

UCLA

UCLA Electronic Theses and Dissertations

Title

Cell Biophysics for Label-free Single-Cell Analysis and Sorting

Permalink

<https://escholarship.org/uc/item/2j26m3fp>

Author

Masaeli, Mahdokht

Publication Date

2013

Peer reviewed|Thesis/dissertation

UNIVERSITY OF CALIFORNIA

Los Angeles

Cell Biophysics for Label-free Single-Cell Analysis
and Sorting

A dissertation submitted in partial satisfaction of the
requirements for the degree Doctor of Philosophy in
Bioengineering

by

Mahdokht Masaeli

2013

ABSTRACT OF THE DISSERTATION

Cell Biophysics for Label-free Single-Cell Analysis and Sorting

by

Mahdokht Masaeli

Doctor of Philosophy in Bioengineering

University of California, Los Angeles, 2013

Professor Dino Di Carlo, Chair

Recent studies have shown that accurate characterization of biological samples is only possible by analyzing single cells rather than the average response from thousands of cells, due to the significant heterogeneity in biological samples. Heterogeneity in gene and protein expression at single cell level has been confirmed using different techniques. Therefore, single cell analysis is critical for accurate representation of cell-to-cell variations within a population, which could be masked by average bulk measurements. Single cell analysis can improve data analysis and give some insight for experimental design when dealing with heterogeneous samples. Single cell analysis can be helpful in providing more insight into specific signaling pathways or cellular properties responsible for cell self-renewal capacity or differentiation. Screening sample for this potential rare population of pluripotent cells is critical before their clinical application. Single cell analysis could also improve diagnostics, one example being to

distinguish normal and cancer cells at different developmental and metastatic stages. Identifying rare cells such as cancer stem cells is difficult since they only represent a small fraction of the total cell population and unique molecular signatures can be drowned out by noise. Single cell analysis is suggested to enable better identification and targeting of these relatively rare populations in tumors. Studying phenotypes in heterogeneous samples and detection of rare populations requires an information-rich data set of cell characteristics to obtain specificity, which can be aided by multiparameter analysis. A longstanding challenge in single-cell analysis is developing specific biomarkers or sets of biomarkers that allow classification of subpopulations of interest, such as cancer stem cells, pluripotent stem cells with high differentiation potential, or immune cells tuned to respond to infections. Sorting is particularly important when nucleic acids are assayed and cells of interest may be rare, and therefore sorting technologies have developed hand-in-hand with analysis approaches. This dissertation reports the development of new tools for label-free multiparameter cell analysis and sorting using its intrinsic biophysical properties.

This dissertation of Mahdokht Masaeli is approved.

Benjamin M. Wu

Amander Therese Clark

Amy Catherine Rowat

Dino Di Carlo, Committee Chair

University of California, Los Angeles

2013

DEDICATION

For Ramin, Mom and Dad

TABLE OF CONTENTS

Abstract of the Dissertation	ii-iii
Committee Page	iv
Dedication	v
Table of Contents	vi
Acknowledgements	vii-viii
Vita	ix-xi
Chapter 1	
Single Cell analysis and Sorting: Need for Multiparameter Label-free Cell Phenotyping	1-25
Chapter 2	
Multiparameter Mechanical and Morphometric Screening of Human Pluripotent Stem cells	26-70
Chapter 3	
The Role of Chromatin Structure in Cell Mechanical Stiffness: Application in Drug Screening	71-96
Chapter 4	
Separation of Particles Based of Aspect Ratio: Application in Cell Sorting by Shape and Deformability	97-155

ACKNOWLEDGEMENTS

Chapter 1

Single Cell analysis and Sorting: Need for Multiparameter Label-free Cell Phenotyping is a version of work in preparation for publication by Mahdokht Masaeli and Dino Di Carlo. Professor Dino Di Carlo is the principal investigator of this work.

Chapter 2

Multiparameter Mechanical and Morphometric Screening of Human Pluripotent Stem cells is a version of work submitted for publication by Mahdokht Masaeli, Henry T. K. Tse, Peter Tseng, Andrew Utada, Amander T. Clark and Dino Di Carlo. We thank Sevgi Unal for her help with fabricating agarose beads and Dewal Gupta for his help with maintaining and staining cells. This work was supported by the David and Lucile Packard Foundation Fellowship in Science and Engineering (D.D.C), an NSF Faculty Early Career Development Award (D.D.C), a Defense Advanced Research Projects Agency Young Faculty Award (D.D.C), and NIH 1R01HD058047 (A.T.C).

Chapter 3

The Role of Chromatin Structure in Cell Mechanical Stiffness: Application in Drug Screening is a version of work submitted for publication by Mahdokht Masaeli, Dewal Gupta, Peter Tseng, Hea-jin Jung, Stephen Young and Dino Di Carlo. This work was supported by the David and Lucile Packard Foundation Fellowship in Science and Engineering (D.D.C), an NSF Faculty Early Career Development Award (D.D.C), a Defense Advanced Research Projects Agency Young Faculty Award (D.D.C), and NIH 1R01HD058047 (A.T.C).

Chapter 4

Separation of Particles Based of Aspect Ratio: Application in Cell Sorting by Shape and Deformability is partly a version of work in preparation for publication by Mahdokht Masaeli, Dewal Gupta and Dino Di Carlo and has been partly reprinted with adaptations with permission from (Masaeli M, Di Carlo D (2012) Continuous Inertial Focusing and Separation of Particles by Shape. *Physical Review X* 2, 031017. Copyright (2012) American Physical Society). Professor Dino Di Carlo is the principal investigator of this work. This work is partially supported by NSF Grant No. 0930501. It is also partly adapted with permission from (Dino Di Carlo (2013) Quantitative Diagnosis of Malignant Pleural Effusions by Single-Cell Mechanophenotyping. *Science Translational Medicine*, 5, 212: 212ra163. Copyright (2013) American Association for the Advancement of Science).

I would like to express my deep gratitude and respect to my advisor, Dr. Dino Di Carlo whose advices and insight was invaluable to me. I would like to thank my friends and colleagues at the Di Carlo lab.

My greatest appreciation goes to my mom, dad and sister and my dear Ramin, for their continuous love and unconditional support; without whom I could not have made it here.

VITA

EDUCATION

University of California Los Angeles, Los Angeles, CA
Bioengineering Department
Doctor of Philosophy Candidate; Advisor: Prof. Dino Di Carlo
Sep 2010-Dec 2013

Northeastern University, Boston, MA
Electrical and Computer Engineering Department (ECE)
Master of Science
Sep 2007-May 2009

Sharif University of Technology
Electrical Engineering Department
Bachelor of Science
Sep 2003-May 2007

PUBLICATIONS, PATENTS AND PROCEEDINGS

Masaeli M, Tse HTK, Gossett DR, Clark AT, Di Carlo D. A label-free high-throughput assay of stem cell pluripotency, *in revision*

Tse HTK, Gossett DR, Moon YS, **Masaeli M**, Sohsman M, Ying Y, Mislick K, Adams RP, Rao J, and Di Carlo D. Improved Diagnosis of Malignant Pleural Effusions by Single-Cell Mechanophenotyping, **Science Translational Medicine**, 2013, 5(212) 212ra163

Weaver WM, Tseng P, Kunze A, **Masaeli M**, Chung A, Dudani J, Kittur, R. P. Kulkarni RP, Di Carlo D. Advances in High- Throughput Single-Cell Microtechnologies. **Current Opinion in Biotechnology**. In press 2013

Amini H, **Masaeli M***, Sollier E*, Xie Y, Ganapathysubramanian B, Stone HA, Di Carlo D. Engineering fluid flow using sequenced microstructures. **Nature Communications**, 2013, 4, 1826 *Equal contribution

Chung AJ, Pulido D, Oka JC, Amini H, **Masaeli M**, Di Carlo D. Microstructure-induced helical vortices allow single-stream and long-term inertial focusing. **Lab Chip**, 2013, 13: 2942-2949.

Masaeli M, Sollier E, Amini H, Mao W, Camacho K, Doshi N, Mitragotri S, Alexeev A, Di Carlo D. Continuous inertial focusing and separation of particles by shape, **Physical Review X**, 2012, 2, 3:031017

Bae H, Ahari AF, Shin H, Nichol JW, Hutson C, **Masaeli M**, Kim S, Aubin H, Khademhosseini A. Cell-laden microengineered pullulan methacrylate hydrogels promote cell proliferation and 3D cluster formation. **Soft Matter**, 2011,7, 1903- 1911. 2

Masaeli M*, Zamanian B*, Khabiry M, Hancock MJ, Nichol JW, Khademhosseini A. Interface Directed Self Assembly of Cell-Laden Microgels **Small**, 2010,6, 8: 937-944 *Equal contribution

Hwang CM, Sant S, **Masaeli M**, Kachouie N, Zamanian B, Khademhosseini A. Single step fabrication of 3D porous cell- laden hydrogel scaffolds **Biofabrication** , 2010, 2, 3: 035003

Hacking SA, **Masaeli M**, Ye Y, Nichol JW, Khademhosseini A. Engineering Hydrogels for Tissue Regeneration **Hydrogels: Properties, Preparation and Applications**, 2009 Edited by David B. Stein, Nova Science Publishers, Inc.

Zamanian B, Kachouie N, **Masaeli M**, Nichol JW, Khademhosseini A. Self-assembly of Cell-laden Hydrogels on the Liquid- Air Interface **3-D Tissue Engineering**, 2009 edited by F. Berthiaume, J. Morgan. Artech House

Nichol JW, Bae H, Kachouie N, Zamanian B, **Masaeli M**, Khademhosseini A, Microscale technologies for tissue engi- neering and stem cell differentiation, **Stem Cell and Tissue Engineering edited** by Song Li, Nicholas LHeureux, Jennifer Elisseeff. World scientific publishing company (WSPC), 2009, Stem Cell and Tissue Engineering

Masaeli M, Sollier E, Di Carlo D. Devices and methods for shape-based particle separation Patent number: WO 2013089883 A2, (assignee: Michael S. Davidson).

Masaeli M, Gossett DR, Di Carlo D. Enrichment of cells by deformed shape, pending. UCLA Case number: 2014-127-1, (assignee: Michael S. Davidson).

Masaeli M, Tse HTK, Gossett DR, Gupta D, Di Carlo D, Multiparameter high-throughput mechanical phenotyping. **Miniaturized Systems for Chemistry and Life Sciences (Micro TAS)**, Freiburg, Germany, 2013.

Masaeli M, Tse HTK, Gossett DR, Di Carlo D, Role of chromatin structure in large strain high-throughput cell deformability measurements, **Biomedical Engineering Society**, Seattle, WA, 2013.

Masaeli M, Tse HTK, Gossett DR, Clark AT, Di Carlo D, Deformability cytometry of embryonic stem cells reveals consistent mechanical properties across cell lines. **Miniaturized Systems for Chemistry and Life Sciences (Micro TAS)**, Okinawa, Japan, 2012.

Amini H, **Masaeli M**, Sollier E, Xie Y, Ganapathysubramanian B, Stone HA, Di Carlo D. Engineering flow cross-section via programmed pillars, **Miniaturized Systems for Chemistry and Life Sciences (Micro TAS)**, Okinawa, Japan, 2012.

Masaeli M, Tse HTK, Gossett DR, Clark AT, Di Carlo, D. Deformability cytometry, a label-free assay of stem cell pluripotency, **Biomedical Engineering Society**, Atlanta, GA, 2012.

Chung AJ, Pulido D, **Masaeli M**, Amini H, Di Carlo D. Low pressure inertial focusing in large-scale microchannels for high- throughput flow cytometry, **Biomedical Engineering Society**, Atlanta, GA, 2012.

Pulido D, Chung A, **Masaeli M**, Amini H, Di Carlo D. Control of interparticle spacing using structured microfluidic channels, **Biomedical Engineering Society**, Atlanta, GA, 2012.

Masaeli M, Sollier E, Amini H, Camacho K, Doshi N, Mitragotri S, Di Carlo D. Effect of Particel Shape on Inertial Focusing, **Biomedical Engineering Society**, Hartford, CT, 2011.

Amini H, **Masaeli M**, Di Carlo D. Pillar Induced Mixing in Microchannels, **Biomedical Engineering Society**, Hartford, CT, 2011.

Amini H, **Masaeli M**, Di Carlo D. Programming fluid flow with microstructures, **Bulletin of the American Physical Society**, Baltimore, MD, 2011.

Hur SC, **Masaeli M**, Di Carlo D, Phenotype Dependent and Independent Inertial Focusing, **Miniaturized Systems for Chemistry and Life Sciences (Micro TAS)**, Seattle, WA 2011.

Masaeli M, Sollier E, Amini H, Camacho K, Doshi N, Mitragotri S, Di Carlo D. Effect of Particel Shape on Inertial Focusing, **Miniaturized Systems for Chemistry and Life Sciences (Micro TAS)**, Seattle, WA 2011.

Amini H, **Masaeli M**, Di Carlo D. Designing Microstructures for Mixing in Microchannels, **Miniaturized Systems for Chemistry and Life Sciences (Micro TAS)**, Seattle, WA 2011.

Masaeli M, Feng G, Dy JC. From Transformation Based Dimensionality Reduction to Feature Selection, **International Conference on Machine Learning**, Haifa, Israel, 2010.

Masaeli M, Yan Y, Cui Y, Feng G, Dy JC. Convex Principal Feature Selection. **SIAM international conference on Data Mining**, Columbus, OH, 2010.

Chapter 1

Single Cell analysis and Sorting: Need for Multiparameter Label-free Cell Phenotyping

Conventional molecular biology analysis techniques for applications in cancer biology, stem cell biology, hematology and tissue engineering have often relied on the average response from thousands of cells in a population. However, accurate characterization of the sample is only possible by analyzing single cells, due to the significant heterogeneity in biological samples ¹⁻⁴. Heterogeneity in gene and protein expression at single cell level has been confirmed using different techniques ^{5,6}. For example, the Mathies group reported that siRNA knockdown of GAPDH gene expression led to ~21% knockdown on average from 50 cells. However, at the single cell level they observed two distinct groups of Jurkat cells with partial knockdown (~50%) and complete knockdown (~0%) ⁷. Another example revealed heterogeneity in known cell lineages in *Caenorhabditis elegans* by single cell gene expression profiles using confocal microscopy by the Kim group ⁸. Interestingly, although they observed diversity in cells, they reported that cells with known fates clustered together in a 2D scatter plot according the correlation in their gene expression. They also observed larger diversity within cells from heterogeneous tissues (e.g. neurons) compared to more homogeneous tissues (e.g. intestinal cells). Therefore, single cell analysis is critical for accurate representation of cell-to-cell variations within a population, which could be masked by average bulk measurements ⁹.

Single cell analysis can improve data analysis and give some insight for experimental design when dealing with heterogeneous samples. Pluripotent cells, for instance, are potentially interesting for applications in regenerative medicine because of their self-renewal and

differentiation potential. These cells, all highly heterogeneous and there is significant cell-cell variations in differentiation potential ^{3,10}. Single cell analysis can be helpful in providing more insight into specific signaling pathways or cellular properties responsible for cell self-renewal capacity or differentiation. Additionally, *in vivo* transplantation of induced pluripotent stem cell-(iPSC-) derived cellular grafts could be risky due to possible existence of a failed-to-differentiate population. Screening sample for this potential rare population of pluripotent cells is critical before their clinical application ^{11,12}. Another example is cancer. Cancer has been widely known as a highly heterogeneous disease. Single tumor cell behavior and response to drugs is critical in designing successful therapeutic strategies ^{13,14}. Single cell analysis could also improve diagnostics, one example being to distinguish normal and cancer cells at different developmental and metastatic stages since cancer cells have been found to have a significantly more heterogeneity in their mitochondrial DNA ¹⁵. One particular phenotype that would be important to identify is the cancer stem cell, which are believed to be responsible for the repopulation of tumors after treatment and is an emerging target for new therapies ^{16,17}. Identifying these cells is difficult since they only represent a small fraction of the total cell population and unique molecular signatures can be drowned out by noise. Single cell analysis is suggested to enable better identification and targeting of these relatively rare populations in tumors.

A longstanding challenge in single-cell analysis is developing specific biomarkers or sets of biomarkers that allow classification of sub-populations of interest, such as cancer stem cells, pluripotent stem cells with high differentiation potential, or immune cells tuned to respond to infections. Biomarkers can be molecular (i.e. nucleic acids, proteins, sugars, or lipids) which

often require labels or amplification approaches to output data, or label-free relying on intrinsic physical properties of cells.

Sorting of cells is a key aspect of single-cell analysis when nucleic acids are assayed and cells of interest may be rare, and therefore sorting technologies have developed hand-in-hand with analysis approaches. Similar to cell analysis techniques, cell sorting has been performed both using tags or labels and in a label-free manner using differences in the intrinsic properties of cells.

Importance and challenges of multiparameter screening

Studying phenotypes in heterogeneous samples and detection of rare populations requires an information-rich data set of cell characteristics to obtain specificity, which can be aided by multiparameter analysis¹⁸. Acquisition of a set of quantitative and qualitative information about single cells, including the level and structure of the expressed proteins, structure of nuclear proteins, cell size, shape, morphology and stiffness enhances accuracy of sample analysis. One of the main focuses of current single cell analysis approaches is increasing the number of simultaneously detected parameters from individual cells at high-throughput. A more comprehensive characterization of cells would provide information on cellular properties responsible for cell self-renewal capacity and detection of rare populations of stem cells in their differentiated progeny, identification of rare populations of circulating tumor cells in blood or cancer stem cells in biopsies, improve prediction of drug effects and toxicity, and so on. Having a large survey of cellular parameters could also be helpful in identifying the most predictive parameters in a specific application. In the past few years, efforts have increased the number of detectable fluorophores by flow cytometry and which has significantly improved the capability

of these systems to immunophenotype and discriminate between normal and malignant cells, or immune cell subpopulations^{19–23}.

While increasing the amount of information a technique can provide on single cells could have substantial advantages in improving specificity and identifying new subpopulations, one of the challenges is the interpretation and visualization of high-dimensional data. Generally, analyzing multidimensional data involves: i) *normalization and standardization* to allow for meaningful data comparison between data captured on different days or using different instruments by different operators, ii) *statistical tests* to determine and validate the significance of the data in accepting or rejecting a hypothesis, iii) *clustering* to detect possible unknown populations in the dataset, iv) *visualization* to view as much information provided by the multiparameter data as possible and v) *machine learning* to build proper classifiers and quantify the fraction of data set belonging to each predefined class²⁴. New technologies are emerging for acquiring and analyzing single-cell multi-dimensional characteristics for applications from cancer diagnostics to drug discovery.

Label-based single cell multiparameter screening and sorting

Flow cytometry: Flow cytometry is probably one of the most widely employed techniques that is used for single-cell analysis for research and diagnostics^{25,26}. The technique quantifies molecular properties from individual cells in a stream of fluid by illumination of targeted fluorophores with lasers. In the clinic, flow cytometry has been routinely used in common laboratory tests, including complete blood counts as well as CD4⁺ T cell counts in HIV patients^{27,28}. It has also shown promise in identifying normal and malignant hematopoietic and lymphoid cells as well as detecting subtypes of inflammatory cells active in diseases such as

psoriasis and lupus using multicolor analysis^{29,30}. The massive production of monoclonal antibodies, high-quality reagents, a wide variety of fluorochromes and particularly advances in multiparameter flow cytometry has improved the accuracy of this technique as a clinical diagnostic tool^{19,31}. New microfluidic platforms have also been recently introduced to integrate cell culture, sample preparation and fluorescence imaging and microfluidic flow cytometry, mainly to permit analysis of small-size samples (100-1000 cells) such as fine-needle aspirations³². These approaches have been used to monitor immune response in macrophages and monocytes.

Flow cytometry has also shown success in separating cells and purifying specific cell populations. After cell interrogation by laser light, the single cell stream is broken into droplets using a vibrating fine nozzle. The droplets carrying cells of interest based on the signals captured from the cells are then electrostatically charged. Using an electromagnetic field, the droplets are pushed into different outlets based on their charge²⁵. Following the identification of CD34 as a marker of human hematopoietic and progenitor cells, flow cytometry was used to deplete contaminating tumor cells in hematopoietic stem cell grafts for autologous transplantation³³.

One of the main disadvantages of flow cytometry is that it requires prior *in vivo* or *in vitro* labeling, which could be expensive and laborious¹. Multicolor flow cytometry also needs careful correction for signal spillover from individual fluorochromes into other detectors^{34,35}. In the currently used clinical flow cytometry, depending on the number of detectors, up to more than 10 different fluorescence emissions can be measured for individual cells simultaneously. Due to the spectral spillover mentioned above, interpretation of data by an experienced operator is critical³⁶. Additionally, the number of molecular measurements are limited to 10-20 even using correction algorithms which involve testing many different controls for immunophenotyping

standardization, which add to the cost and time to implement such approaches^{35,37}. For *in vivo* labeling, characteristics of endogenous proteins can be altered following tagging with fluorescent proteins or their derivatives. Another issue is photobleaching of fluorophores and autofluorescence of cells, which might affect the outcome of the analysis to a great extent³⁸. One other important limitation to flow cytometry, is the lack of proper standardization and instrument setup protocols^{39,40}. Specific professional training has recently been suggested to be critical in subjectivity-related variability observed in the data gathered in a number of clinical studies³⁷. In spite of these disadvantages, multicolor flow cytometry has enabled a wide range of new clinical diagnostics because of the specificity achieved with combinations of biomarkers³⁷.

Mass cytometry: Mass cytometry allows increased numbers of analyzed proteins beyond what even multicolor flow cytometry techniques are capable of. While operating at comparable throughputs with flow cytometry, in mass cytometry cells can be stained with up to 100 antibodies with minimal signal overlap⁴¹. Antibodies are conjugated to different metal isotope containing polymers and the metal tags are quantified in discrete time-separated detectors using inductively coupled plasma time-of flight mass spectroscopy. Mass cytometry has been introduced as a single cell multi-target immunoassay⁴². One main disadvantage of this technique is the cost and time associated with developing the immunoassay and labeling such a large number of different antibodies with metal tags before antigen binding.

Laser scanning cytometry (LSC): While sharing features with flow cytometry, LSC is unique in that it is a microscope-based approach and can measure cells adhered to a slide and can be a more suitable cytometer for applications with adherent cells⁴³. LSC is a technique that can detect several cellular constituents and features simultaneously from laser excited fluorescence

measurements at multiple wavelengths. Notably, unlike flow cytometry LSC is capable of providing time-dependent information from individual cells since the cells can be constantly analyzed over time⁴⁴. These include changes in both morphological and biochemical features within a cell. LSC offers a more limited throughput compared to flow cytometry-based techniques⁹. In addition to the total intensity of the fluorescent signal, LSC can capture other parameters such as the maximal intensity of a pixel, integration area, the perimeter of the integration contour and circularity, all of which increase specificity of cell identification.

Automated microscopy: Automated microscopy, also known as high-throughput microscopy, image cytometry or high-content screening has shown promise in quantitative analysis of cell behavior and characteristics⁴⁵. Compared to LSC it is usually a lower throughput technique but with higher imaging resolution. Microscopy-based cell analysis has been the primary means for studying cell function and behavior for a long time⁴⁶. Microscopy is able to monitor single cells and reveal biological mechanisms through appropriate staining and is high in information content, capable of collecting high-resolution images of cells from time-lapse experiments. Although microscopy usually reports on the average behavior of cells, appropriate image processing and data analysis techniques can be utilized to determine behavior of single cells under study individually. Therefore, one of the major bottlenecks of automated microscopy for single cell analysis is reliable interpretation of the captured images⁴⁷. Compared to flow cytometry, automated microscopy is advantageous in its compatibility with adherent cells and time-lapse experiment. It can also provide information on protein structure and localization if image and data analysis techniques are reliable enough to allow for high-fast and accurate processing.

Label-free single cell screening and sorting

While most of the conventional single cell analysis and sorting tools rely on molecular properties of cellular proteins and DNA, label-free analysis and manipulation approaches are mainly based on intrinsic biophysical properties of cells. These approaches are attractive in their low cost and reduced sample preparation time. Additionally, they can report on properties of cell subpopulations that could reveal unknown molecular properties or pathways that cannot be targeted by known antigens or labeling assays. For instance, the most common tumor detection methods still rely on direct or assisted visualization of primary tumor mass and immunohistopathology that reveals antigens that are believed to be indicative of tumor progression. Although being useful in tumor staging from biopsies with some pre-knowledge, specific cocktails are often needed depending on the tumor of origin. While single or multiple molecular changes can be indicative of cell type, as discussed previously there is significant cellular heterogeneity which can confound classification, requiring even more parameters. As an alternative approach biophysical markers of cellular architecture instead assays emergent properties that arise from a range of molecular changes, which could be more integrative without first breaking down the analysis to component pieces. Here, we list different intrinsic characteristics of cells that have been used for single cell analysis and sorting and briefly explain the common techniques.

Size. One of the most common label-free cell characterization and separation parameters is cell size. Cell size measurements could be indicative of cell type and state⁴⁸. Differences in cell sizes of different tissues have been used for sample analysis purification in different applications. For example, circulating tumor cells (CTCs) have been separated from blood cells due to their larger size using a variety of approaches^{49,50}. However, the measurements and sorting approaches

based on size are also affected by other properties of cells that might not be accounted for in a controlled manner unless these technologies are able to quantify those other characteristics and decouple their effect on cell size.

Size difference has been routinely used for blood fractionation. Microfabricated filters have been used for fractionating blood into its components using a range of well-controlled pore sizes⁵¹. Impedance-based volume sensors and micro-Coulter counters quantify single cell volume by probing the variation in ionic current through a narrow pore through which the cells of interest are forced to pass^{52–54}. These techniques have been used to measure the volume of single red blood cells, yeast and *Escherichia coli*^{53,55}. Pinched flow fractionation is another technique for fractionation of samples by size using hydrodynamic forces⁵⁶. Deterministic lateral displacement (DLD) sort cells of different sizes and particles in laminar flow and has also been used for blood fractionation using micropost arrays. Displacement of cells perpendicular to the primary flow has been observed to depend on the pattern of array and cell size^{57,58}. Another technique that allows for accurate cell sorting at high-throughput is based on inertial effects in microfluidic platforms. It has been shown that particles that are randomly distributed in suspension migrate to specific equilibrium positions depending on the effective diameter as they pass through a channel⁵⁹. This equilibrium position could be affected by cell/particle shape and size defining its rotational or effective diameter, since the particles usually rotate as they migrate downstream^{60–62}.

Cell size is suggested to be regulated by a number of factors, including cell contact, environmental signaling cues, and genetic and epigenetic properties^{63,64}. Although cell size differences can be indicative of cell type and state, significant heterogeneity has been observed among individual cell of the same population. This variation can arise from the dependence of

cell size on cell cycle stage⁶⁵. Additionally, endosome subcellular localization is correlated with cell size and shape⁶⁶. In one study, when single cells were forced to adopt identical size, the heterogeneity observed in intracellular organelle distribution was extremely reduced⁶⁶. When single cells start to divide, even under highly controlled experimental setups, they start to experience differences in cell-cell contacts and available space, which results in cell-cell variation in subcellular component localization and size. Studies have also shown a remarkable variation in the growth rate of cells in the same population⁶⁷. In addition to intrinsic heterogeneity in cell size within a population, some of the methods for cell size based sorting and analysis described above are affected by other cellular properties, including cell shape and stiffness. Information on other cell characteristics is essential in decoupling the effect of these factors on cell size and accounting for within-population variations for better classification of cells based on their state.

Mass and Density. Many important cellular processes including cell cycle progression, differentiation, apoptosis and disease state are linked to specific changes in mass-to-volume ratio of cells^{64,68,69}. Quantifying cell mass and density could be beneficial in basic biology as well as disease diagnostic applications.

While centrifugation has been used for a long time as a macroscale technique for separating cells and particles based on their density, it is difficult to obtain information concerning individual cells using this approach. Magnetic levitation is one method for measuring the density of micron-scale particles, however, this method is not compatible with live cells since it requires concentrated metal salt solutions⁷⁰. Recently, a microfluidic mass sensor has been introduced that is capable of measuring the mass, volume and density of single cells. This method is capable of measuring the density of approximately 500 individual cells per hour⁶⁸. Separation of particles

based on their size and density has been also achieved by hydrodynamic amplification of gravitational force⁷¹.

Similar to cell size, heterogeneity in cell mass and density can arise from cell cycle stage. Cell growth rate is shown to increase with cell mass, potentially contributing to even further heterogeneity in cell mass within a population^{63,67}. Techniques that are used to characterize cell mass can also be sensitive to other parameters. One study showed that the measured mass of paraformaldehyde-fixed cells was 1.4 times greater than that of the corresponding living cell⁷². Studies suggest that cell stiffness is one parameter that can significantly affect the cellular mass measurement by resonating sensors^{72,73}.

Shape and morphology. Cellular and nuclear shape and morphology have long been one of the main tools for histological detection and classification of cancer²⁶. Change in the shape of apoptotic cells has also been reported consistently⁷⁴. It is suggested that this change in cell morphology is mainly due to the formation of plasma membrane pores by rigid areas of tightly packed phospholipids in the plasma membrane. Cell membrane morphological properties are important features indicating tumor development and are used to determine the effect of antitumor drugs and find their minimum effective dosage avoiding potential side effects⁷⁴. The overall cellular outline and morphological features of adhered cells are mainly controlled by assembly and disassembly of focal adhesions and associated actomyosin contractility^{75,76}. Changes in gene expression and reorientation and reorganization of cytoskeletal components are suggested to modify cell morphological properties. The ability of cells to change their morphology, also referred to as morphological plasticity is believed to be different in differentiated versus pluripotent embryonic stem cells⁷⁷. While most of the adult cells are differentiated and are limited in their ability to change their shape, cells are believed to regain

their ability to find new shapes that are most efficient for their migration and invasion upon pathogenesis of disease^{78–80}. These changes in morphology would also result in a larger heterogeneity and, although not completely understood yet, could be a target of stemness or metastatic cancer in the future^{80,81}. However, due to significant shape variations within a sample, cell type and state-based classification solely using morphological features seems to be infeasible. For example, one study found larger natural shape variation in a population of Keratocytes compared to the changes in shape induced by a number of cytoskeletal component reorganizing drugs⁷⁸. Capturing information on cell shape and morphology has been mainly limited to microscopy-based approaches. Using images captured by microscopy, different studies have been able to capture hundreds of quantitative morphological features from different cells and link these morphological parameters to gene expression⁷⁷. In addition to cell-to-cell heterogeneity the low throughput and the need for computationally expensive image analysis techniques, limits the application of morphological-based analysis tools.

A number of approaches have been recently introduced to sort particles and cells based on their shape. HDF, a hydrodynamic method of fractionating a sample by size, was recently applied to separate budding and single cells in a yeast cell mixture⁸². This approach involves highly complex fabrication steps and are limited in throughput. Acoustic radiation forces can also be utilized to separate particles based on their shape by exposing them to ultrasound waves of controlled wavelength and pressure. In addition to shape, particle size (volume), relative density and compressibility of particle and fluid affect the forces acting on the particles. Recently, inertial forces have been used to successfully separate particles and cells of different shapes or aspect ratios. This was achievable due to dramatic differences in inertial equilibrium positions

which result from differences in rotational diameter. This technique has also shown promise in sorting budding yeast cells based on their cell cycle stage.

Deformability. Cell mechanical stiffness is an important property in cell function. It is shown to be indicative of pluripotency and disease state⁸³. Increased deformability is observed in mouse and human pluripotent stem cells and their nuclei compared to that of their differentiated progeny⁸⁴. An increase in both size and deformability has also been consistently reported to be correlated with malignancy. Studies have shown up to 3.5 fold increase in the deformability of metastatic cancer cells disseminated in pleural fluids compared to that of benign cells⁸⁵. This increase in deformability is suggested to be linked to the ability of malignant cells to migrate through tissues and metastasize.

Atomic force microscopy (AFM) is one of the traditional methods for characterization of single cell stiffness. AFM operates by tracking the deflection of a micron-sized cantilever probe as its tip interacts with, and indents the sample. Although AFM is relatively simple and its resolution is at the nanometer scale, there are several difficulties associated with cell mechanical characterization using AFM. In addition to be severely limited in throughput (<10 cells per hour), measurements with AFM requires highly skilled operators. There is a significant variability in measurement depending on the user, the shape of the cantilever, and the position at which the tip is interacting with cells, as it exerts forces over sub- μm^2 surface areas of cells. AFM is also more difficult for measuring cells that are in suspension and are not adhered to a surface, as is the case in many diagnostic fluids. Micropipette aspiration is another technique for characterization of cell stiffness by applying a known suction pressure to cells and bringing them into a small diameter pipette. The length of aspiration is used to measure the cortical tension and Young's modulus of the aspirated cell⁸⁶. Micropipette aspiration- and AFM-based techniques have been

used to measure the stiffness of different cells and in studies on probing the mechanical properties of mitotic cells. By coupling it with fluorescent protein labeling, micropipette aspiration enables examining the cell response to mechanical stress by changing protein localization⁸⁷. Micropipette aspiration is advantageous over AFM in that it applies force to the whole cell and can allow for less cell-to-cell variation in measurement due to the operator. However, it is still a low throughput approach and is not applicable to routine screening. Optical stretching uses a double-beam trap in which two opposed, slightly divergent laser beams trap the cell or particle in the middle. The force that is applied to the cell is due to the difference in refractive index of the cell and the media⁸⁸.

Sorting cells based on deformability is challenging. Current size-based techniques have difficulty sorting deformable objects. The DLD technique which was previously used to separate red blood cells, white blood cells and platelets based on their size, has been recently applied to the separation of non-spherical particles by orienting them via controlling device depth. This technique has also been used to sort cells based on their deformability⁸⁹. However, cell size is still a major factor in sorting by DLD, where more deformable objects are separated together with smaller and stiffer objects.

Acoustic radiation forces can also be utilized to separate particles based on their shape by exposing them to ultrasound waves of controlled wavelength and pressure. In addition to particle size (volume), relative density and compressibility of particle and fluid affect the forces acting on the particles⁹⁰.

A few previous studies have demonstrated the promise of using effects of fluid inertia in high-speed confined microfluidic flows for sorting cells and particles based on their physical

properties. Most of the sorting demonstrations have solely relied on differences in cell size ⁹¹. Previous studies demonstrated deformability-based differences in equilibrium positions of flowing cells and viscous droplets in the microchannel cross-section and used these differences to sort and enrich cancer cells from blood samples ⁹². However, the extent to which the cells are deformed in this method is small and larger deformations are expected to improve enrichment and sample purity. Additionally, this technique is also sensitive to cell size, such that larger less deformable cells would behave the same as smaller and softer cells.

Biochemical spectra. Label-free quantitative analysis of single cell entire proteome can be achieved using single cell mass spectrometry (MS) ⁹³. However, currently the sensitivity of these single cell approaches to detect small amount of proteins found in a single cell is low. Fractionation of proteins prior to mass spectrometry is suggested to be helpful, which increases the sample preparation time⁴¹. This technique still has limitations and cannot be used of routine analysis of cell at the current stage. Further developments are needed especially in sample preparation process to allow high-throughput analysis. Recently, advancement in throughput for detection of hemoglobin in individual erythrocytes was achieved by integrating microfluidic cell lysis and electrophoretic separation with MS ⁹⁴. Integrating microarray with MS has also shown promise in high-throughput single cell protein analysis ⁹⁵. Raman tweezers is another technology that classifies single cells based on their biochemical spectra. Differences in biochemical spectra of cells has been observed between prostate cancer cell lines and bladder cell lines using Raman tweezers ⁹⁶.

Dielectric properties. The changes in electrical properties of cells, such as conductivity and permittivity, are also connected to state ⁹⁷. There are several techniques that characterize single cells based on their electric properties. Microelectrode array setups use several microelectrodes

that are coated with a self-assembled monolayer and a peptide and a couple of larger counter electrodes. Another technique captures individual cells using a flow bottleneck where the electrodes are located. The impedance is measured while the cells are trapped in the bottleneck⁹⁸. Micropillars and traps with electrodes have also been used to characterize the electrical properties of trapped cells⁹⁹. Scanning dielectric microscopy is another approach that uses an electrode probe to scan over individual cells¹⁰⁰.

Previous studies have shown the feasibility of using this technique in separating bacteria from peripheral blood, one cell population from another and cancer cells from normal cells^{101,102}. Electrical properties of cells could indicate the structure and composition of cells and be used to sort cells based on these properties. These methods are mainly based on dielectrophoretic forces that are applied to cells using a non-uniform electric field. The level of force applied to the cells depend on their polarization, which is a function of their dielectric properties, such as the frequency dependent conductivity and permeability of cell and its membrane as well as the conductivity of its surrounding media¹⁰³. Impedance spectroscopy has been used to measure membrane capacitance and resistance and cytoplasmic conductivity and permittivity of cells in suspension^{53,104}. Isodielectric separation (IDS) is a technique that separates cells and particles based on their electrical properties at different frequencies and medium conductivities. Microfluidic devices with integrated electrodes have been introduced recently and have shown promise in discriminating erythrocytes from leukocytes, and leukocyte subpopulations^{105,106}. One of the main challenges of dielectrophoretic separation is the strong dependence of dielectrophoretic forces on cell size and conductivity of media, which makes the measurement and sorting difficult in highly conductive physiological buffers.

Need for high-throughput multiparameter cell biophysical assays

Single cell analysis is critical in analyzing heterogeneous samples and identifying rare cell populations. Due to the consistently reported heterogeneity in cellular samples, one of the main factors for accurate analysis of these samples is to capture a large amount of information on thousands of individual cells. This requires the emergence of high-throughput, high-information content technologies. Flow cytometry has been one of the main techniques for single cell analysis for decades. Addition of new parameters beyond flow cytometry capability, using recently introduced techniques (e.g. mass cytometry) has enabled further discretization and quantification of new cell states. This is a critical frontier as what we now think of as a uniform subpopulation of “neutrophils” or “tumor cells”, is most definitely a unique mixture of thousands of different states that can be more accurately quantified.

Recently there has been interest in analyzing and sorting cells using label-free approaches as alternative to label-based techniques. With these approaches, there are particular advantages for diagnostics as the cost and time of preparing samples can be reduced significantly. Sorting based on biophysical cell characteristics is believed to improve the ability of identifying and sorting homogeneous subpopulations as opposed to relying on specific markers and tags. Advances in understanding the link between cell type and state and its intrinsic biophysical properties have led to the development of technologies for characterization and separation of cells. Extension to multiparameter analysis, similar to that of new label-based techniques, will be required for label-free techniques to obtain useful cell analysis and classification. *Multiparameter label-free approaches* are emerging as the next generation of low-cost cytometry techniques, with sufficient information content to rival label-based approaches.

Bibliography

1. Wang, D. & Bodovitz, S. Single cell analysis: the new frontier in “omics.” *Trends Biotechnol.* **28**, 281–290 (2010).
2. Irish, J. M., Kotecha, N. & Nolan, G. P. Mapping normal and cancer cell signalling networks: towards single-cell proteomics. *Nat. Rev. Cancer* **6**, 146–155 (2006).
3. Graf, T. & Stadtfeld, M. Heterogeneity of embryonic and adult stem cells. *Cell Stem Cell* **3**, 480–483 (2008).
4. Marusyk, A., Almendro, V. & Polyak, K. Intra-tumour heterogeneity: a looking glass for cancer? *Nat. Rev. Cancer* **12**, 323–334 (2012).
5. Elowitz, M. B., Levine, A. J., Siggia, E. D. & Swain, P. S. Stochastic gene expression in a single cell. *Science* (80-.). **297**, 1183–1186 (2002).
6. Cai, L., Friedman, N. & Xie, X. S. Stochastic protein expression in individual cells at the single molecule level. *Nature* **440**, 358–362 (2006).
7. Toriello, N. M. *et al.* Integrated microfluidic bioprocessor for single-cell gene expression analysis. *Proc. Natl. Acad. Sci.* **105**, 20173–20178 (2008).
8. Liu, X. *et al.* Analysis of Cell Fate from Single-Cell Gene Expression Profiles in *C. elegans*. *Cell* **139**, 623–633 (2009).
9. Carlo, D. Di & Lee, L. P. Dynamic single-cell analysis for quantitative biology. *Anal. Chem.* **78**, 7918–7925 (2006).
10. Chan, E. M. *et al.* Live cell imaging distinguishes bona fide human iPS cells from partially reprogrammed cells. *Nat. Biotechnol.* **27**, 1033–1037 (2009).
11. Wakitani, S. *et al.* Embryonic stem cells injected into the mouse knee joint form teratomas and subsequently destroy the joint. *Rheumatology* **42**, 162–165 (2003).
12. Swijnenburg, R.-J. *et al.* Embryonic stem cell immunogenicity increases upon differentiation after transplantation into ischemic myocardium. *Circulation* **112**, I–166 (2005).
13. Dexter, D. L. & Leith, J. T. Tumor heterogeneity and drug resistance. *J. Clin. Oncol.* **4**, 244–257 (1986).
14. Heppner, G. H., Dexter, D. L., DeNucci, T., Miller, F. R. & Calabresi, P. Heterogeneity in drug sensitivity among tumor cell subpopulations of a single mammary tumor. *Cancer Res.* **38**, 3758–3763 (1978).

15. He, Y. *et al.* Heteroplasmic mitochondrial DNA mutations in normal and tumour cells. *Nature* **464**, 610–614 (2010).
16. Clarke, M. F. *et al.* Cancer stem cells—perspectives on current status and future directions: AACR Workshop on cancer stem cells. *Cancer Res.* **66**, 9339–9344 (2006).
17. Ho, M. M., Ng, A. V., Lam, S. & Hung, J. Y. Side population in human lung cancer cell lines and tumors is enriched with stem-like cancer cells. *Cancer Res.* **67**, 4827–4833 (2007).
18. Zanella, F., Lorens, J. B. & Link, W. High content screening: seeing is believing. *Trends Biotechnol.* **28**, 237–245 (2010).
19. Pedreira, C. E., Costa, E. S., Lecrevisse, Q., van Dongen, J. J. M. & Orfao, A. Overview of clinical flow cytometry data analysis: recent advances and future challenges. *Trends Biotechnol.* (2013).
20. Freer, G. & Rindi, L. Intracellular cytokine detection by fluorescence-activated flow cytometry: basic principles and recent advances. *Methods* (2013).
21. Al-Mawali, A., Gillis, D. & Lewis, I. The role of multiparameter flow cytometry for detection of minimal residual disease in acute myeloid leukemia. *Am. J. Clin. Pathol.* **131**, 16–26 (2009).
22. Ferreira-Facio, C. S. *et al.* Contribution of multiparameter flow cytometry immunophenotyping to the diagnostic screening and classification of pediatric cancer. *PLoS One* **8**, e55534 (2013).
23. Paiva, B. *et al.* Utility of flow cytometry immunophenotyping in multiple myeloma and other clonal plasma cell-related disorders. *Cytom. Part B Clin. Cytom.* **78**, 239–252 (2010).
24. Feng, Y., Mitchison, T. J., Bender, A., Young, D. W. & Tallarico, J. A. Multi-parameter phenotypic profiling: using cellular effects to characterize small-molecule compounds. *Nat. Rev. Drug Discov.* **8**, 567–578 (2009).
25. Jahan-Tigh, R. R., Ryan, C., Obermoser, G. & Schwarzenberger, K. Flow cytometry. *J. Invest. Dermatol.* **132**, e1 (2012).
26. Jaye, D. L., Bray, R. A., Gebel, H. M., Harris, W. A. C. & Waller, E. K. Translational applications of flow cytometry in clinical practice. *J. Immunol.* **188**, 4715–4719 (2012).
27. Waldrop, S. L., Pitcher, C. J., Peterson, D. M., Maino, V. C. & Picker, L. J. Determination of antigen-specific memory/effector CD4⁺ T cell frequencies by flow cytometry: evidence for a novel, antigen-specific homeostatic mechanism in HIV-associated immunodeficiency. *J. Clin. Invest.* **99**, 1739 (1997).

28. Barnett, D. *et al.* VERITAS?: A Time for VERIQAS™ and a new approach to training, education, and the quality assessment of CD4+ T lymphocyte counting (I). *Cytom. Part B Clin. Cytom.* **82**, 93–100 (2012).
29. Ferenczi, K., Burack, L., Pope, M., Krueger, J. G. & Austin, L. M. CD69, HLA-DR and the IL-2R identify persistently activated T cells in psoriasis vulgaris lesional skin: blood and skin comparisons by flow cytometry. *J. Autoimmun.* **14**, 63–78 (2000).
30. Moreton, P. *et al.* Eradication of minimal residual disease in B-cell chronic lymphocytic leukemia after alemtuzumab therapy is associated with prolonged survival. *J. Clin. Oncol.* **23**, 2971–2979 (2005).
31. Owens, M. A. & Loken, M. R. *Flow cytometry principles for clinical laboratory practice: quality assurance for quantitative immunophenotyping*. (Wiley-Liss New York, 1995).
32. Srivastava, N. *et al.* Fully integrated microfluidic platform enabling automated phosphoproteomic profiling of macrophage response. *Anal. Chem.* **81**, 3261–3269 (2009).
33. Brugger, W. *et al.* Positively selected autologous blood CD34+ cells and unseparated peripheral blood progenitor cells mediate identical hematopoietic engraftment after high-dose VP16, ifosfamide, carboplatin, and epirubicin. *Blood* **84**, 1421–1426 (1994).
34. Robinson, J. P., Rajwa, B., Patsek, V. & Davisson, V. J. Computational analysis of high-throughput flow cytometry data. *Expert Opin. Drug Discov.* **7**, 679–693 (2012).
35. Roederer, M. Spectral compensation for flow cytometry: visualization artifacts, limitations, and caveats. *Cytometry* **45**, 194–205 (2001).
36. Duquesnoy, R. & Marrari, M. Multilaboratory evaluation of serum analysis for HLA antibody and crossmatch reactivity by lymphocytotoxicity methods: Results of the American Society for Histocompatibility and Immunogenetics/College of American Pathologists Proficiency Testing Surveys D. *Arch. Pathol. Lab. Med.* **127**, 149–156 (2003).
37. Pachón, G., Caragol, I. & Petriz, J. Subjectivity and flow cytometric variability. *Nat. Rev. Immunol.* **12**, 396 (2012).
38. Van den Engh, G. & Farmer, C. Photo-bleaching and photon saturation in flow cytometry. *Cytometry* **13**, 669–677 (1992).
39. Maecker, H. T. & McCoy Jr, J. P. A model for harmonizing flow cytometry in clinical trials. *Nat. Immunol.* **11**, 975 (2010).
40. Maecker, H. T., McCoy, J. P. & Nussenblatt, R. Standardizing immunophenotyping for the human immunology project. *Nat. Rev. Immunol.* **12**, 191–200 (2012).

41. Wu, M. & Singh, A. K. Single-cell protein analysis. *Curr. Opin. Biotechnol.* **23**, 83–88 (2012).
42. Lou, X. *et al.* Polymer-Based Elemental Tags for Sensitive Bioassays. *Angew. Chemie Int. Ed.* **46**, 6111–6114 (2007).
43. Pozarowski, P., Holden, E. & Darzynkiewicz, Z. in *Cell Imaging Tech.* 165–192 (Springer, 2006).
44. Tárnok, A. & Gerstner, A. O. H. Clinical applications of laser scanning cytometry. *Cytometry* **50**, 133–143 (2002).
45. Lindström, S. & Andersson-Svahn, H. Miniaturization of biological assays—Overview on microwell devices for single-cell analyses. *Biochim. Biophys. Acta (BBA)-General Subj.* **1810**, 308–316 (2011).
46. Carpenter, A. E. *et al.* CellProfiler: image analysis software for identifying and quantifying cell phenotypes. *Genome Biol.* **7**, R100 (2006).
47. Gönczy, P. *et al.* Functional genomic analysis of cell division in *C. elegans* using RNAi of genes on chromosome III. *Nature* **408**, 331–336 (2000).
48. Beech, J. P., Holm, S. H., Adolfsson, K. & Tegenfeldt, J. O. Sorting cells by size, shape and deformability. *Lab Chip* **12**, 1048–1051 (2012).
49. Dharmasiri, U., Witek, M. A., Adams, A. A. & Soper, S. A. Microsystems for the capture of low-abundance cells. *Annu. Rev. Anal. Chem. Palo Alto Calif* **3**, 409–431 (2010).
50. Ozkumur, E. *et al.* Inertial focusing for tumor antigen-dependent and -independent sorting of rare circulating tumor cells. *Sci. Transl. Med.* **5**, 179ra47 (2013).
51. Ji, H. M. *et al.* Silicon-based microfilters for whole blood cell separation. *Biomed. Microdevices* **10**, 251–257 (2008).
52. Riordon, J., Mirzaei, M. & Godin, M. Microfluidic cell volume sensor with tunable sensitivity. *Lab Chip* **12**, 3016–3019 (2012).
53. Cheung, K., Gawad, S. & Renaud, P. Impedance spectroscopy flow cytometry: On-chip label-free cell differentiation. *Cytom. Part A* **65**, 124–132 (2005).
54. Sridhar, M. *et al.* Experimental characterization of a metal-oxide-semiconductor field-effect transistor-based Coulter counter. *J. Appl. Phys.* **103**, 104701 (2008).
55. Bernabini, C., Holmes, D. & Morgan, H. Micro-impedance cytometry for detection and analysis of micron-sized particles and bacteria. *Lab Chip* **11**, 407–412 (2011).

56. Yamada, M., Nakashima, M. & Seki, M. Pinched flow fractionation: continuous size separation of particles utilizing a laminar flow profile in a pinched microchannel. *Anal. Chem.* **76**, 5465–5471 (2004).
57. Huang, L. R., Cox, E. C., Austin, R. H. & Sturm, J. C. Continuous particle separation through deterministic lateral displacement. *Science* (80-.). **304**, 987–990 (2004).
58. Zheng, S., Tai, Y.-C. & Kasdan, H. A micro device for separation of erythrocytes and leukocytes in human blood. in *Eng. Med. Biol. Soc. 2005. IEEE-EMBS 2005. 27th Annu. Int. Conf.* 1024–1027 (IEEE, 2006).
59. Di Carlo, D. Inertial microfluidics. *Lab Chip* **9**, 3038–3046 (2009).
60. Hur, S. C., Choi, S.-E., Kwon, S. & Carlo, D. Di. Inertial focusing of non-spherical microparticles. *Appl. Phys. Lett.* **99**, 44101 (2011).
61. Mao, W. & Alexeev, A. Hydrodynamic sorting of microparticles by size in ridged microchannels. *Phys. Fluids* **23**, 51704 (2011).
62. Masaeli, M. *et al.* Continuous Inertial Focusing and Separation of Particles by Shape. *Phys. Rev. X* **2**, 31017 (2012).
63. Bryan, A. K., Goranov, A., Amon, A. & Manalis, S. R. Measurement of mass, density, and volume during the cell cycle of yeast. *Proc. Natl. Acad. Sci.* **107**, 999–1004 (2010).
64. Wolff, D. A. & Pertoft, Hå. SEPARATION OF HELA CELLS BY COLLOIDAL SILICA DENSITY GRADIENT CENTRIFUGATION I. Separation and Partial Synchrony of Mitotic Cells. *J. Cell Biol.* **55**, 579–585 (1972).
65. Snijder, B. & Pelkmans, L. Origins of regulated cell-to-cell variability. *Nat. Rev. Mol. Cell Biol.* **12**, 119–125 (2011).
66. Schauer, K. *et al.* Probabilistic density maps to study global endomembrane organization. *Nat. Methods* **7**, 560–566 (2010).
67. Mir, M. *et al.* Optical measurement of cycle-dependent cell growth. *Proc. Natl. Acad. Sci.* **108**, 13124–13129 (2011).
68. Grover, W. H. *et al.* Measuring single-cell density. *Proc. Natl. Acad. Sci.* **108**, 10992–10996 (2011).
69. Maric, D., Maric, I. & Barker, J. L. Buoyant density gradient fractionation and flow cytometric analysis of embryonic rat cortical neurons and progenitor cells. *Methods* **16**, 247–259 (1998).

70. Mirica, K. A., Shevkoplyas, S. S., Phillips, S. T., Gupta, M. & Whitesides, G. M. Measuring densities of solids and liquids using magnetic levitation: fundamentals. *J. Am. Chem. Soc.* **131**, 10049–10058 (2009).
71. Huh, D. *et al.* Gravity-driven microfluidic particle sorting device with hydrodynamic separation amplification. *Anal. Chem.* **79**, 1369–1376 (2007).
72. Park, K. *et al.* Measurement of adherent cell mass and growth. *Proc. Natl. Acad. Sci.* **107**, 20691–20696 (2010).
73. Voinova, M. V, Jonson, M. & Kasemo, B. “Missing mass” effect in biosensor’s QCM applications. *Biosens. Bioelectron.* **17**, 835–841 (2002).
74. Van den Driesche, S. *et al.* Cell membrane morphology analysis using an infrared sensor system. *Sensors Actuators B Chem.* (2012).
75. Paluch, E. & Heisenberg, C.-P. Biology and physics of cell shape changes in development. *Curr. Biol.* **19**, R790–R799 (2009).
76. Pelham, R. J. & Wang, Y. Cell locomotion and focal adhesions are regulated by substrate flexibility. *Proc. Natl. Acad. Sci.* **94**, 13661–13665 (1997).
77. Yin, Z. *et al.* A screen for morphological complexity identifies regulators of switch-like transitions between discrete cell shapes. *Nat. Cell Biol.* **15**, 860–71 (2013).
78. Keren, K. *et al.* Mechanism of shape determination in motile cells. *Nature* **453**, 475–480 (2008).
79. Mogilner, A. & Keren, K. The shape of motile cells. *Curr. Biol.* **19**, R762–R771 (2009).
80. Sanz-Moreno, V. *et al.* Rac activation and inactivation control plasticity of tumor cell movement. *Cell* **135**, 510–523 (2008).
81. Wolf, K. *et al.* Compensation mechanism in tumor cell migration mesenchymal–amoeboid transition after blocking of pericellular proteolysis. *J. Cell Biol.* **160**, 267–277 (2003).
82. Valero, A. *et al.* Tracking and synchronization of the yeast cell cycle using dielectrophoretic opacity. *Lab Chip* **11**, 1754–1760 (2011).
83. Gossett, D. R. & Carlo, D. Di. Particle focusing mechanisms in curving confined flows. *Anal. Chem.* **81**, 8459–8465 (2009).
84. Pajerowski, J. D., Dahl, K. N., Zhong, F. L., Sammak, P. J. & Discher, D. E. Physical plasticity of the nucleus in stem cell differentiation. *Proc. Natl. Acad. Sci.* **104**, 15619–15624 (2007).

85. Cross, S. E., Jin, Y.-S., Rao, J. & Gimzewski, J. K. Nanomechanical analysis of cells from cancer patients. *Nat. Nanotechnol.* **2**, 780–783 (2007).
86. Hochmuth, R. M. Micropipette aspiration of living cells. *J. Biomech.* **33**, 15–22 (2000).
87. Wang, Y., Shyy, J. Y.-J. & Chien, S. Fluorescence proteins, live-cell imaging, and mechanobiology: seeing is believing. *Annu. Rev. Biomed. Eng.* **10**, 1–38 (2008).
88. Guck, J. *et al.* The optical stretcher: a novel laser tool to micromanipulate cells. *Biophys. J.* **81**, 767–784 (2001).
89. Sharma, V., Park, K. & Srinivasarao, M. Shape separation of gold nanorods using centrifugation. *Proc. Natl. Acad. Sci. U. S. A.* **106**, 4981–4985 (2009).
90. Laurell, T., Petersson, F. & Nilsson, A. Chip integrated strategies for acoustic separation and manipulation of cells and particles. *Chem. Soc. Rev.* **36**, 492–506 (2007).
91. Mach, A. J., Kim, J. H., Arshi, A., Hur, S. C. & Di Carlo, D. Automated cellular sample preparation using a Centrifuge-on-a-Chip. *Lab Chip* **11**, 2827–2834 (2011).
92. Hur, S. C., Henderson-MacLennan, N. K., McCabe, E. R. B. & Di Carlo, D. Deformability-based cell classification and enrichment using inertial microfluidics. *Lab Chip* **11**, 912–920 (2011).
93. Bantscheff, M., Schirle, M., Sweetman, G., Rick, J. & Kuster, B. Quantitative mass spectrometry in proteomics: a critical review. *Anal. Bioanal. Chem.* **389**, 1017–1031 (2007).
94. Mellors, J. S., Jorabchi, K., Smith, L. M. & Ramsey, J. M. Integrated microfluidic device for automated single cell analysis using electrophoretic separation and electrospray ionization mass spectrometry. *Anal. Chem.* **82**, 967–973 (2010).
95. Urban, P. L. *et al.* High-density micro-arrays for mass spectrometry. *Lab Chip* **10**, 3206–3209 (2010).
96. Harvey, T. J. *et al.* Spectral discrimination of live prostate and bladder cancer cell lines using Raman optical tweezers. *J. Biomed. Opt.* **13**, 64004 (2008).
97. Du, E. *et al.* Electric impedance microflow cytometry for characterization of cell disease states. *Lab Chip* **13**, 3903–3909 (2013).
98. Taff, B. M. & Voldman, J. A scalable addressable positive-dielectrophoretic cell-sorting array. *Anal. Chem.* **77**, 7976–7983 (2005).
99. Pratt, E. D., Huang, C., Hawkins, B. G., Gleghorn, J. P. & Kirby, B. J. Rare cell capture in microfluidic devices. *Chem. Eng. Sci.* **66**, 1508–1522 (2011).

100. Asami, K. Characterization of heterogeneous systems by dielectric spectroscopy. *Prog. Polym. Sci.* **27**, 1617–1659 (2002).
101. Markx, G. H., Dyda, P. A. & Pethig, R. Dielectrophoretic separation of bacteria using a conductivity gradient. *J. Biotechnol.* **51**, 175–180 (1996).
102. Becker, F. F. *et al.* Separation of human breast cancer cells from blood by differential dielectric affinity. *Proc. Natl. Acad. Sci.* **92**, 860–864 (1995).
103. Kotnik, T. & Miklavčič, D. Theoretical evaluation of voltage inducement on internal membranes of biological cells exposed to electric fields. *Biophys. J.* **90**, 480–491 (2006).
104. Morgan, H., Sun, T., Holmes, D., Gawad, S. & Green, N. G. Single cell dielectric spectroscopy. *J. Phys. D. Appl. Phys.* **40**, 61 (2007).
105. Vahey, M. D. & Voldman, J. High-throughput cell and particle characterization using isodielectric separation. *Anal. Chem.* **81**, 2446–2455 (2009).
106. Vahey, M. D. & Voldman, J. An equilibrium method for continuous-flow cell sorting using dielectrophoresis. *Anal. Chem.* **80**, 3135–3143 (2008).

Chapter 2

Multiparameter Mechanical and Morphometric Screening of Human Pluripotent Stem cells

This chapter introduces a high-content and label-free method to rapidly phenotype cells based on mechanical and morphological properties. We extract 15 biophysical parameters from cells as they deform in a microfluidic stretching flow field via high-speed microscopy and apply machine learning approaches to develop classification boundaries to discriminate between differentiated and pluripotent stem cells. When employing the full 15 dimensional dataset the technique robustly classifies individual cells based on their pluripotency across 12 different embryonic stem cell lines, with accuracy above 95%. Rheological and morphological properties of cells while deforming were found to be critical for this classification, increasing accuracy from 73% to 95%. This method to quickly assay intrinsic biophysical properties of cells should be broadly applicable to classify changes in cell state, with specific use as a potential low cost tool to screen differentiated cell-based therapies for residual tumor-causing pluripotent cells prior to implantation.

Intrinsic physical properties of cells that reflect underlying molecular structure are indicators of cell state associated with a number of processes including cancer progression, stem cell differentiation, and drug response^{1,2}. Nuclear and cytoplasmic structure or morphology have been one of the main tools for histological detection and classification of cancer. These features include chromatin texture, nuclear shape and cytoplasmic features such as shape and cytoplasmic clearing³⁻⁵. Morphology is also indicative of cell fate and differentiation and self-renewal

capacity. In addition to the expression of certain cell surface markers, cell morphology has been one other major parameter for validation of human embryonic stem cell (hESC) and induced pluripotent stem cell (iPSC) pluripotency⁶⁻⁸. Recent studies have also identified morphological properties that distinguish different subpopulations in highly heterogeneous cultures of mesenchymal stem cells⁹. Morphology-based assays have also been successful in discovery of unique drugs that act on mammalian cells, filamentous fungi and yeasts¹⁰. Observation of pharmacological class-dependent morphological changes in cells has been considered as a complementary strategy for drug discovery⁸. Recent work using morphological screening tools have also linked morphology to activity of a subset of genes^{11,12}. While morphometric measurements provide information on visible cell structures without external probing, internal and optically transparent architectural features can be probed by measuring cell deformation under an applied stress. Cell mechanical stiffness has recently emerged as an indicator of various changes in cells state¹³ including cancer cell function, motility and invasion capacity¹⁴⁻¹⁶. One study found human metastatic cancer cells to be more than 70% softer than neighboring benign reactive mesothelial cells². Embryonic stem cells have also been found to be more deformable than differentiated cells using atomic force microscopy and micropipette aspiration^{17,18}. Therefore, assaying both external and internal architectural properties of cells through the combinations of morphological and mechanical signatures are expected to provide label-free and low cost biomarkers of cell type or state.

Although cell morphological and mechanical characteristics can be indicative of cell state in a variety of cellular processes and conditions, the lack of high-throughput and integrated methods to assay single-cell physical properties, especially from fluid samples, has been a major barrier to adoption of these platforms. For instance, morphological properties can be measured

by automated microscopy, a process that can image tens of cells per second, while cell mechanical properties have been mainly measured using methods such as atomic force microscopy (AFM), optical stretching, or micropipette aspiration, which are single-cell based and manual approaches (< 1 cell / sec)^{2,17,19,20}. These approaches do not allow for flow cytometry-like throughputs ($> 1,000$ cells/sec) and intuitive readouts which allow sampling of rare subpopulations of cells in a reasonable time period. Emerging methods are now able to measure a few mechanical properties from tens to thousands of cells per second^{21,22}, however, these techniques do not currently provide a holistic view of a cell in which multiple internal and visible features of cellular architecture are simultaneously probed. Multiparameter measurements are important in identifying rare populations of cells, in which additional parameters and sample size provide increased statistical confidence in sub-classification²³.

In this study, we perform combined mechanical and morphological phenotyping at rates of $> 1,000$ cells/sec using the deformability cytometry platform. This microfluidic platform was previously used by our group to assay a single mechanical property (deformability) of cells in a variety of body fluids and cell lines, and is based on microfluidic hydrodynamic stretching of cells combined with high speed imaging and automated image analysis (Fig. 1)²¹. Briefly, using inertial focusing, single cells arrive at a junction where they are uniformly stretched while being imaged. Here we implement deformability cytometry as a high-throughput automated tool to assay 15 biophysical properties of cells, including time-dependent mechanical properties, and morphologies across length scales (Fig. 1).

We apply this technique to discriminate pluripotent from differentiated cells in order to screen for the presence of pluripotent stem cells in mixed cultures. Importantly, we discovered that the combination of morphological and mechanical properties provides significantly higher

accuracy compared to either set alone. This multiparameter data set of cell biophysical properties enables us to perform cutting-edge machine learning and statistical data analysis techniques to accurately classify pluripotent stem cells, and provides a new method to characterize cell populations across fields – from cancer biology²⁴ to immunology²¹, in a label-free, and cost-effective manner. In this paper, we show that the multiparametric nature of our technique is particularly useful for detecting rare phenotypes in heterogeneous samples, when the "average cell" properties cannot indicate the variations in cellular state within a population.

Results

Gradual changes in deformability and cell size occur upon differentiation. We first report detailed changes in deformability and size with stem cell differentiation and plot these parameters as 2D single-cell density plots in a fashion similar to flow cytometry (Fig. 1D). While pluripotent cell populations are characterized by a higher deformability and smaller diameter, there is a transition to a larger, less deformable state as cells lose their pluripotency upon a 14-day feeder- and serum-free differentiation (Fig. 2A, SI Video 1 & 2). The decrease in deformability (parameter D3) and increase in size (parameter A) is consistently observed across three hESC lines, although slight variations were detected at later passage numbers of UCLA1 (Fig. 2B). In order to calibrate deformability to commonly reported elasticity measures, we fabricated agarose beads with elastic moduli spanning 0.2-40 kPa, determined by AFM, and measured their deformability in our device (Fig. 3). Using the standard curve generated from the correlation between AFM and DC measurements of these beads (Fig. 3D), pluripotent cells had a median stiffness of ~0.26 kPa which increased to ~1.11 kPa following differentiation. As both size and deformability of cells change, we used the median value of the ratio between cell

deformability and diameter ($D3/A$) as a simple metric of the relative change of cell physical properties with time (Fig. 2C). Normalizing by cell size, which gradually increases from approximately $15\mu\text{m}$ to $18\mu\text{m}$ upon differentiation (Fig. 2D-E), gives a more accurate representation of changes in mechanical properties due to size-dependent differences in applied stress²¹. Although there are distinctive changes in both size and deformability, there is substantial heterogeneity within a population, such that these two parameters alone only allow for classification accuracy of single cells up to 64.6%.

Deformability measures correlate with conventional pluripotency markers. We assessed pluripotency of cells using conventional pluripotency markers including Tra-1-81, and SSEA4 by immunofluorescence flow cytometric analysis at day 0 (Fig. 2F, first column), 3, 6, 9 (Fig. 4A,B) and 12 (Fig. 2F, second column). The expression of Oct4 and Nanog was analyzed by RT-PCR as well (Fig. 2G). The results consistently show down-regulation of pluripotency markers following differentiation as expected. The high correlation ($R^2 \geq 0.9$ for UCLA1 and UCLA2, for the expression of OCT4, NANOG and TRA-1-81) between our mechanical measure and these commonly used pluripotency markers supports the potential of our method as a label-free assay of pluripotency (Fig. 2H and Fig. 4C).

Biophysical properties cluster pluripotent versus differentiated cells across cell lines. We assessed the biophysical features for 9 other hESC lines (a total of 12) before and after two weeks of feeder- and serum-free differentiation. Across cell lines the same trend of increasing size and stiffening upon differentiation was observed (Fig. 5A). The median deformability and median diameter of these 12 cell lines is plotted before (blue) and after (green) differentiation (Fig. 5B). The data shows a 15% increase in size and 20% decrease in deformability following differentiation (Fig. 5C).

Expanding the biophysical dataset beyond size and deformability measures we introduced 13 additional features extracted from cell deformation videos (SI Video 3). These included three additional parameters related to overall cell deformation (D1, D2 and D4), two parameters that report on circularity before and at the junction (C1,C2), two parameters describing normalized strain, removing size dependency from deformability measurements (S1,S2), four morphological parameters before and at the junction (M1-M4) and two parameters reporting on the dynamics of deformation (T1,T2) (refer to Methods section, Fig. 1, Fig. 5E). Measurements of dynamic response to stress is expected to depend on viscous contributors to cellular mechanics, along with elastic properties. Stem cells behaved similar to low viscosity oil droplets, spending longer times deforming in the channel while differentiated cells deformed less and for a shorter time period (Fig. 5E). With these additional parameters, we performed unsupervised clustering based on median parameter values for all 12 cell lines. Linear Discriminant Analysis (LDA) successfully grouped pluripotent cells (day0) separately from differentiated cells (day14) (Fig. 5D). We also performed supervised classification using LDA to quantify how well linear classification can discriminate between day0 versus day14 samples. While classification based on all 15 parameters yielded ~5.28% classification error (misclassification), considering the two size and deformability parameters alone resulted in ~35.4% misclassification. LDA analysis also yielded the most important parameters contributing to the classification. Based on LDA the five most important parameters include deformability (D3), normalized deformability (S1,S2), size (A) and morphology (M1) (Table 1).

Multiple mechanical and morphological parameters improve classification accuracy of single cells. Beyond cell deformability and diameter, we detected up to a 60% change in the median value of other parameters when comparing stem cells and differentiated cell samples,

especially morphology parameters (Fig. 6A). Although differences in medians between pluripotent and differentiated cell populations were detected, at the single-cell level we observed substantial heterogeneity, resulting in a significant overlap between the two populations (Fig. 6B). Therefore, a more information-rich multidimensional dataset was critical to maximize distances in parameter space between the two cell population clusters. To visualize this improvement in clustering we compressed the multidimensional dataset into two or three dimensions and observed a marked reduction in overlap at the single-cell level. We first performed principal component analysis (PCA) on the combined 15-dimensional data sets (day0 and day14 from all cell lines) for which two distinct clusters emerged (Fig. 6C). When we subsequently labeled the groups we found that two (Fig. 6E) or three (Fig. 6D) principal components lead to more separated clusters when compared to deformability-size plots alone. These principle components (PCs) consist of linear combinations of our parameters with PC2 and PC3 again being dominated by parameters A, S1, M1, M3 and D4 (parameters with the largest coefficients) (Table 2). Although each PC might not be informative of a specific parameter, having a large pool of parameters and using dimensionality reduction is a helpful means for summarizing and visualizing the differences between physical properties of different cell populations. Interestingly, as observed in size and deformability plots, two week-differentiated cell populations appear more heterogeneous than day 0 pluripotent cells, displaying a more spread distribution in PC space (Fig. 6D,E). The increased heterogeneity in this population can be better quantified when looking at a similarity matrix for each individual cell, showing a higher similarity between single day0 cells compared to day14 cells (Fig. 6F). The similarity matrix is generated by calculating pairwise Euclidean distances between every

row of the pooled data set (red showing smaller distances or higher similarity). The existence of two distinct clusters in the data is also visible from the similarity matrix.

We next looked at whether there existed a threshold number of parameters that was sufficient to yield accurate single-cell classification. To determine the optimal number of parameters for successful clustering of the two classes (pluripotent versus differentiated cells), we performed unsupervised clustering by expectation maximization for Gaussian mixture (EMGM) models considering different numbers of parameters. As expected, increasing the number of parameters resulted in increased clustering accuracy across the 12 cell lines separately (Fig. 6G, colored lines). Similarly, pooled data from all cell lines at day 0 and day 14 yielded increased clustering accuracy with increasing number of parameters (Fig. 6G, black line). Although adding more pieces of information enables more accurate clustering, further increasing the number of parameters from 9 to 15 parameters resulted in only a 2.35% reduction in clustering error, compared to a 20.2% reduction from 2 to 9 parameters. This could be due to the fact that not all the features extracted from the images are linearly independent. In fact, the correlation coefficients between parameters show partial dependence between a few parameters as expected (Table 3).

Using these same 9 most important features, we next trained a support vector machine (SVM) classifier to distinguish between single pluripotent and differentiated cells with 93% classification accuracy. When increasing to 15 parameters, classification accuracy increased only to 95%. A 5-fold cross validation technique was first used to train the classifier and classification accuracy was calculated as the fraction of data points that were classified correctly. The area under the curve (AUC) of the sensitivity vs. specificity receiver operating characteristic (ROC) was ~0.97 using all 15 parameters, showing an exceptional classifier performance (Fig.

6H). SVM recursive feature elimination (RFE) was then used to determine whether a smaller number of parameters could yield high classification accuracy as well. The parameters were removed one at a time depending on their contribution to classification (Fig. 6I). Again, we observed a significant decrease in classification accuracy and AUC upon removing 6 or more parameters (Fig. 6J).

Biophysical identification of pluripotent cells spiked into differentiated cell batches. We next validated the multiparameter SVM classifier using a separate validation data set. We performed several spiking experiments by mixing pluripotent cells (day 0) with cells after 12 days of serum-free differentiation. For comparison, three flow cytometry-like gating strategies were first applied to assess the purity of hESC cells in the mixed samples using only deformability and initial cell diameter (parameters D3 and A) (Fig. 7A). We also performed gating across a line that divided the small deformable population from the larger stiff population of differentiated cells (in purple). Lastly, we gated the cells only based on their diameter to understand the contribution of the deformability measure on the ability to detect sample purity. The purity measured by the three gating methods versus the actual mixing ratios is presented in Fig. 7B. While all three methods correlate well with the actual purity, “*Diagonal gating*” and “*day0 gating*” are more sensitive to impurities achieving a slope closer to an ideal 1. With the analytical sensitivity achieved, the minimum impurity difference that the gating can predict is around 6.2% considering a standard deviation of 4.4% within the gate from sample to sample. In comparison to simple gating on two parameters, machine learning-based classification with additional parameters leads to improved detection of spiked sub-populations.

When all 15 parameters were used as part of the SVM classifier, improved classification was achieved (Fig. 7C, second row: cells classified as pluripotent in blue and differentiated in green). Using multiparameter analysis, we can detect as small as a 0.7% impurity difference across samples (Fig. 7D). Support vectors clearly define a boundary when visualizing the data in 3D with test data (spiked cells) overlapping well with the training data from all 12 cell lines at day 0 - Class1 and day 14 - Class2 for the 5 different spiking ratios. Upon removing parameters using RFE, the sensitivity of our sub-population estimation decreased and the minimum distinguishable sample impurity increased (Fig. 7D, F, Fig. 8).

Simultaneous biophysical and molecular analysis shows high correlation between pluripotency and deformability at single cell level. Here, we have developed a system that can perform flow cytometry and deformability cytometry at the same time on single cells. Using this setup we show that the population of feeder mouse embryonic fibroblasts (mEFs) in the culture of hESCs are stiffer, smaller and are not labeled by TRA-1-81 pluripotency marker (Fig. 12).

Discussion

Our results show that the combination of mechanical and morphological properties can be an accurate label-free biomarker of cell state. This is demonstrated in the detection of a pluripotent state across 12 embryonic stem cell lines. Importantly, mechanical parameters obtained upon hydrodynamic stretching, such as deformability and rate of deformation, were key parameters that increased the accuracy of pluripotency classification substantially, from 0.74 when considering morphological parameters alone to 0.95 (Fig.9). We also showed the capability of our system to classify mixed populations accurately down to less than 1% using machine learning. Compared to published techniques to measure cell mechanics^{12,14,25} our integrated

method provides throughput improvements while expanding the number of biophysical parameters 2-3 fold, enabling increased information content and accuracy. In fact, our system operates at throughputs similar to flow cytometry (>1000 cells/sec) but without labeling or sample preparation.

Such a label-free approach is specifically important in the field of regenerative medicine, since heterogeneity in the culture system is a challenge for repeatability. Furthermore, assessment of pluripotency in human pluripotent stem cells currently requires teratoma formation in mice. This is not traditionally a quantifiable assay, and merely provides a binary yes-no result. A simple label-free method to evaluate cultures for self-renewal potential or level of differentiation will enable low cost quality control (QC) of stem cells with robust quantifiable measurements. It is also possible that these types of measurements may ultimately enable a diagnostic for differentiation potential in future studies. In particular, based on the machine learning approaches presented here we can create a classifier that identifies normal pluripotent cultures that yield the best differentiation potential. One could then screen for cultures that fall outside of this validated state. For example, our approach is able to discriminate a later passage pluripotent stem cell culture from an earlier passage (Fig. 2B).

Clinically, there is a critical need to remove rare failed to differentiate pluripotent cells in differentiated cultures for upcoming cell-based therapies. Teratoma formation following injection of pluripotent cells, has been reported in several pre-clinical studies, and is a major barrier to successful clinical translation^{26,27}. Since implantation of pluripotent cells causes tumor formation *in vivo*, only their differentiated progeny are being applied for clinical transplantation^{28,29}. In the absence of optimized differentiation protocols for many lineages, the transplanted cell population ends up as a mixture of differentiated progenitors and in some cases

failed to differentiate pluripotent cells. The high risk of injecting failed to differentiate pluripotent cells reinforces the need for rigorous characterization of ESC-derived cell products before any clinical applications³⁰. Previous studies show that increasing purity of hESC-derived cardiomyocytes to around 85% prevented teratoma formation four weeks after injection into immunodeficient rats³¹ and the demonstrated sensitivity seems to be adequate to perform fast screening for culture purity at this level.

Methods to sort out these pluripotent sub-populations are also needed. Currently, QC and sorting can be done using traditional fluorescence activated cell sorting techniques, however the addition of antibody labels to cell surface proteins and the required sample preparation has a substantial associated regulatory burden that has been a roadblock to using these approaches translationally. Although, we do not currently demonstrate sorting in our system, we anticipate that this functionality will be achievable in the future using hardware-based image analysis³² and traditional flow cytometry sorting hardware.

The presented label-free method may report on changes in nuclear architecture upon stem cell differentiation. As the largest eukaryotic organelle, the nucleus plays an important role in cell size and deformability and chromatin structure is suggested to be one of the major determinants of nuclear size and stiffness³³. Interestingly, chromatin and nuclear lamina both undergo extensive changes during differentiation and both are linked to changes in cell mechanical properties. Several epigenetic processes define the structure of chromatin and result in a global chromatin condensation level, which can determine the global transcriptional activity of a cell. In stem cells, regulation of pluripotency genes and their inactivation upon differentiation are linked with extensive epigenetic programming and chromatin rearrangement^{34,35} (Fig. 11). Several epigenetic modifications including global DNA hypermethylation³⁶ and

decrease in histones H3 and H4 acetylation^{37,38} lead to substantial chromatin reorganization, which is critical for transcriptional reprogramming during stem cell differentiation. ESCs are known to have more open euchromatin than differentiated cells^{37,39}, which has been associated with a reduction in nuclear viscosity and stiffness⁴⁰. Isolated nuclei treated with ethylenediaminetetraacetic acid (EDTA), (a chelating agent that decondenses chromatin through binding divalent cations) showed significant expansion of the nuclear envelope, increase in nuclear size and reduction in the stiffness of the nucleus, while imposing chromatin condensation through addition of divalent cations resulted in nuclear contraction and greater nuclear stiffness^{17,41}. As one of the major determinants of nuclear structure and mechanics, A-type lamins are not expressed in ESCs and are only present in differentiated cells. Lamin-A depleted human epithelial cells also showed lower nuclear stiffness compared to normal cells¹⁷. Chromatin and nuclear membrane elasticity are expected to be dominant contributors to deformability metrics because of the large stresses that we can apply (Fig. 10) which result in corresponding large strains to the whole cell and nucleus. Our dynamic measurements of deformation at high shear rates also interrogate viscous properties including the ability of chromatin to flow within the nucleus, in which tightly wound heterochromatin foci are expected to lead to a decreased rate of deformation. Chromatin rearrangements and lamin expression which are critical for cell development and differentiation are also involved in many cellular processes, human conditions and diseases including aging, cancer and cardiovascular disease^{4,34,42}.

Beyond differentiation, our technique can be used to measure other cell states, particularly when nuclear architectural changes are prevalent. Aberrant epigenetic regulation, causing undesirable gene silencing or expression, has also been observed frequently in cancer cells, and the level of chromatin condensation controlled by these epigenetic modifications is found to considerably

alter the structural and physical properties of chromatin and the cell nucleus. In fact nuclear shape and structure is still one of the main tools for histological detection and classification of cancer ⁴³. However, current cytomorphological analysis is labor-intensive and qualitative, creating a need for automated, quantitative alternatives ²⁴. The additional mechanical and morphological properties we can assay here are poised to accelerate the development of physical biomarkers across a range of fields, particularly impacting immunology and cancer biology, in which whole-cell architectural changes are critical aspects of disease processes.

Materials and Methods

Deformability cytometry device. The deformability cytometer is a microfluidic device designed for single-cell analysis of cell mechanical properties (Fig. 1A)²¹. Cells in suspension are delivered at high rates to an extensional flow which is used to stretch the cells to high strains (Fig. 1B). Functioning in an inertial regime (channel Reynolds number $Re \sim 100$), inertial focusing positions cells precisely before stretching (Fig. 10A) ^{44,45}, which ensures a more uniform three-dimensional force on cells of the same size. Cell viscoelastic properties then determine to what extent a cell deforms. This deformation is continuously imaged using high-speed microscopy (Fig. 1C) and automated image analysis is conducted to extract cell biophysical properties after transforming images from a polar to a Cartesian coordinate system (SI video 4). Populations of individual cells are plotted based on these parameters in a color density format (Fig. 1E). Finite element simulations show that for a simplified model of the system the force applied to a cell at the junction is on the order of 10^{-4} N (Fig. 1D, Fig. 10B), which is almost three orders of magnitude higher than that applied by conventional methods like AFM or micropipette aspiration ⁴⁶. The high force allows for a very short deformation timescale

(around 2 μ s) and large deformations, resulting in processing of more than 1000 cells per second and probing of deep intracellular structures like the nucleus.

Microfluidic devices were fabricated using common polydimethylsiloxane (PDMS) replica molding processes. Briefly, standard lithographic techniques were used to produce a mold from a silicon master spin-coated with SU-8 photoresist. PDMS chips were produced from this mold using Sylgard 184 Elastomer Kit (Dow Corning Corporation) and a cross-linker to polymer ratio of 1:10. To enclose the channels, PDMS and glass were both activated by air plasma (Plasma Cleaner, Harrick Plasma, 500 mTorr, 30 sec) before being bonded together. The device contained 20 μ m filters to avoid entrance of cell clusters or dust followed by curving channels to ensure inertial focusing and a junction that provides an extensional flow. Channel width before and after extensional region was 67 μ m and the height of the channel was 30 μ m. The positioned cells arrived one at a time at an extensional flow, were stretched and left the junction from either of the two outlets on the top or bottom. The extensional region was continuously imaged using high-speed microscopic imaging.

Cell culture and sample preparation. The biophysical properties of human embryonic stem cells (hESCs) (day 0) were analyzed by deformability cytometry before and after feeder and serum-free non-specific induction to differentiation for up to 12 days. Twelve lines of human ESCs, (UCLA1-12) were maintained in DMEM high glucose with 20% knockout serum replacer supplemented with 20ng/ml of bFGF, and grown on mitomycin-treated mouse embryo fibroblasts ⁴⁷. Culture on 1% gelatin coated dishes without feeder cells in DMEM high glucose with 20% FBS resulted in a gradual differentiation ⁴⁸. Single cell suspensions were prepared by 5 min treatment with 1X trypsin EDTA followed by detachment from the dish, aspiration, and suspension in culture media. For each condition and each replicate three sets of samples were

prepared for (i) live cell flow cytometry analysis, (ii) RT-PCR and (iii) deformability cytometry. For deformability cytometry the cell suspension was prepared immediately prior to the test (<1 hour). Cell suspensions were injected into the device, at a concentration of 200,000 to 500,000 cells/mL, using a syringe pump (Harvard Apparatus PHD 2000) and a glass syringe (Hamilton), at flow rate of 1000 μ L/min.

High-speed imaging and data extraction. Image sequences from cells at the extensional flow region magnified with a 10 \times objective (Nikon Japan 10x/0.30 on a Nikon Eclipse Ti inverted microscope) were recorded at ~520,000 frames/s using a Phantom v7.11 high-speed camera and the Phantom Camera Control Software (Vision Research Inc.). Automated image analysis was conducted on the gathered cell deformation images to track cells, and to extract 15 parameters based on cell biophysical properties (SI Video 3). The cell tracking and analysis software was previously developed in our lab ²¹. The custom image analysis script performs image processing and data collection on each 1.5 second experiment totaling 780,000 frames, with expected occurrences of 1,000 to 5,000 cells.

The following parameters were extracted from the captured high-speed images:

(A) Initial cell size, before reaching the junction by calculating the maximum diameter of the cell within 30 degrees from the vertical axis.

(D1) Deformation of cells at the junction, accounting for pre-junction perceived deformations due to morphology.

(D2) Deformation of cells at the junction defined as: (long axis-short axis) / (long axis+short axis)

(D3) Maximum deformability at the junction defined as the maximum cell diameter within 30 degrees from the vertical axis divided by the minimum diameter within 30 degrees from the horizontal axis.

(D4) The maximum vertical diameter at the junction.

(S1) Maximum deformability at the junction normalized by cell perimeter before deformation.

(S2) Relative strain defined as the ratio of parameters D3 and A.

(C1) Circularity defined as cell perimeter/area ratio at the maximum deformation.

(C2) Circularity defined as the perimeter/area ratio prior to deformation in the channel.

(M1) Morphology extracted prior to the junction measured by the difference between the area under the curve of the cell border (trace) and its moving average. This parameter indicates cell roughness.

(M2) Morphology metric extracted prior to deformation as defined by the number of intersections of the trace and the moving average. This parameter indicates regularity of the surface.

(M3) Morphology metric extracted during deformation is defined as in M1.

(M4) Morphology metric extracted during deformation is defined as in M2.

(T1) Length of deformation time between when the cell enters the junction until it leaves.

(T2) The rate of change in deformation at the junction defined by change in vertical cell diameter over the first 5 frames of the deformation.

Numerical simulations and force approximation. To estimate fluid pressure and the force applied on cells at the junction, we simulated steady-state pressure and force using a numerical model that solves the 3D incompressible Navier-Stokes equations. To achieve this, we assumed that the position of the cell is fixed at the center of the junction and the cell is not deforming or

rotating in time. Using this method, we conducted a series of simulations for various inlet flow rates specified as input velocity boundary conditions.

Multiparameter analysis.

Expectation maximization. The expectation maximization process was initialized by k-means clustering. Hierarchical search was used to remove parameters that have the least contribution to clustering first. Briefly, exhaustive search was performed at each iteration to find the parameter that yields the lowest clustering error after being removed. This test was performed for data gathered from individual cell lines at day 0 and after two weeks of differentiation. Clustering error was defined as within class variations over between class variations:

$$EMGM \text{ clustering error} = \frac{\sum_{i \in C1} x_i - m_{C1}}{\sum_{i \in C1} x_i - m_{C2}} + \frac{\sum_{j \in C2} x_j - m_{C2}}{\sum_{j \in C2} x_j - m_{C1}} \quad (x_i, x_j : \text{single data points, } C1 : \text{class number (pluripotent cells), } C2 : \text{class number 2 (differentiated cells). } m_{C1}, m_{C2} : \text{means of classes 1 and 2}).$$

Support vector machine and recursive feature elimination. SVM with a linear kernel and 5-fold cross validation was used on the pooled data from all 12 cell lines to test the accuracy of classification. SVMs were implemented using the *SVMTrain* and *SVMclassify* functions of MatlabTM. *Perfcurve* function was then used to compute the ROC curves for the classifier. The ROC curves are plotted as *True positive rate* or sensitivity defined as: number of true positive instances/(number of true positive instances+number of false negative instances) versus *False positive rate* or 1-specificity, defined as: number of false positive instances/(number of true negative instances+number of false positive instances). Starting with all 15 parameters, the

parameters were eliminated hierarchically to minimize misclassification at each iteration. All the data from 12 cell lines at day0 and day14 was used as the training set for SVM and the spiked samples were analyzed for the ratio of single cells belonging to each class.

Agarose bead fabrication. A microfluidic droplet generator platform was used to generate agarose beads with different elastic moduli ⁴⁹ (Fig. 3B). The pre-gel solution was prepared by melting and diluting two low-gelling temperature agarose types: Agarose Type IX and IXA (Sigma) at different dilutions (0.5, 1 and 2 wt%) in DI water. The oil phase consisted of mineral oil (Sigma) mixed with 2% Span80 (Sigma). The bead generation process was performed on an incubated microscope (at 40°C) to prevent agarose gelation. After capturing beads (10-20µm in diameter), the solution containing oil and surfactant was incubated at 4°C overnight to allow the gelation of agarose droplets. The beads were then resuspended in DI water for analysis.

Elastic modulus characterization. Elastic moduli of the two agarose gel types were measured in bulk at different dilutions. Force-displacement curves were obtained from a Bruker Catalyst AFM aligned above a Leica inverted microscope. Model SNL-D cantilevers (Bruker, spring constant: 0.06 N/m) generated indentation curves in force control mode. Elastic modulus was extracted by fitting the Hertz model to our acquired data.

Immunofluorescence microscopy. Human embryonic stem cells and mouse 3T3 fibroblasts were fixed in 4% paraformaldehyde (Fisher Scientific, US) in phosphate-buffered saline (PBS, Invitrogen) at room temperature for 20 minutes. Cells were then washed three times in PBS and then permeabilized in 0.1% Triton X-100 in PBS for 10 minutes. Cells were washed three times again and incubated with goat anti-Lamin A/C (Santa Cruz) diluted 1:400 and rabbit anti-Histone H3K9me1me2me3 (Active Motif) diluted 1:500 in 1%BSA for 1 hour at room temperature. Cells

were washed three times in PBS and then incubated with a 1:400 dilution of Cy5-labeled chicken anti goat and 1:400 FITC-labeled mouse anti-rabbit and 1:10000 Hoechst 33342 (Invitrogen) for one hour. The cells were then washed one last time in PBS and were mounted in Prolong antifade mounting medium (Invitrogen) on glass slides for confocal imaging.

Flow Cytometry. Expression of cell surface pluripotency antigens was characterized using flow cytometry. After harvesting cells by trypsin-EDTA, cells were washed in cold 1% BSA in PBS, were passed through a cell strainer (40 μ m Nylon membrane BD Falcon) and resuspended to approximately 10⁶ cells/mL of cold BSA/PBS solution. Cell samples were incubated with optimal dilution of DAPI, PE-labeled anti TRA-1-81 (BD Biosciences), and APC-labeled anti SSEA4 (R&D systems) on ice in the dark for 1 hour. The cells were then washed and resuspended in cold PBS/BSA solution and analyzed within 30 minutes. Data was analyzed using FlowJo software (Treestar, Inc., San Carlos, CA).

Quantitative real-time PCR. Total RNA was extracted and purified using a PureLink™ RNA Mini kit (Invitrogen, USA) per manufacturer recommendations. PCR was carried out for 40 cycles and relative expression level for each target gene was evaluated using 2^{- $\Delta\Delta$ Ct} method. To obtain the Δ Ct values, the Ct values of target genes were normalized by the Ct values of GAPDH.

Bibliography

1. Settleman, J. Tension precedes commitment—even for a stem cell. *Mol. Cell* **14**, 148–150 (2004).
2. Cross, S. E., Jin, Y.-S., Rao, J. & Gimzewski, J. K. Nanomechanical analysis of cells from cancer patients. *Nat. Nanotechnol.* **2**, 780–783 (2007).
3. Bigras, G. *et al.* Interobserver concordance in the assessment of features used for the diagnosis of cervical atypical squamous cells and squamous intraepithelial lesions (ASC-US, ASC-H, LSIL and HSIL). *Cytopathol. Off. J. Br. Soc. Clin. Cytol.* **24**, 44–51 (2013).
4. Zink, D., Fischer, A. H. & Nickerson, J. A. Nuclear structure in cancer cells. *Nat. Rev. cancer* **4**, 677–687 (2004).
5. Millot, C. & Dufer, J. Clinical applications of image cytometry to human tumour analysis. *Histol. Histopathol.* **15**, 1185 (2000).
6. Thomson, J. A. *et al.* Embryonic stem cell lines derived from human blastocysts. *Science* (80-.). **282**, 1145–1147 (1998).
7. Amit, M. *et al.* Clonally derived human embryonic stem cell lines maintain pluripotency and proliferative potential for prolonged periods of culture. *Dev. Biol.* **227**, 271–278 (2000).
8. Takahashi, K. *et al.* Induction of pluripotent stem cells from adult human fibroblasts by defined factors. *Cell* **131**, 861–872 (2007).
9. Haasters, F. *et al.* Morphological and immunocytochemical characteristics indicate the yield of early progenitors and represent a quality control for human mesenchymal stem cell culturing. *J. Anat.* **214**, 759–767 (2009).
10. Futamura, Y. *et al.* Morphobase, an encyclopedic cell morphology database, and its use for drug target identification. *Chem. Biol.* **19**, 1620–30 (2012).
11. Yin, Z. *et al.* A screen for morphological complexity identifies regulators of switch-like transitions between discrete cell shapes. *Nat. Cell Biol.* **15**, 860–71 (2013).
12. Goranov, A. I. *et al.* Changes in cell morphology are coordinated with cell growth through the TORC1 pathway. *Curr. Biol.* (2013).
13. Di Carlo, D. A Mechanical biomarker of cell state in medicine. *J. Lab. Autom.* **17**, 32–42 (2012).
14. Xu, W. *et al.* Cell stiffness is a biomarker of the metastatic potential of ovarian cancer cells. *PLoS One* **7**, e46609 (2012).

15. Suresh, S. *et al.* Connections between single-cell biomechanics and human disease states: gastrointestinal cancer and malaria. *Acta Biomater.* **1**, 15–30 (2005).
16. Swaminathan, V. *et al.* Mechanical stiffness grades metastatic potential in patient tumor cells and in cancer cell lines. *Cancer Res.* **71**, 5075–5080 (2011).
17. Pajerowski, J. D., Dahl, K. N., Zhong, F. L., Sammak, P. J. & Discher, D. E. Physical plasticity of the nucleus in stem cell differentiation. *Proc. Natl. Acad. Sci.* **104**, 15619–15624 (2007).
18. Chowdhury, F. *et al.* Material properties of the cell dictate stress-induced spreading and differentiation in embryonic stem cells. *Nat. Mater.* **9**, 82–88 (2009).
19. Guck, J. *et al.* Optical deformability as an inherent cell marker for testing malignant transformation and metastatic competence. *Biophys. J.* **88**, 3689–3698 (2005).
20. Sraj, I. *et al.* Cell deformation cytometry using diode-bar optical stretchers. *J. Biomed. Opt.* **15**, 47010 (2010).
21. Gossett, D. R. *et al.* Hydrodynamic stretching of single cells for large population mechanical phenotyping. *Proc. Natl. Acad. Sci.* **109**, 7630–5 (2012).
22. Byun, S. *et al.* Characterizing deformability and surface friction of cancer cells. *Proc. Natl. Acad. Sci.* **110**, 7580–7585 (2013).
23. Andersson, H. & van den Berg, A. Microtechnologies and nanotechnologies for single-cell analysis. *Curr. Opin. Biotechnol.* **15**, 44–49 (2004).
24. Tse, H. T. *et al.* Improved Diagnosis of Malignant Pleural Effusions by Single-Cell Mechanophenotyping. *Sci. Transl. Med.* **In review**, (2013).
25. Remmerbach, T. W. *et al.* Oral cancer diagnosis by mechanical phenotyping. *Cancer Res.* **69**, 1728–1732 (2009).
26. Cunningham, J. J., Ulbright, T. M., Pera, M. F. & Looijenga, L. H. J. Lessons from human teratomas to guide development of safe stem cell therapies. *Nat. Biotechnol.* **30**, 849–857 (2012).
27. Tang, C. *et al.* An antibody against SSEA-5 glycan on human pluripotent stem cells enables removal of teratoma-forming cells. *Nat. Biotechnol.* **29**, 829–834 (2011).
28. Swijnenburg, R.-J. *et al.* Embryonic stem cell immunogenicity increases upon differentiation after transplantation into ischemic myocardium. *Circulation* **112**, I–166 (2005).

29. Wakitani, S. *et al.* Embryonic stem cells injected into the mouse knee joint form teratomas and subsequently destroy the joint. *Rheumatology* **42**, 162–165 (2003).
30. Adewumi, O. *et al.* Characterization of human embryonic stem cell lines by the International Stem Cell Initiative. *Nat. Biotechnol.* **25**, 803–816 (2007).
31. Laflamme, M. A. *et al.* Cardiomyocytes derived from human embryonic stem cells in pro-survival factors enhance function of infarcted rat hearts. *Nat. Biotechnol.* **25**, 1015–1024 (2007).
32. Lee, D. *et al.* A HARDWARE ACCELERATED APPROACH FOR IMAGING FLOW CYTOMETRY.
33. Dahl, K. N., Kahn, S. M., Wilson, K. L. & Discher, D. E. The nuclear envelope lamina network has elasticity and a compressibility limit suggestive of a molecular shock absorber. *J. Cell Sci.* **117**, 4779–4786 (2004).
34. Ballas, N., Grunseich, C., Lu, D. D., Speh, J. C. & Mandel, G. REST and its corepressors mediate plasticity of neuronal gene chromatin throughout neurogenesis. *Cell* **121**, 645–657 (2005).
35. Joffe, B., Leonhardt, H. & Solovei, I. Differentiation and large scale spatial organization of the genome. *Curr. Opin. Genet. Dev.* **20**, 562–569 (2010).
36. Bibikova, M. *et al.* Human embryonic stem cells have a unique epigenetic signature. *Genome Res.* **16**, 1075–1083 (2006).
37. Meshorer, E. & Misteli, T. Chromatin in pluripotent embryonic stem cells and differentiation. *Nat. Rev. Mol. cell Biol.* **7**, 540–546 (2006).
38. Lee, J., Hart, S. R. L. & Skalnik, D. G. Histone deacetylase activity is required for embryonic stem cell differentiation. *Genesis* **38**, 32–38 (2004).
39. Bhattacharya, D., Talwar, S., Mazumder, A. & Shivashankar, G. V. Spatio-Temporal Plasticity in Chromatin Organization in Mouse Cell Differentiation and during *Drosophila* Embryogenesis. *Biophys. J.* **96**, 3832–3839 (2009).
40. Dahl, K. N., Ribeiro, A. J. S. & Lammerding, J. Nuclear shape, mechanics, and mechanotransduction. *Circ. Res.* **102**, 1307–1318 (2008).
41. Dahl, K. N., Engler, A. J., Pajerowski, J. D. & Discher, D. E. Power-law rheology of isolated nuclei with deformation mapping of nuclear substructures. *Biophys. J.* **89**, 2855–2864 (2005).
42. Wu, H. & Sun, Y. E. Epigenetic regulation of stem cell differentiation. *Pediatr. Res.* **59**, 21R–25R (2006).

43. Zwerger, M., Ho, C. Y. & Lammerding, J. *Nuclear mechanics in disease. Annu. Rev. Biomed. Eng.* **13**, 397–428 (2011).
44. Di Carlo, D., Irimia, D., Tompkins, R. G. & Toner, M. Continuous inertial focusing, ordering, and separation of particles in microchannels. *Proc. Natl. Acad. Sci. U. S. A.* **104**, 18892–7 (2007).
45. Di Carlo, D., Wu, L. Y. & Lee, L. P. Dynamic single cell culture array. *Lab Chip* **6**, 1445–1449 (2006).
46. Rowat, A. C., Lammerding, J., Herrmann, H. & Aebi, U. Towards an integrated understanding of the structure and mechanics of the cell nucleus. *Bioessays* **30**, 226–236 (2008).
47. Clark, A. T. *et al.* Spontaneous differentiation of germ cells from human embryonic stem cells in vitro. *Hum. Mol. Genet.* **13**, 727–739 (2004).
48. Ozolek, J. A., Jane, E. P., Krowsoski, L. & Sammak, P. J. Human embryonic stem cells (HSF-6) show greater proliferation and apoptoses when grown on glioblastoma cells than mouse embryonic fibroblasts at day 19 in culture: comparison of proliferation, survival, and neural differentiation on two different feeder c. *Stem Cells Dev.* **16**, 403–412 (2007).
49. Eun, Y.-J., Utada, A. S., Copeland, M. F., Takeuchi, S. & Weibel, D. B. Encapsulating bacteria in agarose microparticles using microfluidics for high-throughput cell analysis and isolation. *ACS Chem. Biol.* **6**, 260–266 (2010).

Figures

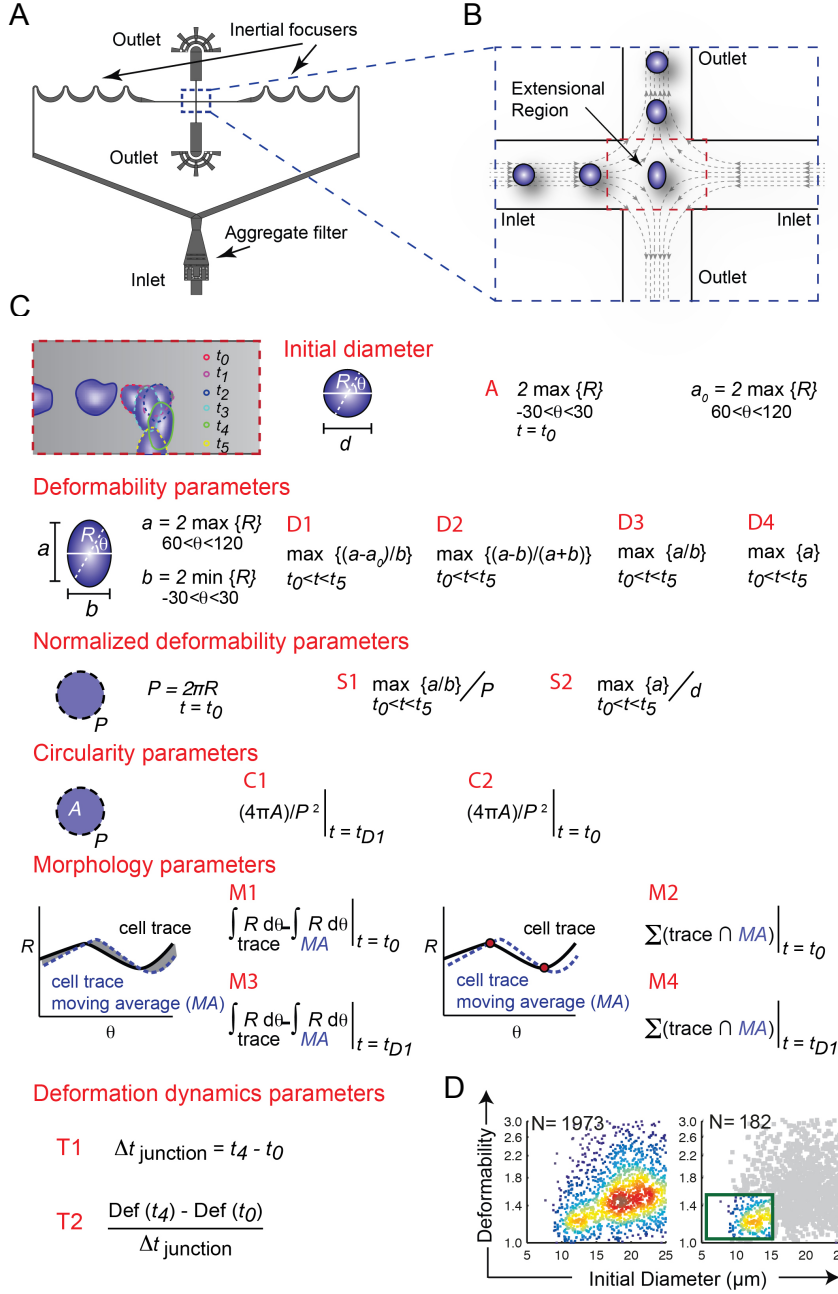


Figure 1. Deformability cytometry device. Device schematic (A) shows the aggregate filter at the inlet, the curved channels facilitating inertial focusing and the extensional region magnified in b.

(B) The extensional region is continuously imaged by high-speed camera. (C) A series of overlapped images show how a cell deforms as it enters the extensional region. Several parameters including initial diameter, deformability, circularity, morphology, stretching period and strain rate are captured for each cell using image processing. The deformability and cell size parameters captured from cells are depicted as color density plots. (D) Gating can further be used to identify specific cell populations.

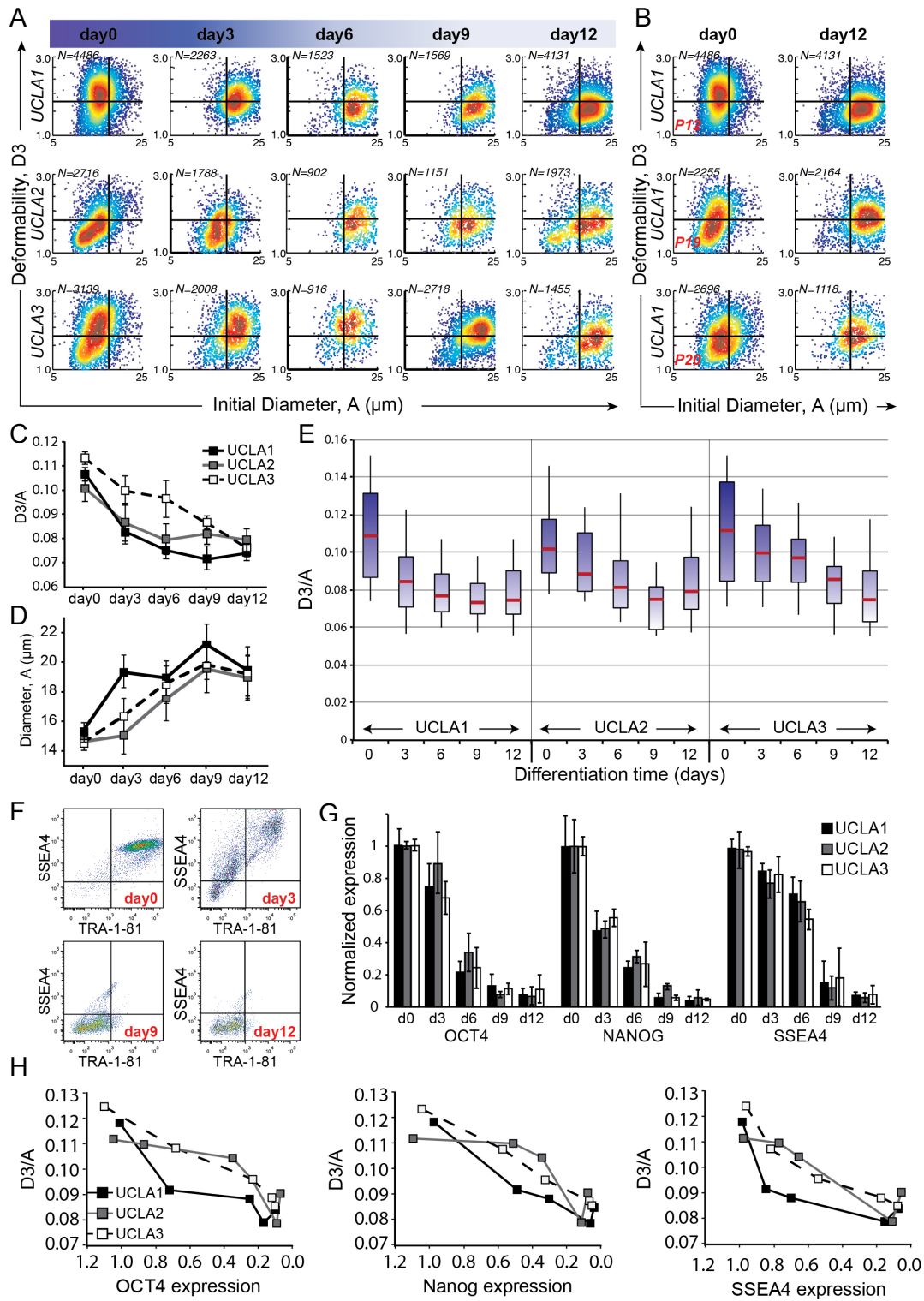


Figure 2. As stem cells differentiate mechanical properties and pluripotency markers shift (gates are set at “Initial Diameter” =17 μ m and “Deformability” =1.6)(A). Color density plots (red-to-blue indicates high-to-low density) of single cell deformability and size measurements of hESCs and hESCs differentiated up to 12 days for UCLA1, UCLA2 and UCLA3 cell lines (rows one to three respectively). (B) A stiffer mechanophenotype is seen at higher passage numbers for the undifferentiated UCLA1 cell line. (C) The median value of deformability / diameter (D3/A) gradually decreases (error bars show standard deviation for n=3 samples). (D) Cells become larger as they differentiate. (E) The range of D3/A first decreases before increasing at 12 days in differentiated cells. (F) Reduction in TRA-1-81 and SSEA4 are observed upon differentiation by flow cytometry. (G) Normalized deformability (D3/A) correlates with traditional markers of pluripotency that decrease with differentiation (H).

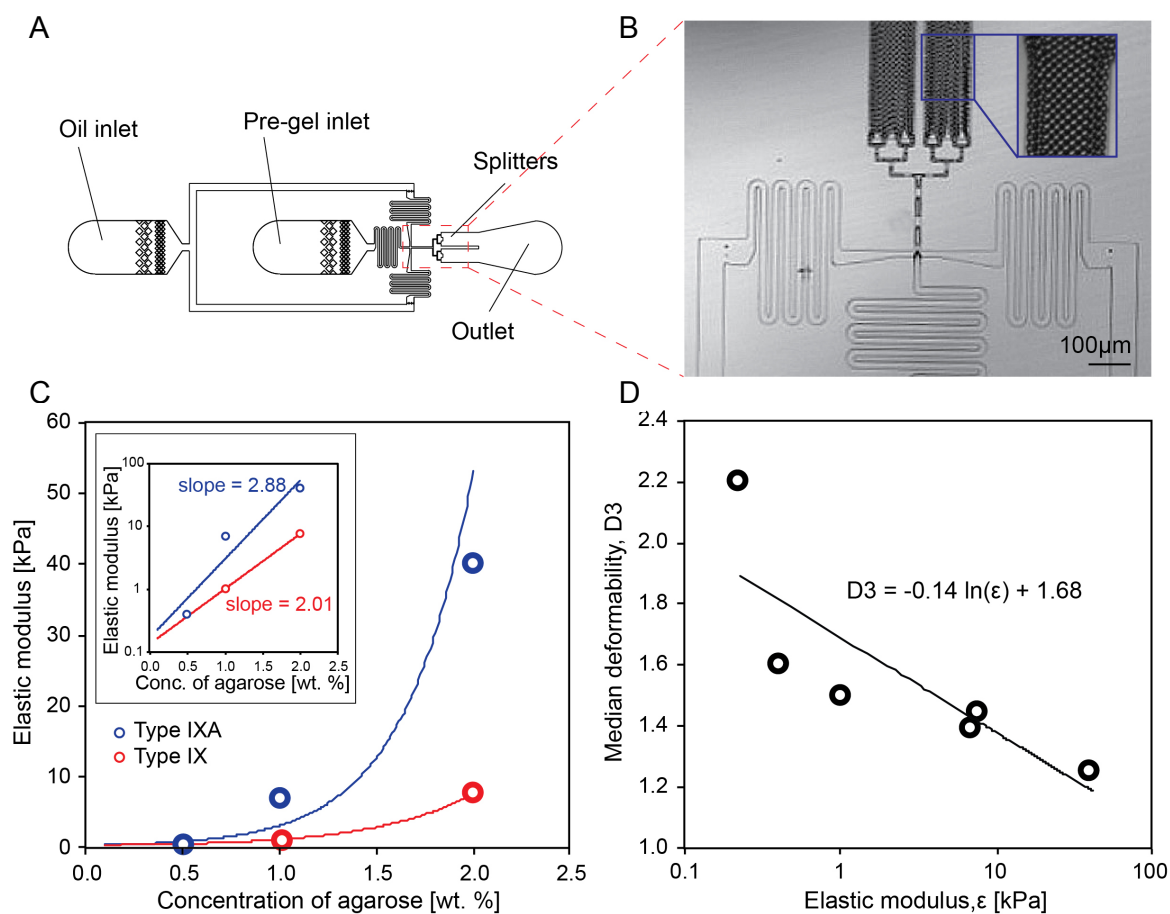


Figure 3. Agarose calibration particles. (A) A microfluidic droplet-generating platform was used to generate agarose gel particles with different stiffness. (B) The generation of agarose droplets in oil/surfactant solution which are subsequently gelled upon refrigeration. (C) The elastic modulus of different concentrations of two low-gelling temperature agarose gels were measured in bulk using AFM. (D) Using DC measurements, the median deformability of beads are plotted versus their mechanical stiffness. This calibration curve can be used to translate deformability measurements to conventional cell stiffness measurements.

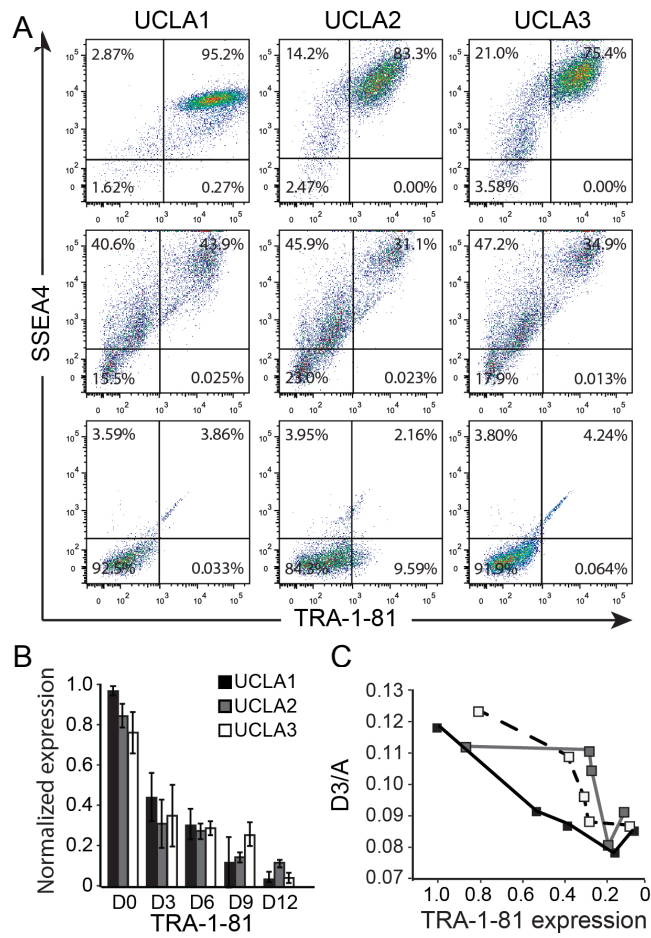


Figure 4. (A) Down-regulation of SSEA4 and TRA-1-81 pluripotency markers was observed by flow cytometry for UCLA1-3 at day0 (first row), day3 (second row) and day12 (third row). (B) The largest change is seen within the first 3 days, but levels continue to decrease up to 12 days. (C) Correlation is observed between the expression of these conventional pluripotency measures and normalized deformability.

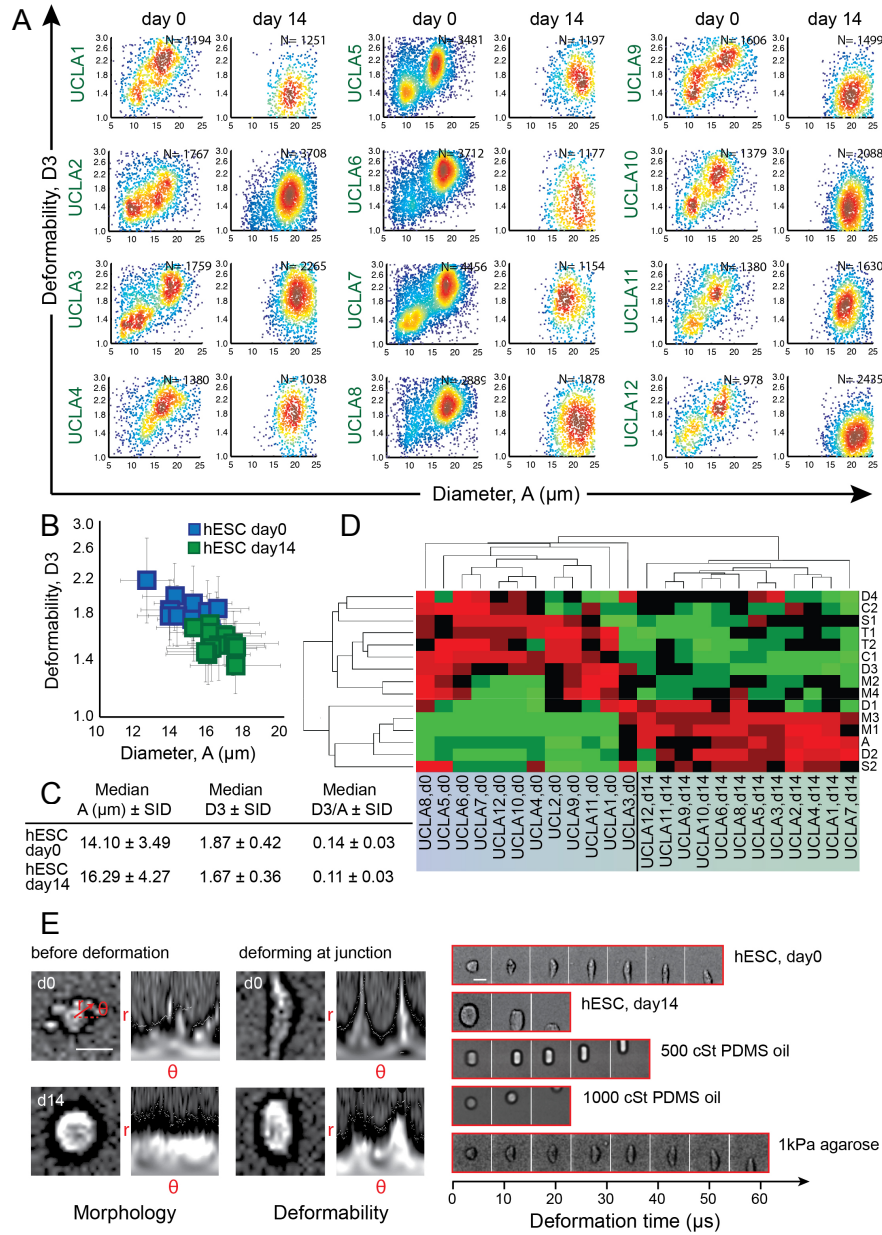


Figure 5. Morphological and mechanical properties are indicative of pluripotency at the population level across 12 cell lines. (A) Two-dimensional density scatter plots show an increase in cell size and decrease in cell deformability after differentiation. (B) Median deformability and size with semi-interquartile deviation (SID) as error bars are plotted for each cell line. (C)

Statistics for the 12 cell line samples are tabulated. The SID value is calculated for median values of the parameters across the 12 cell lines. (D) Using all 15 parameters including cell initial diameter (A), four deformability (D1-D4), two circularity (C1,C2), two strain (S1,S2), four morphological (M1-M4) and two deformation dynamics (T1,T2) parameters extracted from the captured high speed images, linear discriminant analysis (LDA) successfully grouped pluripotent and differentiated cells separately. (E) The captured images are rich in information and are converted to a Cartesian coordinate system to extract a range of physical parameters. Substantial changes in physical properties of cells are observed upon differentiation, including cell morphology, size, deformability and length of time that cells and particles spend in the junction. Deformable pluripotent stem cells show time-dependent properties more in line with 500 centistokes (cSt) PDMS oil-in-water droplets and 1kPa agarose beads than stiffer differentiated cells which behave more like 1000 cSt PDMS oil. (Full definition of parameters in Supplementary Information) Scale bars: 20 μ m

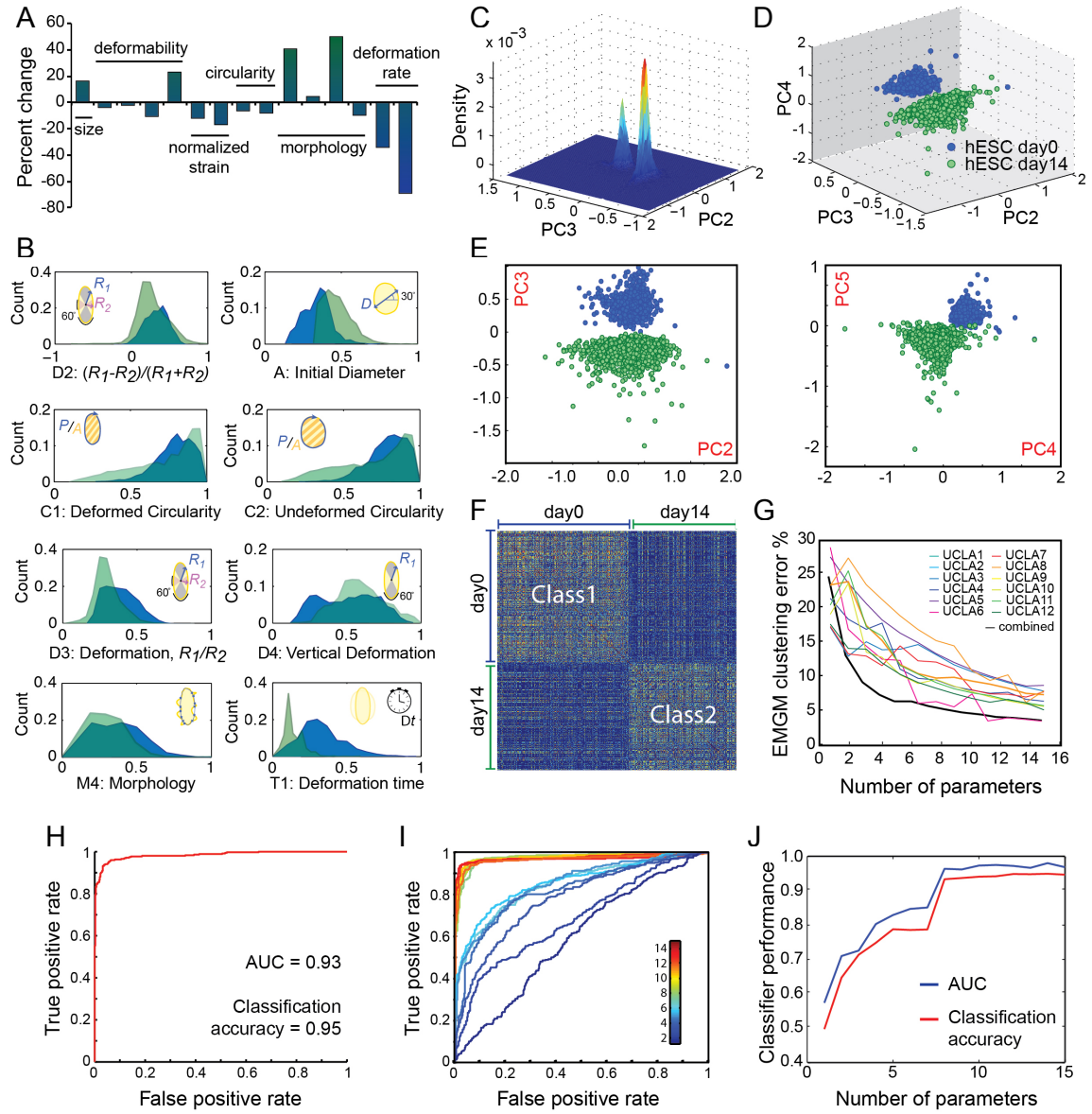


Figure 6. Multiparameter screening of mechanical and morphological properties can classify single cells accurately based on their pluripotency. (A) The percent change in median value of all 15 measured properties for all 12 hESC lines following 14 day differentiation (B) Histograms (normalized count) showing the variations within cell populations are depicted for several parameters showing overlap at the single-cell level for single properties (day0 in blue and day14

in green). (C) The Gaussian kernel density estimation of PC2 and PC3 of the data from all 12 cell lines at day0 and day14 show the existence of two distinct populations in the collapsed multidimensional space. (D,E,F) Labeling the data points as day0 (blue) and day14 (green) samples in PC space shows these distinct clusters correspond to the two cell states. Note larger variation is present within the day14 cluster compared to day0. (F) Similarity scores comparing the individual data points together shows the existence of two major blocks of highly similar data points, corresponding to day0 and day14 samples. The similarity scores within day0 samples (Class 1) are on average larger than day14 samples (Class 2), indicated by more dark red points. (G) Expectation-maximization clustering for individual cell lines and the pooled data shows a decrease in clustering accuracy when parameters were iteratively eliminated. (H) ROC graph showing the performance of a linear kernel SVM classifier with all 15 parameters. (I) Using RFE and removing parameters one by one, ROC curves for different numbers of parameters show a decline in classifier performance with smaller numbers of parameters. (J) AUC and classification accuracy increase with number of parameters, although reaching a plateau at ~ 9 parameters.

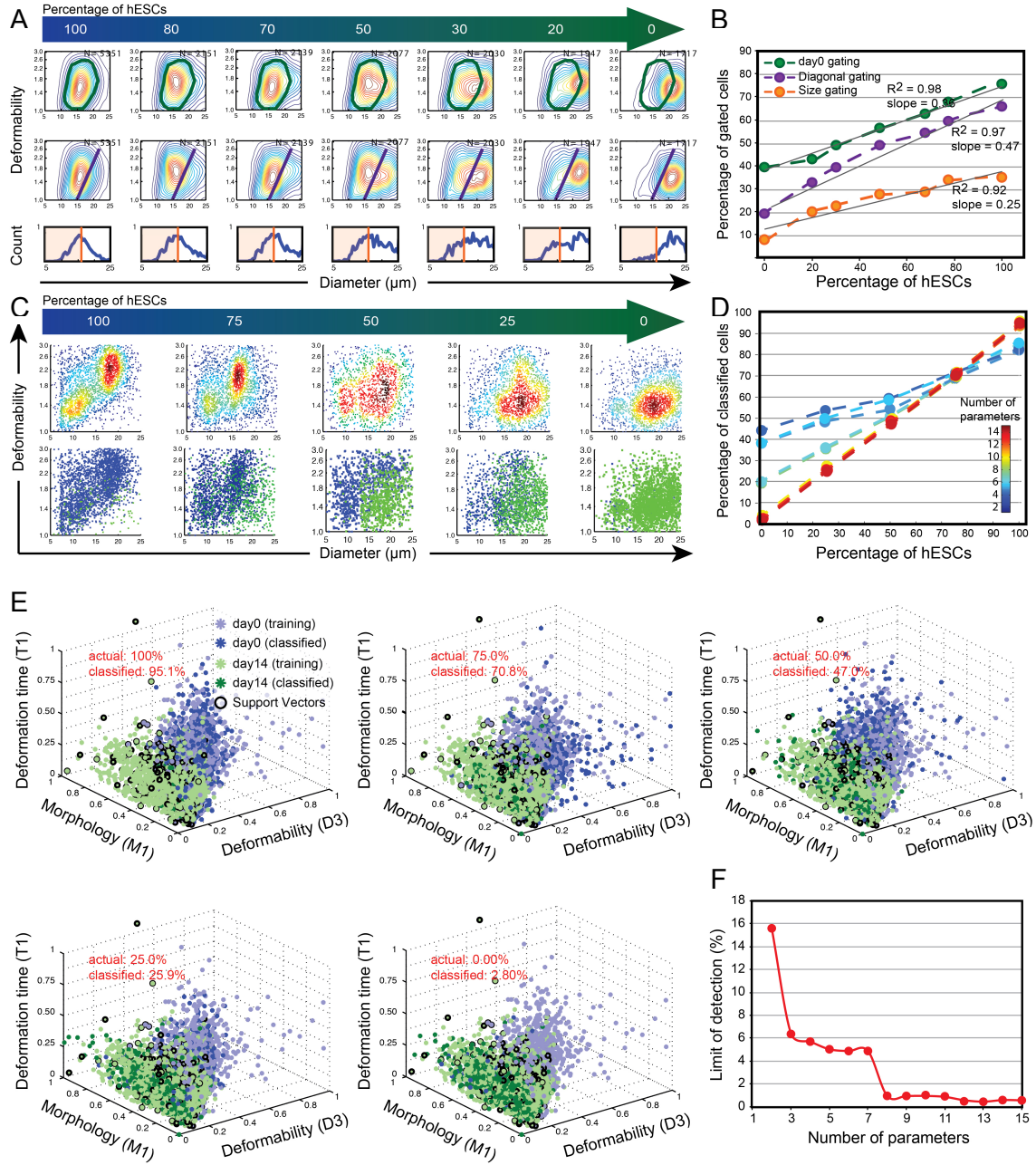


Figure 7. Impurities in mixed population samples can be detected using biophysical properties.

(A) Day0 and day14 samples spiked at different ratios were analyzed and three different gating methods were applied to characterize the spiking ratio: “*Diagonal gating*”, “*day0 gating*” and “*size gating*”. (B) Plot of percentage of gated cells versus percentage of spiked day0 cells. The slope of these curves can be interpreted as the sensitivity of prediction to variations in mixed

populations. Having a lower slope of the curve, e.g. in “*size gating*” leads to more errors caused by sample-sample variations and when deviating from a 1:1 spiking ratio. (C) Using all 15 parameters, spiked samples could be accurately classified as single cells day0 (blue) or day14 (green). (D) Increasing the number of physical parameters improves prediction of the two spiked sub-populations. (E) The individual cells acting as support vectors for spiked populations at different ratios and cells classified as day0 (dark blue) and day14 (dark green) are shown in the sub-space of 3 different parameters: Deformability parameter D3, Morphology parameter M1 and deformation dynamics parameter T1. The whole data set from all 12 cell lines for pure day0 (light blue) and day14 (light green) were used as training sets. (F) Increasing the number of parameters enables the distinction of lower impurities in mixed samples. The “*Limit of detection*” was calculated as the inverse of analytical sensitivity, where analytical sensitivity was defined as the slope of the curve normalized by the standard deviation of day0 classified cells between samples of the same cell type.

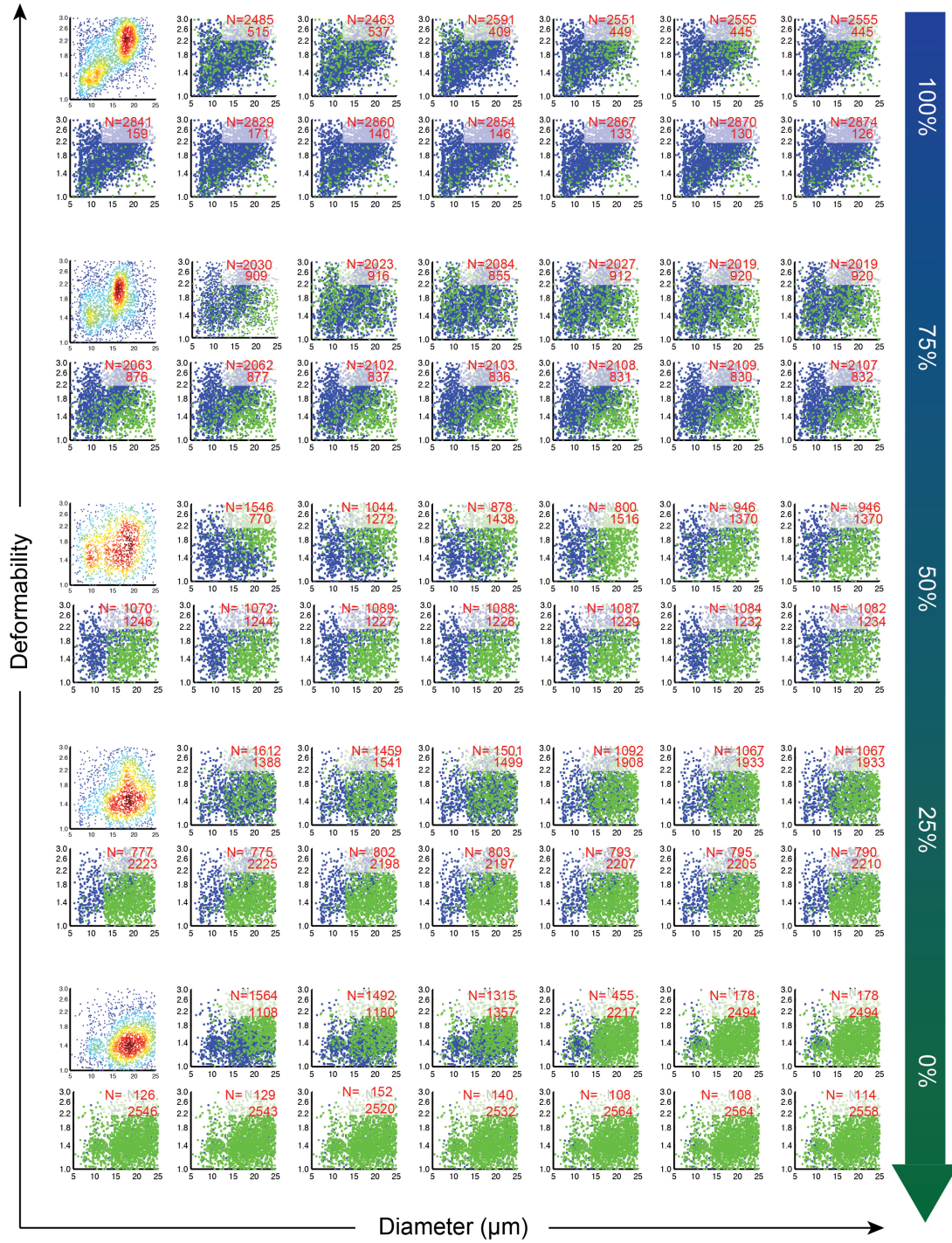


Figure 8. Spiked sample classification with SVM for increasing numbers of parameters. For each spiked sample (containing 100, 75, 50, 25 or 0 percent day0 cells) data points classified as day0

(blue) and day14 (green) are shown using 3 to 15 parameters. The data is depicted in the two dimensional space of deformability and cell diameter.

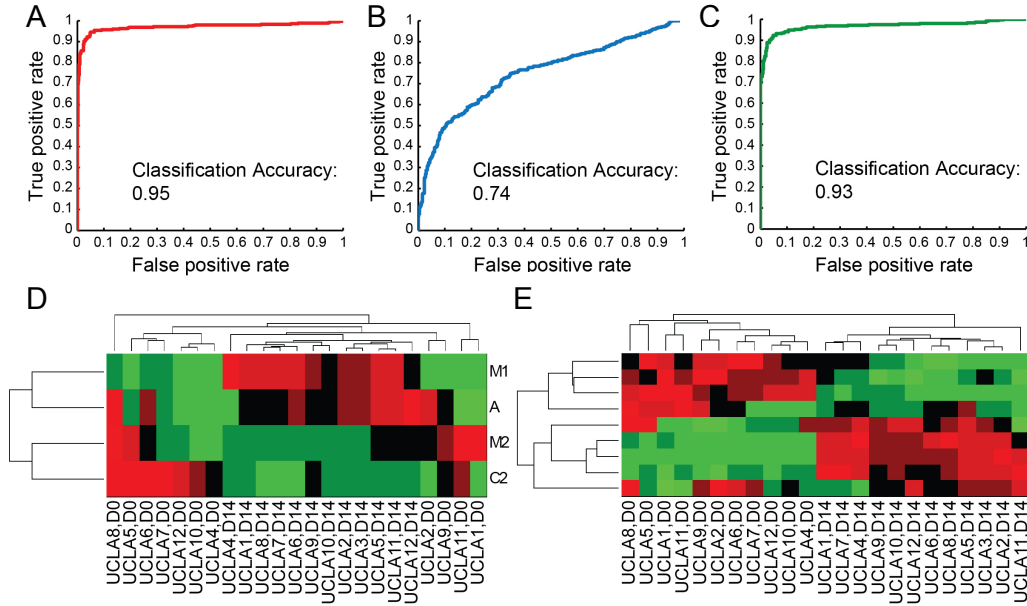


Figure 9. Dynamic mechanical properties of cells are critical for accurate classification. (A) ROC plot showing the performance of the SVM classifier using all 15 biophysical parameters. (B) Using only the morphology parameters captured before the junction, classification accuracy dropped substantially to 74%. (C) Only considering parameters captured at the junction (during cell deformation) we could classify cells based on their pluripotency with 93% accuracy. (D,E) Clustering of cell populations using only pre-junction (D) and in-junction (E) parameters respectively. Four day0 samples were misclassified when only pre-junction parameters were used.

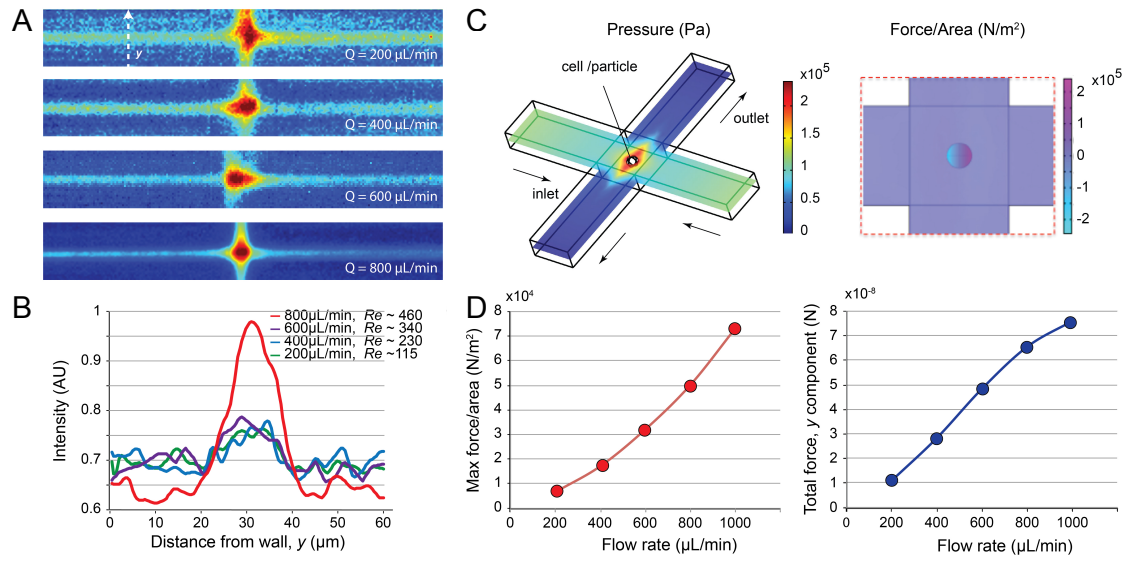


Figure 10. Applying uniform force on cells (A) Flow rate should be high enough to focus cells at a single lateral position in order to apply uniform force to cells of the same size. (B) Standard deviation plots showing the variations in lateral position of cells arriving at the junction and optimal operation at 800 mL/min. (C) Comsol simulations predict that the pressure on the cell is around 10^5 Pa at the extensional region when flow rate is $\sim 1000 \mu\text{L/min}$. (D) Maximum force/area in the channel and the total y component of force on cells in the junction increase with increasing operating flow rate.

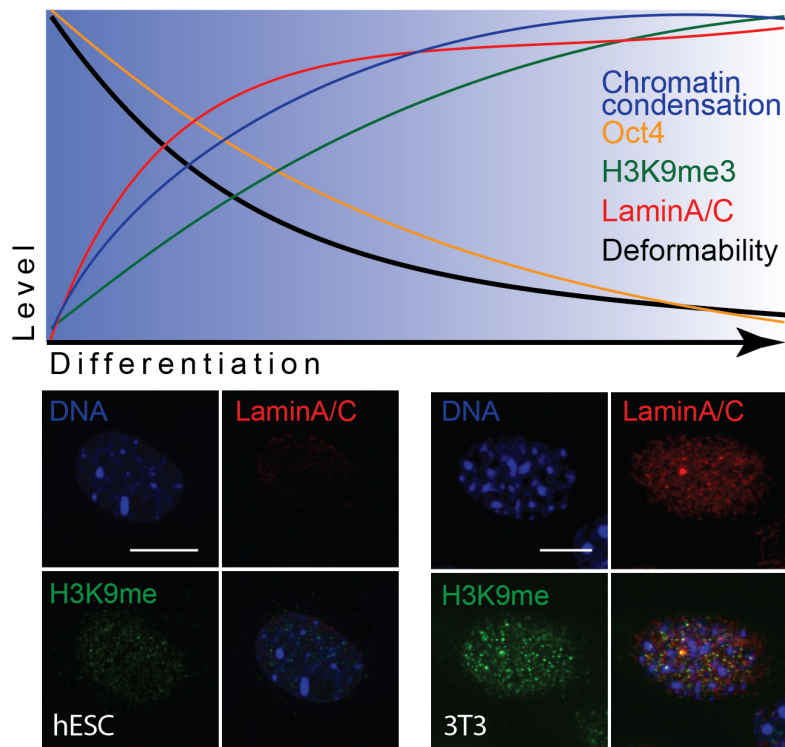


Figure 11. Structural, epigenetic, and biophysical changes occur concurrently upon differentiation. Expression of pluripotency markers including Oct4 decrease, while methylation of H3K9 (green) and the level of chromatin condensation (dsDNA in blue) increase. The level of Lamin A/C increases following differentiation. These changes are accompanied by a decrease in cell deformability. Scale bars: 5μm.

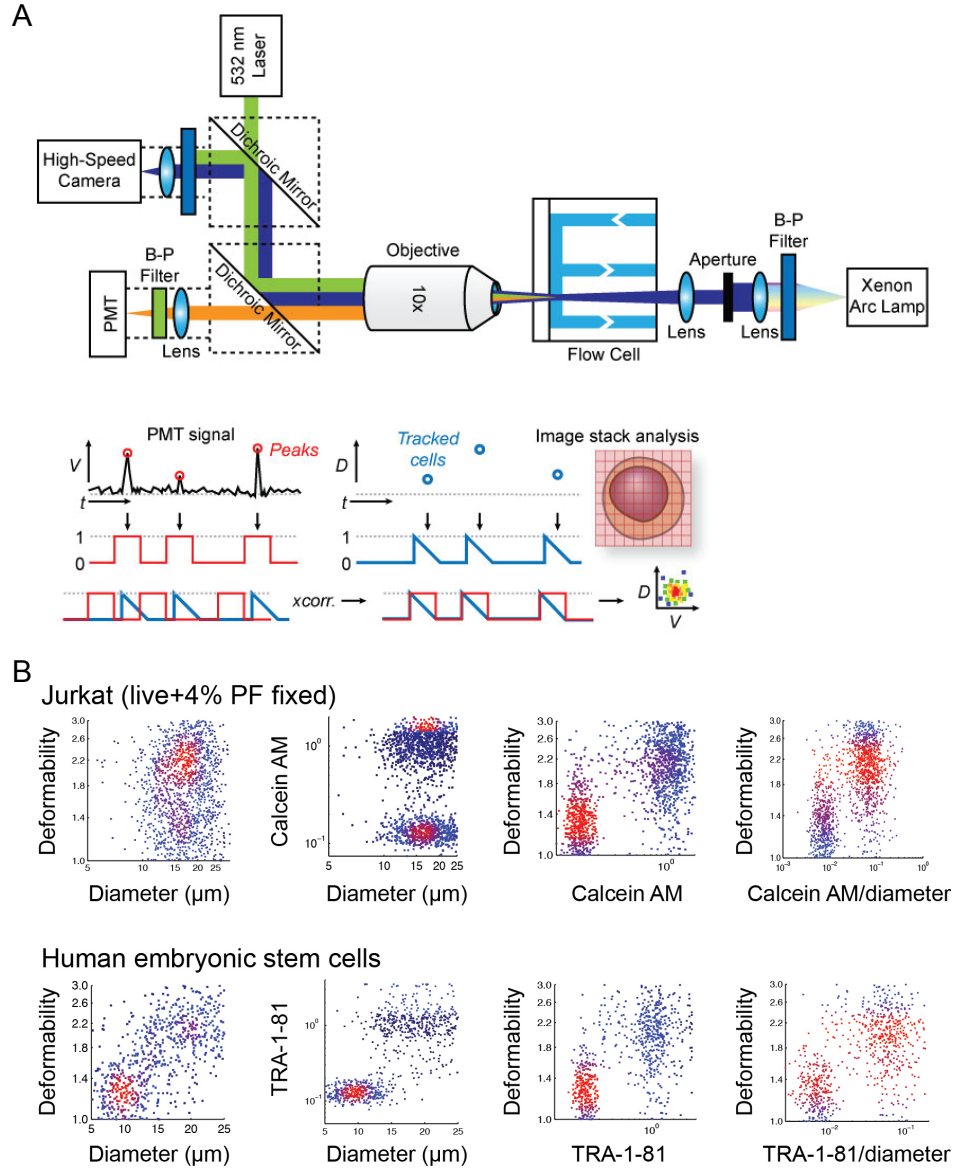


Figure 12. Simultaneous fluorescence and mechanical analysis confirms the correlation of TRA-1-81 expression and deformability at single cell level. (A) Optical setup for simultaneous assessment of cell mechanical and molecular analysis. (B) Live jurkat cells labeled with calcein AM and fixed unlabeled jurkat cells were mixed and analyzed by the system in a. Stiffer unlabeled fixed cells showed lower fluorescent signal and small deformability as expected (first row). Human embryonic stem cell culture containing mouse embryonic feeders (mEF) were

analyzed with this system. Two distinct populations were detected: larger more deformable stem cells and smaller stiffer mEFs. Labeling the sample with TRA-1-81 pluripotency marker confirmed that the population of large and deformable cells are in fact pluripotent at the single cell level.

	D1	D2	A	D3	D4	S1	C1	C2	S2	M1	M2	M3	M4	T1	T2
UCLA1,d0	0.02	0.03	0.14	0.88	0.04	0.75	0.02	0.04	0.5	0.06	0.04	0.05	0.04	0.01	0.06
UCLA2,d0	0	0.03	0.14	0.83	0.04	0.71	0.02	0.04	0.48	0.06	0.05	0.05	0.04	0.01	0.05
UCLA3,d0	0.01	0.03	0.14	0.87	0.04	0.75	0.02	0.04	0.51	0.06	0.03	0.05	0.03	0.01	0.06
UCLA4,d0	0	0.03	0.14	0.84	0.04	0.73	0.02	0.04	0.49	0.06	0.04	0.05	0.04	0	0.05
UCLA5,d0	0.01	0.03	0.14	0.85	0.04	0.73	0.02	0.04	0.49	0.06	0.04	0.05	0.04	0	0.05
UCLA6,d0	0.01	0.03	0.14	0.88	0.04	0.76	0.02	0.04	0.51	0.06	0.03	0.05	0.04	0.01	0.06
UCLA7,d0	0.01	0.03	0.14	0.87	0.04	0.75	0.02	0.04	0.51	0.06	0.03	0.05	0.04	0.01	0.06
UCLA8,d0	0.02	0.03	0.14	0.86	0.04	0.73	0.02	0.04	0.49	0.06	0.04	0.05	0.04	0.01	0.05
UCLA9,d0	0.01	0.03	0.14	0.9	0.03	0.78	0.02	0.04	0.48	0.06	0.04	0.05	0.04	0	0.05
UCLA10,d0	0.02	0.03	0.14	0.86	0.04	0.74	0.02	0.04	0.5	0.06	0.03	0.05	0.04	0.01	0.05
UCLA11,d0	0.01	0.03	0.14	0.86	0.04	0.74	0.02	0.04	0.49	0.06	0.04	0.05	0.04	0.02	0.04
UCLA12,d0	0.1	0.03	0.13	0.79	0.03	0.74	0.02	0.04	0.48	0.06	0.03	0.07	0.04	0.03	0.06
UCLA1,d14	0.11	0.03	0.14	0.77	0.03	0.72	0.02	0.04	0.47	0.06	0.04	0.06	0.04	0.02	0.06
UCLA2,d14	0.1	0.03	0.14	0.8	0.04	0.74	0.02	0.04	0.48	0.06	0.03	0.06	0.04	0.03	0.06
UCLA3,d14	0.11	0.03	0.13	0.76	0.03	0.71	0.02	0.04	0.47	0.06	0.03	0.06	0.04	0.02	0.05
UCLA4,d14	0.1	0.03	0.14	0.79	0.04	0.74	0.02	0.04	0.48	0.07	0.03	0.06	0.04	0.03	0.06
UCLA5,d14	0.1	0.03	0.14	0.81	0.03	0.74	0.02	0.04	0.48	0.06	0.03	0.06	0.04	0.03	0.06
UCLA6,d14	0.11	0.03	0.14	0.8	0.04	0.73	0.02	0.04	0.47	0.07	0.04	0.05	0.03	0.03	0.06
UCLA7,d14	0.09	0.03	0.15	0.83	0.04	0.77	0.02	0.04	0.48	0.06	0.04	0.06	0.04	0.03	0.06
UCLA8,d14	0.09	0.03	0.14	0.81	0.03	0.75	0.02	0.04	0.48	0.06	0.03	0.06	0.04	0.03	0.05
UCLA9,d14	0.12	0.03	0.13	0.75	0.03	0.7	0.02	0.04	0.46	0.06	0.03	0.06	0.03	0.02	0.05
UCLA10,d14	0.13	0.03	0.13	0.76	0.04	0.7	0.02	0.04	0.46	0.06	0.03	0.05	0.03	0.02	0.06
UCLA11,d14	0.11	0.03	0.13	0.77	0.03	0.71	0.02	0.04	0.47	0.07	0.03	0.06	0.04	0.02	0.05

Table 1. Linear discriminant analysis (LDA) coefficients for classifying 12 hESC lines before and after 2 weeks of differentiation. The 6 parameters with maximum average coefficients are deformability (D3), relative strain parameters (S1,S2) cell diameter (A), morphology (M1) and deformation time (T2)

	PC1	PC2	PC3	PC4	PC5	PC6	PC7	PC8	PC9	PC10	PC11	PC12	PC13	PC14	PC14
D1	0	0	0	0	0.02	0.03	0.01	0	1	0.03	0.04	0	0.01	0	0
D2	0	0	0	0	0	0	0	0.01	0.01	0.03	0.44	0.02	0.83	0.32	0.11
A	0.04	0.02	0.22	0.28	0.93	0.06	0.03	0.07	0.02	0	0.01	0	0.01	0	0
D3	0	0	0	0.01	0.02	0	0	0.01	0.04	0.06	0.88	0.1	0.45	0.05	0
D4	0.12	0.01	0.15	0.93	0.32	0.01	0.01	0.01	0	0	0	0	0	0	0
S1	0.17	0.01	0.94	0.23	0.16	0	0	0.01	0.01	0	0.01	0	0	0	0
C1	0	0	0	0	0	0	0	0	0.03	0.91	0.09	0.4	0.02	0	0.01
C2	0	0	0	0	0	0	0	0	0.01	0.41	0.04	0.91	0.06	0	0.01
S2	0	0	0	0	0	0	0	0	0	0.02	0.05	0.01	0.09	0.04	0.99
M1	0.46	0.88	0.1	0.03	0	0	0.01	0	0	0	0	0	0	0	0
M2	0	0.01	0.01	0.01	0.05	0.58	0.8	0.14	0.03	0	0	0	0	0	0
M3	0.87	0.47	0.16	0.08	0.04	0	0	0	0	0	0	0	0	0	0
M4	0	0	0.01	0.03	0.03	0.81	0.59	0.02	0.01	0	0	0	0	0	0
T1	0	0	0	0.02	0.08	0.09	0.1	0.99	0	0.01	0.01	0	0	0	0
T2	0	0	0	0	0	0	0	0	0	0.01	0.1	0.02	0.31	0.95	0.01

Table 2. PCA components show a strong dependence of the most important PCs, PC1, PC2 and PC3 on parameters S1, M1, M3, A and D4 (absolute values of coefficients are shown).

	D1	D2	A	D3	D4	S1	C1	C2	S2	M1	M2	M3	M4	T1	T2
D1	1.00	0.26	0.53	0.14	0.44	0.35	0.17	0.23	0.12	0.16	0.28	0.28	0.26	0.22	0.15
D2	0.26	1.00	0.27	0.86	0.44	0.73	0.04	0.01	0.41	0.19	0.08	0.62	0.04	0.39	0.40
A	0.53	0.27	1.00	0.13	0.49	0.64	0.29	0.31	0.04	0.38	0.45	0.24	0.31	0.15	0.18
D3	0.14	0.86	0.13	1.00	0.29	0.78	0.07	0.04	0.44	0.15	0.02	0.55	0.12	0.27	0.36
D4	0.44	0.44	0.49	0.29	1.00	0.44	0.16	0.19	0.26	0.13	0.21	0.74	0.34	0.17	0.25
S1	0.35	0.73	0.64	0.78	0.44	1.00	0.11	0.13	0.24	0.33	0.23	0.49	0.08	0.27	0.35
C1	0.17	0.04	0.29	0.07	0.16	0.11	1.00	0.62	0.15	0.31	0.27	0.06	0.11	0.08	0.05
C2	0.23	0.01	0.31	0.04	0.19	0.13	0.62	1.00	0.14	0.48	0.25	0.03	0.14	0.03	0.08
S2	0.12	0.41	0.04	0.44	0.26	0.24	0.15	0.14	1.00	0.06	0.10	0.40	0.10	0.01	0.08
M1	0.16	0.19	0.38	0.15	0.13	0.33	0.31	0.48	0.06	1.00	0.10	0.17	0.10	0.16	0.09
M2	0.28	0.08	0.45	0.02	0.21	0.23	0.27	0.25	0.10	0.10	1.00	0.05	0.31	0.09	0.06
M3	0.28	0.62	0.24	0.55	0.74	0.49	0.06	0.03	0.40	0.17	0.05	1.00	0.10	0.25	0.28
M4	0.26	0.04	0.31	0.12	0.34	0.08	0.11	0.14	0.10	0.10	0.31	0.10	1.00	0.06	0.06
T1	0.22	0.39	0.15	0.27	0.17	0.27	0.08	0.03	0.01	0.16	0.09	0.25	0.06	1.00	0.13
T2	0.15	0.40	0.18	0.36	0.25	0.35	0.05	0.08	0.08	0.09	0.06	0.28	0.06	0.13	1.00

Table 3. Correlation coefficient matrix (absolute coefficient values) shows some level of linear dependence between several parameters. The highest correlation was observed between parameters D2 and D3, which are both deformability measures at the junction as well as D3 and S1, which are deformability and normalized deformability measures at the junction. The least correlation is observed between S2 and T1.

Supplementary videos

SI video 1: Human embryonic stem cells (day0) deforming at the extensional flow region.

SI video 2: Fourteen-day differentiated human embryonic stem cells (day14) deforming at the extensional flow region.

SI video 3: A collection of cells deforming at the junction and their transformation from polar to Cartesian coordinate system. The white lines show the edges of the cells detected by the Matlab image processing script. The 15 parameters are extracted from the Cartesian maps as described in SI Fig.1.

SI video 4: Showing the polar to Cartesian coordinate system transformation of a sequence of images captured from one cell deforming in the device.

Chapter 3

The Role of Chromatin Structure in Cell Mechanical Stiffness:

Application in Drug Screening

As the largest and most rigid eukaryotic organelle, the cell nucleus is hypothesized to be a critical determinant of overall cell deformability. One study showed the nuclei of human embryonic stem cells (ESCs) became less deformable upon differentiation¹. ESCs are known to have more open euchromatin than differentiated cells, which has been associated with a reduction in nuclear viscosity and stiffness². Interestingly, chromatin and nuclear lamina, both being major determinants of nuclear mechanics, undergo extensive changes during differentiation. One of the major determinants, A-type lamins are not expressed in ESCs and are only present in differentiated cells. Additionally, several epigenetic modifications including global DNA hypermethylation and a decrease in acetylation of histones H3 and H4 lead to substantial chromatin reorganization during differentiation. Cellular and nuclear deformability associated with specific nuclear properties and chromatin organization could therefore be used as an indicator of cell pluripotency. Aberrant epigenetic regulation, causing undesirable gene silencing or expression, has also been observed frequently in cancer cells, and the level of chromatin condensation controlled by these epigenetic modifications is found to considerably alter the structural and physical properties of chromatin and the cell nucleus. In fact nuclear shape and structure is still one of the main tools for histological detection and classification of cancer³.

Chromatin and cellular processes. In eukaryotic cells, DNA is tightly packed in chromatin, a complex of mainly DNA and histone proteins. Chromatin is responsible for the spatial organization of genome and is classified as (i) regions associated with active gene expression and low condensation (open chromatin) located at the nuclear interior, euchromatin; and (ii) transcriptionally silent areas, heterochromatin, which are associated with high compaction and condensation (highly-packed, closed chromatin); usually located at the periphery of the nucleus or near the nucleolus ^{2,4}. Chemical modification of chromatin is one of the major mechanisms that regulate the transcriptional profile of a cell ⁵. These chemical modifications mainly include DNA methylation and the posttranslational modifications of histone such as acetylation, methylation and phosphorylation ⁶. The posttranslational modifications can directly alter the physical accessibility of DNA by changing chromatin structure, hence directly involved in cell transcriptional activation or silencing. As such modifications are essential in a variety of cellular processes, blocking them would result in inhibition of proper development. For example disruption of H3K9 (lysine 9 on histone 3) methylation or HDAC1 (histone deacetylase 1) results in embryo death ^{7,8}.

Chromatin reorganization through epigenetic modifications, referred to as heritable changes in the pattern of gene expression that are independent of primary nucleotide sequence ⁹ are associated with a variety of cellular processes and human conditions such as stem cell differentiation, cancer, aging and cardiovascular disease ¹⁰⁻¹². Stem cells undergo extensive modifications in chromatin organization during differentiation ¹³. For instance, hypoacetylation and H3K9 di- or tri-methylation of chromatin structure and high levels of DNA methylation is observed in stem cell differentiation along the neural lineage ¹⁴. Tumor progression is also often associated with changes in nuclear organization ¹⁵. For example, aberrant DNA

hypermethylation linked with silencing tumor suppressor genes has been observed in cancer^{16,17}. Changes in DNA methylation are shown to be associated with atherosclerotic vascular disease^{18,19}.

While chromatin organization is critical in regulating genetic processes, it has been suggested that it may also largely contribute to cellular and nuclear mechanics. Interestingly, studies have shown that modifications in the structure of chromatin could be a critical determinant of nuclear and cell overall mechanical properties²⁰. Global organization of chromatin seems to be a regulator of nuclear shape, size and stiffness, which could modulate several tissue and matrix developmental events including migration and cell-microenvironment interactions.

Chromatin structure and cell mechanobiology. Chromatin as one of the main determinants of nuclear organization could play a significant role in cell overall stiffness. Studies on endothelial cells have shown that the nucleus of these cells is about 9 times stiffer than the cytoplasm²¹. Micropipette aspiration of the isolated nuclei of articular chondrocytes have shown that the elasticity and viscosity of the nucleus is higher than the cytoplasm²². Similarly, it was found that the nucleus of neutrophils is about 10 times more elastic and viscous than the cytoplasm²³. Studies on spread and round endothelial cells have shown that while the elastic modulus of the cytoplasm is on the order of 500 Pa, the nuclear stiffness of these cells is on the order of 5000 Pa²⁴. Taken together, these studies suggest nucleus as the main contributor to cellular rheology, suggesting an important role for chromatin, which is the key determinant of nuclear organization. Isolated nuclei treated with ethylenediaminetetraacetic acid (EDTA), (a chelating agent that decondenses chromatin through binding divalent cations) showed significant expansion of nuclear envelope, increase in nuclear size and reduction in the stiffness of the

nucleus while imposing chromatin condensation through addition of divalent cations resulted in nuclear contraction and greater nuclear stiffness^{2,25} (23, 24).

As the largest eukaryotic organelle, the nucleus plays an important role in cell migration through its size and deformability. Given its determining role in nuclear size and stiffness²⁶, chromatin could facilitate necessary cellular organizations for cell migration. Recently, it was shown that the migration of melanocytes in a defined direction depends on global chromatin organization²⁷. During cell migration, coordinated structural changes between the cytoskeleton and chromatin is facilitated through a direct physical link between the chromatin and various cytoskeletal elements in the cytoplasm, including actin filaments²⁸, microtubules motor proteins²⁹ and intermediate filaments^{30,31}, established by the SUN domain and KASH domain proteins³²⁻³⁴. This coordination in structural changes between the chromatin and cytoskeleton could result in epigenetically regulated cell elongation and organization, which might affect the organization of the extracellular matrix (ECM). Therefore, in addition to the apparent role of chromatin structure in regulating the expression of genes encoding for proteins that are involved in the migration process, the direct structural and physical role of chromatin condensation could significantly contribute to cell migration patterns.

In addition to cell migration, nuclear stiffness could affect the cell-cell and cell-substrate interactions by influencing the outcome of forces applied to it. While forces applied to a stiff nucleus would stay focused, highly deformable nuclei would disperse the force into many directions, resulting in less significant downstream effects. Because these forces do not operate independently and are balanced within the tissue, these different effective forces could orchestrate downstream cellular events including cell survival, growth, differentiation, cell-cell communication and spatial organization of cells and ECM differently³⁵.

While chromatin structure can regulate tissue structural and mechanical properties through modifying critical cellular processes including cell migration, cell-microenvironment interactions and ECM organization, it could also act as a cellular mechanosensor, directly affecting transcriptional regulation in response to external mechanical stimuli. Mechanical stimuli in cell extracellular environment are transmitted by integrins and cadherins to cytoskeletal filament networks, which are further linked to subnuclear elements such as chromatin³⁴. Several studies confirm the existence of a physical link between extracellular integrins and subnuclear elements, which can act as transmitters of mechanical signal from cell surface to nucleus³⁶. Through this nuclear mechanotransduction, physical and mechanical cues at the cell surface can be translated into structural changes in chromatin. For example reorganization in actin, intermediate filaments, microtubules as well as nucleus is reported following the application of shear forces on cells by flow^{21,37-39}. Studies using atomic force microscopy (AFM) and micropipette aspiration on whole cells as well as isolated nuclei show that shear stress will change nuclear shape and stiffness^{40,41}. Through computational studies it is suggested that cells exposed to flow respond to external shear by aligning in the direction of flow to minimize the shear force on their nuclei⁴².

Through deforming the nucleus, these forces could result in altered DNA packing and structural changes in chromatin⁴³. Mechanically stretched rat cardiac myocytes were shown to transmit the mechanical signal to the chromatin, rearranging nuclear envelope associated chromatin via intermediate filaments⁴⁴. Recently, mechanostimulation of human fibroblasts with micron-scale grooves and ridges was found to result in transcript-level effects on mediators of chromatin remodeling such as HMGA1 and HMGB1⁴⁵. A recent study using differential scanning calorimetry suggests that ultrasound stimulation of fibroblasts can have a transient effect on chromatin organization⁴⁶. These changes in chromatin structure and organization could

further restrict or promote the accessibility of chromatin and genes to transcription factors resulting in alterations in gene transcription.

Here, we summarize the observed epigenetic modifications and alterations of cell and tissue physical properties associated with three important cellular processes and conditions: stem cell differentiation, cancer progression and cardiovascular disease.

Stem cell differentiation. Embryonic stem cells (ESCs) are a main focus of intensive research in regenerative medicine due to their capacity to self-renew indefinitely and to differentiate into cell lines of all three germ layers. It is established that crucial changes in gene expression profiles during the progression from ESCs to their differentiated progeny are accompanied by multiple epigenetic rearrangements^{47,48}. Along with expression of specific pluripotency factors, stem cells possess a signature epigenetic landscape. Studies suggest that chromatin organization changes significantly during differentiation, which is accompanied by alteration in transcriptional activity. While the chromatin of pluripotent cells is suggested to possess an “open” conformation, responsible for genome plasticity and cell self-renewal state^{12,49-51}, differentiation results in a change in chromatin organization and a switch to “closed” chromatin conformation. Studies on ESCs reported an increase in the number of heterochromatin foci during their differentiation to neuronal progenitor cells (NPCs)⁵². Along these changes in chromatin organization, several chemical modifications in DNA and histone are reported during differentiation. The genome of differentiated somatic cells is suggested to be globally hypermethylated compared to ESCs⁵³. Several heterochromatin marks increase during mouse ESC differentiation, including histone H3 lysine 9 trimethylation (H3K9me3), histone H3 lysine 27 methylation and dimethylation (H3K27me and H3K27me2), histone H4 lysine 20 di- and trimethylation (H4K20me2 and H4K20me3)⁵⁴. In ESCs many non-transcribed genes are associated

with a “bivalent” chromatin structure, enriched both in active chromatin marks such as high levels of H3K4me2 and H3K4me3 and repressive marks such as H3K27me3. Differentiated cells, however, while retaining repressive chromatin mark, H3K27me3 do not show the active chromatin mark^{55,56}.

Differentiation is also associated with a global decrease in histones H3 and H4 acetylation^{12,57}. Along the same line, treatment of ESCs with a common histone deacetylase (HDAC) inhibitor, trichostatin A resulted in inhibition of differentiation⁵⁷. Moreover, during differentiation promoters of critical pluripotency transcription factors such as OCT4 are methylated^{58,59}. As DNA methylation is suggested to inhibit transcription, methylation at the promoter of these genes is believed to be responsible for keeping them silent in differentiated cells^{60,61}. Additionally, lamin A/C proteins, which are not expressed in stem cells, appear as they differentiate¹⁰. These changes in chromatin arrangement are critical for transcriptional reprogramming during stem cell differentiation.

Nuclear and cellular mechanical stiffness also changes significantly during differentiation. Atomic force microscopy (AFM) and micropipette aspiration studies have reported lower stiffness for ESCs compared to differentiated cells. Studies on both mouse and human ESCs suggest that high deformability of ESCs could be an indicator of their self-renewal state^{2,62}. While both nuclear lamina and chromatin contribute to nuclear stiffness, lamina is shown to be mainly responsible for elastic behavior of the cells and chromatin is suggested to mostly “flow” plastically under load². Microrheology experiments on ESCs with condensed chromatin have shown that these cells are much less pliable than normal cells². As one of the major determinants of nuclear shape and deformability has been suggested to be the level of chromatin condensation, epigenetic modifications could be at least one of the reasons behind alterations in cell mechanics

during stem cell differentiation. Chromatin reorganization during differentiation could therefore significantly contribute to changes in nuclear stiffness. As discussed before, these alterations in nuclear stiffness could further result in changes in the patterns of cell migration and ECM organization, which still need to be investigated.

In addition to the effect of epigenetic modifications and chromatin reorganization on cell deformability alterations, the interaction between stem cell mechanobiology and epigenetics could be in fact responsible for lineage-specific differentiation through mechanotransduction. Epigenetic mechanisms are believed to regulate specific phenotypes in response to environmental cues². The mechanical signals from cell microenvironment such as substrate stiffness are found to play a key role in stem cell fate⁶³. Many recent studies have shed light on the significant influence of the extracellular matrix (ECM) on stem cell fate, partly caused by mechanical signals transmitted from the ECM to the cells^{63,64}. Extracellular physical and mechanical cues could be a means for alterations in the patterns of chromatin condensation. Regulation of nuclear shape by the cytoskeleton properties has already been observed in various processes including the dependence of granulocytes nuclei lobulation on microtubules⁶⁵ or the changes in nuclear shape of the chondrocytes caused by mechanical forces or cellular adhesion geometry through actin filaments^{28,66}. Chromatin reorganization alters regions available for transcription, which would result in modified gene expression patterns. Therefore, alterations in chromatin organization could be an upstream effect of external mechanical cues resulting in downstream effects including the regulation of specific gene expression and lineage-specific differentiation.

Epigenetic mechanisms are believed to be a means for cells to respond to the environment, which might result in the development of abnormal phenotypes under undesirable conditions⁶⁷.

Since the extensive modifications in chromatin organization have been observed during differentiation, the effect of environmental factors interfering with normal epigenetic processes could also result in differentiation deficiencies. Therefore, it would be interesting to explore the effect of epigenetic abnormalities on the potential of ESCs to differentiate into all three known germ layers.

Additionally, the cellular and molecular processes by which the mechanical signals could be translated into chromatin reorganization and stem cell fate are not fully understood. Evidence suggests the regulation of stem cell response to external mechanical stimuli through RhoA pathway⁶⁸. Manipulation of RhoA and its downstream effector, Rho kinase has been shown to affect the fate of mesenchymal stem cells⁶⁹. However, the detailed mechanism of the role of these signaling pathways in the regulation of self-renewal and differentiation of stem cells is not known. Since the self-renewal property of stem cells are associated with a signature chromatin state, it is interesting to understand whether the modifications in Rho/ROCK signaling pathways regulated by mechanical stimuli are translated into differentiation commitments through modifications in epigenetic properties of DNA and chromatin.

Cancer progression. Aberrant epigenetic regulation causing undesirable gene silencing has been observed frequently in cancer cells. DNA methylation aberrations are one of the fundamental epigenetic abnormalities involved in cancer development⁷⁰. Disruption of DNMT1 gene resulting in hypomethylation of DNA is reported to induce tumor formation in mice⁷¹⁻⁷³. Aberrant DNA methylation pattern as somatic mutations in DNMT3A was recently reported in acute myeloid leukemia⁷⁴. While loss of DNA methylation in cancer is detected globally throughout the genome, specific promoter regions have been characterized by hypo and hyper methylation patterns⁷⁵. While hypomethylation can account for aberrant expression of oncogenes

⁷⁶⁻⁷⁸, and also lead to loss of imprinting and induction of growth promoting genes expression ^{79,80}, such as IGF2⁸¹; hypermethylation at specific promoters results in silencing tumor suppressor genes such as CDKN2A, MLH1, MGMT or BRCA1^{75,82-85}.

Global histone modifications including H4K20me3 and H4K16Ac reduction are another hallmark of cancer. H3K16 acetylation loss and modifications of H4K20me3 and H3K27me3 have been also associated with cancer prognosis⁸⁶⁻⁸⁸. Alterations in the expression or activity of chromatin modifying enzymes have also been observed in several types of cancer and are in fact suggested to cause the global alterations in histone modification. For example histone deacetylases (HDAC1, HDAC2 and HDAC6) are overexpressed in tumors⁸⁹. Abnormalities in the expression of histone methyltransferases (HMTs) and histone demethylases (HDMs) are also associated with cancer⁹⁰. Overexpression of EZH2, a common HMT specific to H3K27, is reported in several tumors⁹¹. These alterations in epigenetic modifications result in aberrations in the level of chromatin condensation, which could considerably modify the structural and physical properties of chromatin and stiffness of nucleus. Several studies confirm a considerable difference in cancer cell mechanical properties compared to normal cells. Characterization of normal and cancerous human bladder epithelial cells using atomic force microscopy have showed an order of magnitude lower stiffness in cancer cells compared to normal ones ⁹². Human breast cancer (adenocarcinoma) cells (MCF7) also reported to be more deformable than non-malignant human mammary epithelial cells (MCF10)⁹³. Human myeloid cells (HL60) are shown to be six times stiffer than human neutrophils ⁹⁴. However, it is not known if chromatin reorganization is a main reason for the changes in cell stiffness in these conditions.

Nuclear stiffness changes could further play a crucial role in cell response to its environment and regulation of tumor cell migration and aberrant tissue reorganization. For

example, since cell deformability can facilitate passing through pulmonary circulation it is suggested to affect tumor cell metastasis⁹⁵. Studies have also reported an association between cell deformability and transformation of cell phenotype into tumorigenic metastatic state^{95,96}.

Tumor tissue is characterized with a modified extracellular matrix (ECM) composed of a network of glycoproteins and collagens, which modulate cancer cell adhesion and proliferation. During tumor development, ECM remodeling and stiffening initiate integrin clustering and actin remodeling, which enhance tumor cell growth and survival and confer tumor drug resistance^{97,98}. Production of extracellular elements, growth factors and cytokines by the tumor cells changes the local microenvironment of the cells, which modifies their proliferative and invasive behaviors. Therefore, the interaction between cancer cells and their environment, regulated by cell's physical and mechanical properties, can play a significant role in their migrational and invasional behavior. Manipulation of ECM organization and the interaction between tumor cells and their environment through chromatin reorganization could lead to therapeutic targets. Since epigenetic modifications appear to be reversible, epigenetic cancer therapeutics have received major interest recently. However, in the studies related to cancer epigenetics, the only role assumed for epigenetics processes has been their function as a regulator of tumor suppressor gene expression. For instance inhibition of DNA methylation, although not fully understood, is suggested to cause the trapping of DNA methyltransferases (DNMTs), which would result in expression of tumor suppressor genes that initiate cell differentiation and cancer cell death^{99,100}. However, the long-term effect of DNMT inhibition has not been investigated. Histone deacetylases (HDACs) are also found to regulate the induction of tumor cell death and inhibition of cell cycle progression⁸⁹.

Results

We previously did not observe any significant change in cell deformability upon treatment

of HeLa cells with cytoskeletal modifying drugs including Laranculin A, to disrupt actin polymerization and nocodazole to inhibit microtubules¹⁰¹. Here, we studied the effect of nuclear lamins and chromatin structure on our deformability measure. While all lamin knockout mouse embryonic fibroblasts showed a slightly softer profile compared to the wildtype cells, we detected more change in lamin B1 knockout cells compared to lamin A knockouts (Fig. 1).

Next, to study the effect of chromatin structure on cell deformability we treated 3T3 fibroblasts and Jurkat acute T-cell leukemia cells with several chromatin reorganizing drugs (Fig. 2). Hoechst 33258 dsDNA staining was used to visualize nuclear reorganization after treatment with chromatin modifying drugs or during human embryonic stem cell differentiation (Fig. 3A). The number of heterochromatin foci was used as an indicator of chromatin condensation level. We quantified the level of chromatin condensation by evaluating the number of heterochromatin foci in at least 20 cells per sample. We found that deformability is inversely correlated with the level of chromatin condensation (Fig. 3B). Stem cells and 3T3 cells that were treated with histone deacetylation (HDAC) inhibitor and DNA methylation (DNMT) inhibitors seemed to have a less condensed chromatin. These cells were significantly more deformable compared to untreated 3T3s. Fibroblasts treated with H3K9 methylation inhibitor, on the other hand were less deformable and had a more condensed chromatin. We also did not detect any significant difference in the deformability of DNMT triple knockout mouse embryonic stem cells compared to wildtype cells (Fig. 4).

Next, using multiparameter analysis described in chapter 2, we performed unsupervised clustering based on median parameter values for mouse fibroblasts treated with different drugs as well as lamin knockout cells. Linear Discriminant Analysis (LDA) successfully grouped the cells based on the nature of the treatment, either cytoskeletal or nuclear (Fig. 5).

Discussion

Epigenetic modifications are involved in various cellular processes and conditions. Interestingly, in these processes changes in cell mechanical and physical properties are reported, which are critical for the initiation and development of the specific process or condition. As chromatin structure and function are correlated, alterations of its structure resulting in changes in cell mechanics could be associated with alterations in cell function. Uncovering the detailed relation between the two could be beneficial in better controlling gene regulation by external mechanical signals in applications like stem cell differentiation. More interestingly, characterizing cells based on their mechanical properties as an indicator of their epigenetic properties could be used in applications like early diagnostic of disease.

Alterations in chromatin organization could be an upstream effect of external mechanical cues resulting in downstream effects including the regulation of specific gene expression and lineage-specific differentiation. An interesting study to understand this possible interaction would be through investigating the dynamics of chromatin remodeling during stem cell differentiation on substrates with different elastic moduli. Understanding the effect of extracellular mechanical signals on chromatin reorganization could be highly beneficial in applications such as controlling stem cell differentiation lineage. Aberrations in cellular shape and stiffness can be an early indicator of abnormal cellular function in a variety of physiological and pathological situations. Cell mechanics, could therefore be used as a screening tool for a number of cellular events. For instance, it is interesting to know whether the possible epigenetic abnormalities in stem cells resulting in their deficient pluripotency could be revealed through their mechanical properties. Future methods that can bring both high resolutions and high-throughput to the cell mechanics measurements could also give rise to earlier or easier cancer diagnostic approaches.

Identifying the extent to which nuclear structural changes underpin biophysical measurements can provide a molecular basis for using DC as a label-free diagnostic, especially in classifying disease states, such as cancer, that can be linked to abnormal chromatin structure. Importantly, we believe that there is a high correlation between chromatin structure and our deformability measure. The high information content, flexibility and throughput of this approach indicates the potential of multiparameter DC to serve as a general label-free screening tool for cell state. This could be useful for a variety of applications including cancer diagnosis, cell pluripotency characterization and drug screening.

Materials and Methods

We treated NIH-3T3 fibroblasts with several cytoskeletal drugs (to inhibit microtubules inhibitor with nocodazole (0.001–10 μ M), inhibit nonmuscle myosin II with blebbistatin (5 μ M), and disrupt actin polymerization with Latrunculin A (0.001–10 μ M) and modify Keratin network architecture by sphingosylphosphorylcholine (SPC) (0.1–10 μ M) for two hours and chromatin modifying drugs (to inhibit H3K9 methylation with Chaetocin, (5 μ M), inhibit histone deacetylation with Trichostatin A (TSA), (2 μ M) and inhibit DNA methylation with 5'-Deoxy-5'-(methylthio)adenosine (MTA), (5 μ M) and 5-Azacytidine (5Aza), (5 μ M) for 48 hours). Hoechst 33258 dsDNA staining was used to visualize nuclear reorganization after treatment with chromatin modifying drugs or during differentiation (Fig.2A). The number of heterochromatin foci was used as an indicator of chromatin condensation level.

Bibliography

1. Pajerowski, J. D., Dahl, K. N., Zhong, F. L., Sammak, P. J. & Discher, D. E. Physical plasticity of the nucleus in stem cell differentiation. *Proc. Natl. Acad. Sci.* **104**, 15619–15624 (2007).
2. Dahl, K. N., Ribeiro, A. J. S. & Lammerding, J. Nuclear shape, mechanics, and mechanotransduction. *Circ. Res.* **102**, 1307–1318 (2008).
3. Zwerger, M., Ho, C. Y. & Lammerding, J. *Nuclear mechanics in disease. Annu. Rev. Biomed. Eng.* **13**, 397–428 (2011).
4. Ruthenburg AJ, Li H, Patel DJ, & Allis CD (2007) Multivalent engagement of chromatin modifications by linked binding modules. *Nature reviews. Molecular cell biology* 8(12):983-994.
5. Turner BM (2002) Cellular memory and the histone code. *Cell* 111(3):285-291.
6. Amor DJ & Halliday J (2008) A review of known imprinting syndromes and their association with assisted reproduction technologies. *Hum Reprod* 23(12):2826-2834.
7. Lagger G, *et al.* (2002) Essential function of histone deacetylase 1 in proliferation control and CDK inhibitor repression. *The EMBO journal* 21(11):2672-2681.
8. Tachibana M, *et al.* (2002) G9a histone methyltransferase plays a dominant role in euchromatic histone H3 lysine 9 methylation and is essential for early embryogenesis. *Genes & development* 16(14):1779-1791.
9. Russo JJ, *et al.* (1996) Nucleotide sequence of the Kaposi sarcoma-associated herpesvirus (HHV8). *Proc Natl Acad Sci U S A* 93(25):14862-14867.
10. Constantinescu D, Gray HL, Sammak PJ, Schatten GP, & Csoka AB (2006) Lamin A/C expression is a marker of mouse and human embryonic stem cell differentiation. *Stem Cells* 24(1):177-185.
11. Park SH, Kook MC, Kim EY, Park S, & Lim JH (2004) Ultrastructure of human embryonic stem cells and spontaneous and retinoic acid-induced differentiating cells. *Ultrastruct Pathol* 28(4):229-238.
12. Meshorer E, *et al.* (2006) Hyperdynamic plasticity of chromatin proteins in pluripotent embryonic stem cells. *Developmental cell* 10(1):105-116.
13. Wu H & Sun YE (2006) Epigenetic regulation of stem cell differentiation. *Pediatric research* 59(4 Pt 2):21R-25R.

14. Ballas N, Grunseich C, Lu DD, Speh JC, & Mandel G (2005) REST and its corepressors mediate plasticity of neuronal gene chromatin throughout neurogenesis. *Cell* 121(4):645-657.
15. Zink D, Fischer AH, & Nickerson JA (2004) Nuclear structure in cancer cells. *Nature reviews. Cancer* 4(9):677-687.
16. Gao XN, *et al.* (MicroRNA-193a represses c-kit expression and functions as a methylation-silenced tumor suppressor in acute myeloid leukemia. *Oncogene* 30(31):3416-3428.
17. Toyota M, *et al.* (2001) Methylation profiling in acute myeloid leukemia. *Blood* 97(9):2823-2829.
18. Dong C, Yoon W, & Goldschmidt-Clermont PJ (2002) DNA methylation and atherosclerosis. *J Nutr* 132(8 Suppl):2406S-2409S.
19. Hiltunen MO & Yla-Herttuala S (2003) DNA methylation, smooth muscle cells, and atherogenesis. *Arterioscler Thromb Vasc Biol* 23(10):1750-1753.
20. Rowat AC, Lammerding J, Herrmann H, & Aebi U (2008) Towards an integrated understanding of the structure and mechanics of the cell nucleus. *Bioessays* 30(3):226-236.
21. Maniotis AJ, Chen CS, & Ingber DE (1997) Demonstration of mechanical connections between integrins, cytoskeletal filaments, and nucleoplasm that stabilize nuclear structure. *Proceedings of the National Academy of Sciences of the United States of America* 94(3):849-854.
22. Guilak F, Tedrow JR, & Burgkart R (2000) Viscoelastic properties of the cell nucleus. *Biochemical and biophysical research communications* 269(3):781-786.
23. Dong C, Skalak R, & Sung KL (1991) Cytoplasmic rheology of passive neutrophils. *Biorheology* 28(6):557-567.
24. Caille N, Thoumine O, Tardy Y, & Meister JJ (2002) Contribution of the nucleus to the mechanical properties of endothelial cells. *Journal of biomechanics* 35(2):177-187.
25. Dahl KN, Engler AJ, Pajerowski JD, & Discher DE (2005) Power-law rheology of isolated nuclei with deformation mapping of nuclear substructures. *Biophysical journal* 89(4):2855-2864.
26. Dahl KN, Kahn SM, Wilson KL, & Discher DE (2004) The nuclear envelope lamina network has elasticity and a compressibility limit suggestive of a molecular shock absorber. *Journal of cell science* 117(Pt 20):4779-4786.
27. Gerlitz G, *et al.* (2007) Migration cues induce chromatin alterations. *Traffic* 8(11):1521-1529.

28. Starr DA & Han M (2002) Role of ANC-1 in tethering nuclei to the actin cytoskeleton. *Science* 298(5592):406-409.
29. Fan J & Beck KA (2004) A role for the spectrin superfamily member Syne-1 and kinesin II in cytokinesis. *Journal of cell science* 117(Pt 4):619-629.
30. Homan SM, Martinez R, Benware A, & LaFlamme SE (2002) Regulation of the association of alpha 6 beta 4 with vimentin intermediate filaments in endothelial cells. *Experimental cell research* 281(1):107-114.
31. Gumbiner BM (2005) Regulation of cadherin-mediated adhesion in morphogenesis. *Nature reviews. Molecular cell biology* 6(8):622-634.
32. Haque F, *et al.* (2006) SUN1 interacts with nuclear lamin A and cytoplasmic nesprins to provide a physical connection between the nuclear lamina and the cytoskeleton. *Molecular and cellular biology* 26(10):3738-3751.
33. Worman HJ & Gundersen GG (2006) Here come the SUNs: a nucleocytoplasmic missing link. *Trends in cell biology* 16(2):67-69.
34. Wang N, Tytell JD, & Ingber DE (2009) Mechanotransduction at a distance: mechanically coupling the extracellular matrix with the nucleus. *Nature reviews. Molecular cell biology* 10(1):75-82.
35. Jaalouk DE & Lammerding J (2009) Mechanotransduction gone awry. *Nature reviews. Molecular cell biology* 10(1):63-73.
36. Oberhauser AF, Marszalek PE, Erickson HP, & Fernandez JM (1998) The molecular elasticity of the extracellular matrix protein tenascin. *Nature* 393(6681):181-185.
37. Helmke BP, Rosen AB, & Davies PF (2003) Mapping mechanical strain of an endogenous cytoskeletal network in living endothelial cells. *Biophysical journal* 84(4):2691-2699.
38. Helmke BP & Davies PF (2002) The cytoskeleton under external fluid mechanical forces: hemodynamic forces acting on the endothelium. *Annals of biomedical engineering* 30(3):284-296.
39. Kumar S, *et al.* (2006) Viscoelastic retraction of single living stress fibers and its impact on cell shape, cytoskeletal organization, and extracellular matrix mechanics. *Biophysical journal* 90(10):3762-3773.
40. Ochalek T, Nordt FJ, Tullberg K, & Burger MM (1988) Correlation between cell deformability and metastatic potential in B16-F1 melanoma cell variants. *Cancer research* 48(18):5124-5128.
41. Yao W, *et al.* (2003) Wild type p53 gene causes reorganization of cytoskeleton and, therefore, the impaired deformability and difficult migration of murine erythroleukemia cells. *Cell motility and the cytoskeleton* 56(1):1-12.

42. Igawa S, *et al.* (2004) Nitric oxide generated by iNOS reduces deformability of Lewis lung carcinoma cells. *Cancer science* 95(4):342-347.
43. Maniotis AJ, Bojanowski K, & Ingber DE (1997) Mechanical continuity and reversible chromosome disassembly within intact genomes removed from living cells. *Journal of cellular biochemistry* 65(1):114-130.
44. Bloom S, Lockard VG, & Bloom M (1996) Intermediate filament-mediated stretch-induced changes in chromatin: a hypothesis for growth initiation in cardiac myocytes. *Journal of molecular and cellular cardiology* 28(10):2123-2127.
45. McNamara LE, *et al.* (2012) The role of microtopography in cellular mechanotransduction. *Biomaterials* 33(10):2835-2847.
46. Noriega S, Budhiraja G, & Subramanian A (2012) Remodeling of chromatin under low intensity diffuse ultrasound. *The international journal of biochemistry & cell biology* 44(8):1331-1336.
47. Hattori N & Shiota K (2008) Epigenetics: the study of embryonic stem cells by restriction landmark genomic scanning. *FEBS J* 275(8):1624-1630.
48. Mattout A & Meshorer E (2010) Chromatin plasticity and genome organization in pluripotent embryonic stem cells. *Current opinion in cell biology* 22(3):334-341.
49. Meshorer E & Misteli T (2006) Chromatin in pluripotent embryonic stem cells and differentiation. *Nature reviews. Molecular cell biology* 7(7):540-546.
50. Jorgensen HF, *et al.* (2007) The impact of chromatin modifiers on the timing of locus replication in mouse embryonic stem cells. *Genome biology* 8(8):R169.
51. Bhattacharya D, Talwar S, Mazumder A, & Shivashankar GV (2009) Spatio-temporal plasticity in chromatin organization in mouse cell differentiation and during Drosophila embryogenesis. *Biophysical journal* 96(9):3832-3839.
52. Efroni S, *et al.* (2008) Global transcription in pluripotent embryonic stem cells. *Cell stem cell* 2(5):437-447.
53. Bibikova M, *et al.* (2006) Human embryonic stem cells have a unique epigenetic signature. *Genome research* 16(9):1075-1083.
54. Martens JH, *et al.* (2005) The profile of repeat-associated histone lysine methylation states in the mouse epigenome. *The EMBO journal* 24(4):800-812.
55. Azuara V, *et al.* (2006) Chromatin signatures of pluripotent cell lines. *Nature cell biology* 8(5):532-538.
56. Bernstein BE, *et al.* (2006) A bivalent chromatin structure marks key developmental genes in embryonic stem cells. *Cell* 125(2):315-326.
57. Lee JH, Hart SR, & Skalnik DG (2004) Histone deacetylase activity is required for embryonic stem cell differentiation. *Genesis* 38(1):32-38.

58. Ben-Shushan E, Pikarsky E, Klar A, & Bergman Y (1993) Extinction of Oct-3/4 gene expression in embryonal carcinoma x fibroblast somatic cell hybrids is accompanied by changes in the methylation status, chromatin structure, and transcriptional activity of the Oct-3/4 upstream region. *Molecular and cellular biology* 13(2):891-901.
59. Deb-Rinker P, Ly D, Jezierski A, Sikorska M, & Walker PR (2005) Sequential DNA methylation of the Nanog and Oct-4 upstream regions in human NT2 cells during neuronal differentiation. *The Journal of biological chemistry* 280(8):6257-6260.
60. Spivakov M & Fisher AG (2007) Epigenetic signatures of stem-cell identity. *Nature reviews. Genetics* 8(4):263-271.
61. Farthing CR, *et al.* (2008) Global mapping of DNA methylation in mouse promoters reveals epigenetic reprogramming of pluripotency genes. *PLoS genetics* 4(6):e1000116.
62. Chowdhury F, *et al.* (2010) Material properties of the cell dictate stress-induced spreading and differentiation in embryonic stem cells. *Nature materials* 9(1):82-88.
63. Engler AJ, Sen S, Sweeney HL, & Discher DE (2006) Matrix elasticity directs stem cell lineage specification. *Cell* 126(4):677-689.
64. Zajac AL & Discher DE (2008) Cell differentiation through tissue elasticity-coupled, myosin-driven remodeling. *Current opinion in cell biology* 20(6):609-615.
65. Olins AL & Olins DE (2004) Cytoskeletal influences on nuclear shape in granulocytic HL-60 cells. *BMC cell biology* 5:30.
66. Zhen YY, Libotte T, Munck M, Noegel AA, & Korenbaum E (2002) NUANCE, a giant protein connecting the nucleus and actin cytoskeleton. *Journal of cell science* 115(Pt 15):3207-3222.
67. Jaenisch R & Bird A (2003) Epigenetic regulation of gene expression: how the genome integrates intrinsic and environmental signals. *Nat Genet* 33 Suppl:245-254.
68. McBeath R, Pirone DM, Nelson CM, Bhadriraju K, & Chen CS (2004) Cell shape, cytoskeletal tension, and RhoA regulate stem cell lineage commitment. *Developmental cell* 6(4):483-495.
69. Pacary E, *et al.* (2006) Synergistic effects of CoCl₂ and ROCK inhibition on mesenchymal stem cell differentiation into neuron-like cells. *Journal of cell science* 119(Pt 13):2667-2678.
70. Jones PA & Baylin SB (2002) The fundamental role of epigenetic events in cancer. *Nature reviews. Genetics* 3(6):415-428.
71. Gaudet F, *et al.* (2003) Induction of tumors in mice by genomic hypomethylation. *Science* 300(5618):489-492.
72. Eden A, Gaudet F, Waghmare A, & Jaenisch R (2003) Chromosomal instability and tumors promoted by DNA hypomethylation. *Science* 300(5618):455.

73. Dodge JE, *et al.* (2005) Inactivation of Dnmt3b in mouse embryonic fibroblasts results in DNA hypomethylation, chromosomal instability, and spontaneous immortalization. *The Journal of biological chemistry* 280(18):17986-17991.
74. Ley TJ, *et al.* (2010) DNMT3A mutations in acute myeloid leukemia. *The New England journal of medicine* 363(25):2424-2433.
75. Esteller M, Corn PG, Baylin SB, & Herman JG (2001) A gene hypermethylation profile of human cancer. *Cancer research* 61(8):3225-3229.
76. Wilson AS, Power BE, & Molloy PL (2007) DNA hypomethylation and human diseases. *Biochimica et biophysica acta* 1775(1):138-162.
77. Irizarry RA, *et al.* (2009) The human colon cancer methylome shows similar hypo- and hypermethylation at conserved tissue-specific CpG island shores. *Nature genetics* 41(2):178-186.
78. Futscher BW, *et al.* (2002) Role for DNA methylation in the control of cell type specific maspin expression. *Nature genetics* 31(2):175-179.
79. Feinberg AP (1999) Imprinting of a genomic domain of 11p15 and loss of imprinting in cancer: an introduction. *Cancer research* 59(7 Suppl):1743s-1746s.
80. Holm TM, *et al.* (2005) Global loss of imprinting leads to widespread tumorigenesis in adult mice. *Cancer cell* 8(4):275-285.
81. Ito Y, *et al.* (2008) Somatically acquired hypomethylation of IGF2 in breast and colorectal cancer. *Human molecular genetics* 17(17):2633-2643.
82. Belinsky SA (2004) Gene-promoter hypermethylation as a biomarker in lung cancer. *Nature reviews. Cancer* 4(9):707-717.
83. Belinsky SA, *et al.* (2004) Plutonium targets the p16 gene for inactivation by promoter hypermethylation in human lung adenocarcinoma. *Carcinogenesis* 25(6):1063-1067.
84. Esteller M (2008) Epigenetics in cancer. *The New England journal of medicine* 358(11):1148-1159.
85. Jones PA & Baylin SB (2007) The epigenomics of cancer. *Cell* 128(4):683-692.
86. Fraga MF, *et al.* (2005) Loss of acetylation at Lys16 and trimethylation at Lys20 of histone H4 is a common hallmark of human cancer. *Nature genetics* 37(4):391-400.
87. Varier RA & Timmers HT (2011) Histone lysine methylation and demethylation pathways in cancer. *Biochimica et biophysica acta* 1815(1):75-89.
88. Portela A & Esteller M (2010) Epigenetic modifications and human disease. *Nature biotechnology* 28(10):1057-1068.
89. Bolden JE, Peart MJ, & Johnstone RW (2006) Anticancer activities of histone deacetylase inhibitors. *Nature reviews. Drug discovery* 5(9):769-784.

90. Rodriguez-Paredes M & Esteller M (2011) Cancer epigenetics reaches mainstream oncology. *Nature medicine* 17(3):330-339.
91. Bracken AP & Helin K (2009) Polycomb group proteins: navigators of lineage pathways led astray in cancer. *Nature reviews. Cancer* 9(11):773-784.
92. Lekka M, *et al.* (1999) Elasticity of normal and cancerous human bladder cells studied by scanning force microscopy. *European biophysics journal : EBJ* 28(4):312-316.
93. Guck J, *et al.* (2005) Optical deformability as an inherent cell marker for testing malignant transformation and metastatic competence. *Biophysical journal* 88(5):3689-3698.
94. Rosenbluth MJ, Lam WA, & Fletcher DA (2006) Force microscopy of nonadherent cells: a comparison of leukemia cell deformability. *Biophysical journal* 90(8):2994-3003.
95. Suresh S (2007) Biomechanics and biophysics of cancer cells. *Acta biomaterialia* 3(4):413-438.
96. Ward KA, Li WI, Zimmer S, & Davis T (1991) Viscoelastic properties of transformed cells: role in tumor cell progression and metastasis formation. *Biorheology* 28(3-4):301-313.
97. Mantovani A, Allavena P, Sica A, & Balkwill F (2008) Cancer-related inflammation. *Nature* 454(7203):436-444.
98. Yu H, Mouw JK, & Weaver VM (Forcing form and function: biomechanical regulation of tumor evolution. *Trends Cell Biol* 21(1):47-56.
99. Issa JP (2007) DNA methylation as a therapeutic target in cancer. *Clinical cancer research : an official journal of the American Association for Cancer Research* 13(6):1634-1637.
100. Ellis L, Atadja PW, & Johnstone RW (2009) Epigenetics in cancer: targeting chromatin modifications. *Mol Cancer Ther* 8(6):1409-1420.
101. Gossett, D. R. *et al.* Hydrodynamic stretching of single cells for large population mechanical phenotyping. *Proc. Natl. Acad. Sci.* **109**, 7630–5 (2012).

Figures

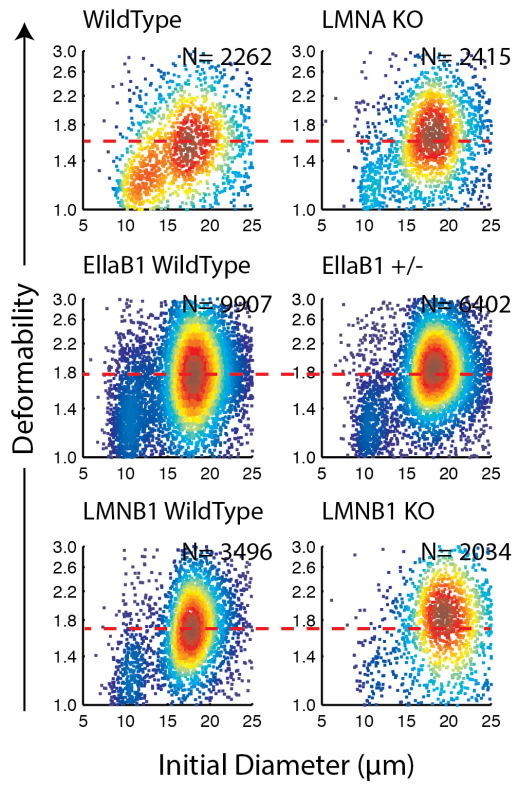


Figure 1. Deformability profiles of wildtype (left) and lamin knockout (right) mouse embryonic fibroblasts. A slight increase in deformability is detected in lamin A knockout (LMNA KO) cells compared to wildtype. Lamin B1 knockout cells (LMNB1 KO) are more deformable than Lamin B1 partial knockouts (EllaB1 +/-).

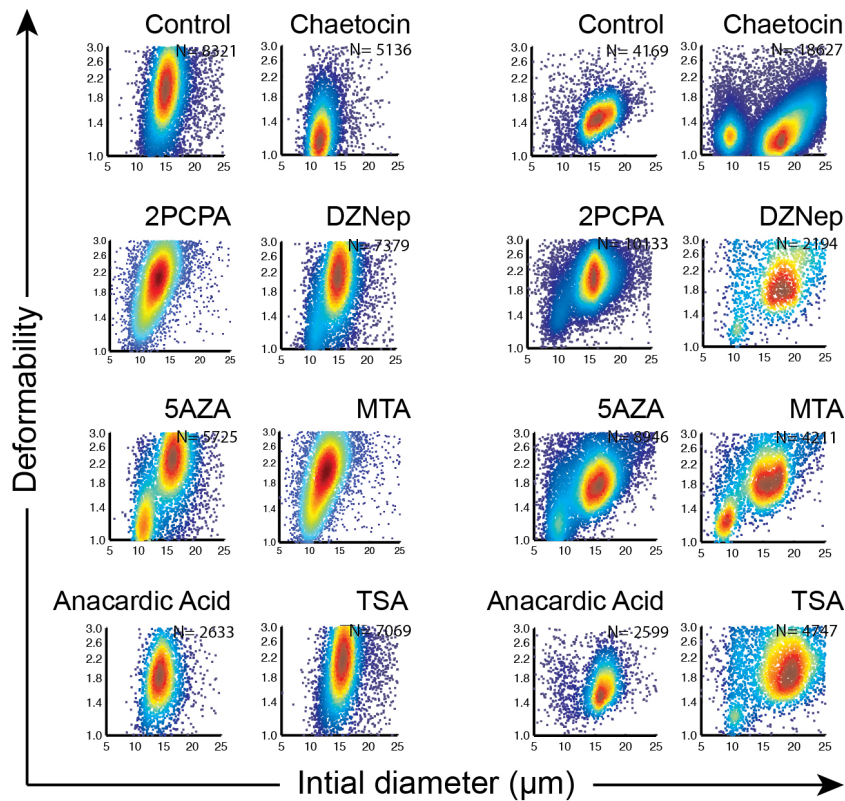


Figure 2. Jurkats acute T-cell leukemia cells (left) and NIH-3T3 fibroblasts (right) were treated with different chromatin reorganizing drugs. Compared to control, treatment with H3K9me inhibitor, chaetocin and HAT inhibitor, anacardic acid, resulted in stiffening of cells, while treatment with HDAC inhibitor TSA, HMT inhibitor DZNep and DNMT inhibitors MTA and 5AZA resulted in an increase in cell deformability.

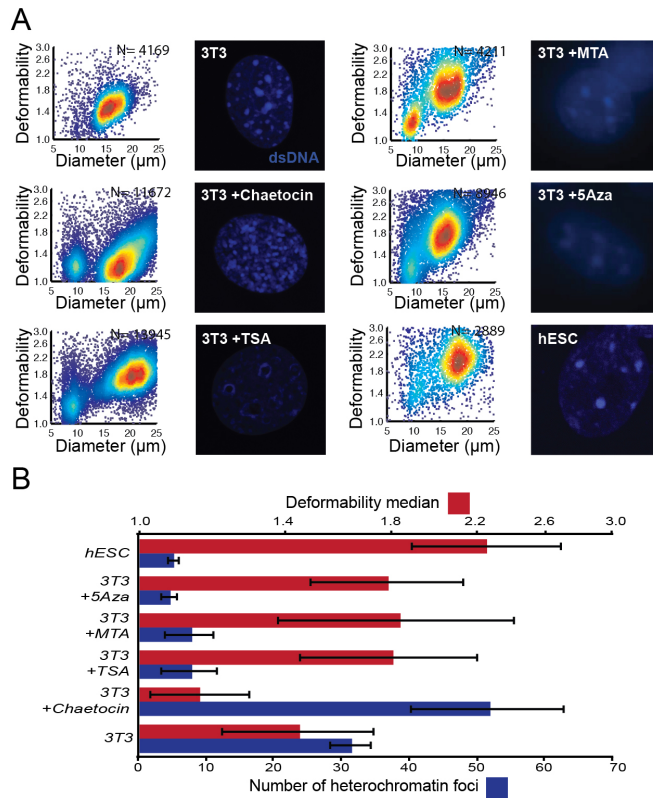


Figure 3. NIH-3T3 fibroblasts were treated with different chromatin and cytoskeletal reorganizing drugs. Human embryonic stem cells as well as fibroblasts treated with HDAC inhibitor and DNMT inhibitors that seem to have less condensed chromatin, deform more in our device, while in the case of treatment with Chaetocin, an H3K9 methylation inhibitor a smaller deformation and a highly condensed chromatin is observed (A,B).

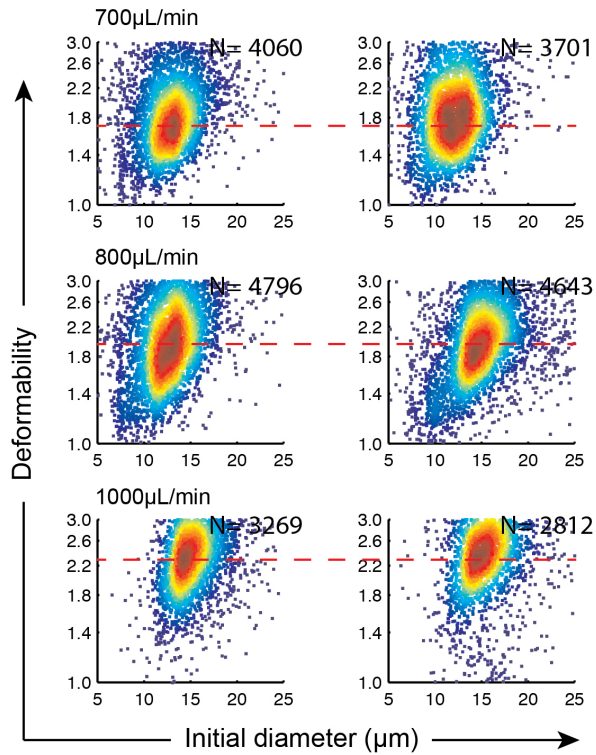


Figure 4. No significant difference in the deformability of DNMT triple knockout mouse embryonic stem cells (right column) was observed compared to wildtype cells (left column) at three different flow rates.

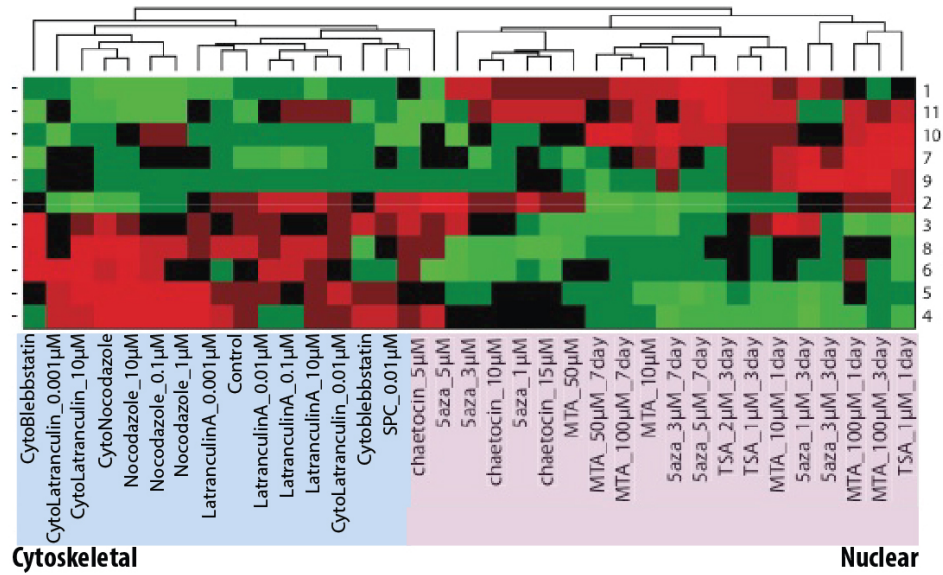


Figure 5. Using multiparameter analysis single cells were successfully classified based on the treatment.

Chapter 4

Separation of Particles Based of Aspect Ratio: Application in

Cell Sorting by Shape and Deformability

This chapter introduces microfluidic platforms for particle and cell sorting based on their shape, size and deformability. The first part of the chapter focuses on using inertial forces for separation of particles and yeast cells of different aspect ratios. We will show that particle rotation around a conserved axis following Jeffery orbits is a necessary component in producing different equilibrium positions across the channel that depend on particle rotational diameter. In the second part, we will show that by first deforming cells and then introducing them into a straight or curved channel, inertial effects are capable of separating these cells based on their size and stiffness. In other words, after being stretched into different “deformed diameters” (effective diameter), cells will focus on different equilibrium positions in the channel. Both original cell size and its stiffness contribute to its final deformed diameter. These differences are large enough to enable an efficient, continuous, label-free and high-throughput sorting and enrichment of cells of interest downstream.

Importance and challenges of separating particles by shape. Many microparticles of interest such as parasites, bacteria, viruses, but also marine organisms, and man-made powders and microparticles possess a variety of shapes. Separating particles with specific shapes from a background of other particles can aid in isolating disease-causing cells for diagnostics or particles with specific geometric properties of use in research and industry. However, the most common way of separating particles with filters (i.e. pores that restrict passage to particles below

a certain size) is not effective for this application since non-spherical particles can present different faces while interacting with the filter. Here we show how the shape of a particle will modify its location of stable accumulation while flowing through a microscale pipe under conditions in which the momentum of the fluid is important.

Fluid inertia is shown to lead to focusing of shaped microparticles in the cross-section of a channel, such that particles of different shapes occupy different positions in the channel. Particles rotate around a conserved axis while moving downstream at this focusing position, and this rotation is found to be a necessary component in producing different cross-sectional positions for particles that are dependent on particle rotational diameter. These differences are large enough to enable high-purity shape-based separation of large quantities of particles that are directed into separate outlets. The separation was applied to a large range of particle sizes and types, including small 3 μm particles and biological particles such as budding yeast with different shapes that accompany the cell life cycle.

The simple and practical approach for sorting particles by a previously inaccessible geometric parameter opens up a new capability that should find use in a range of fields from preparing standardized anisotropic particles for composite materials to synchronizing the life cycles of yeast and bacteria populations for controlled experiments.

An approach to separate shaped-particles can be used to isolate disease-causing cells for diagnostics or can aid in purifying non-spherical targets in applications ranging from food science to drug delivery. However, the separation of shaped-particles is generally challenging, since non-spherical particles can freely rotate and present different faces while being sorted. We experimentally and numerically show that inertial fluid dynamic effects allow for shape-

dependent separation of flowing particles (spheres and rods with aspect ratios 3:1 and 5:1 all were separable). Particle rotation around a conserved axis following Jeffery orbits is found to be a necessary component in producing different cross-sectional positions that depend on particle rotational diameter. These differences are large enough to enable high-purity, continuous, passive and high-throughput shape-based separation downstream. Furthermore, we show that this shape-based separation can be applied to a large range of particle sizes and types, including small 3 μm particles and bio-particles such as yeast. The demonstrated enrichment of budded yeast from an unsynchronized population can be particularly useful for synchronization and study of stochasticity in cell behavior. This practical approach for sorting particles by a previously inaccessible geometric parameter opens up a new capability that should find use in a range of fields.

Shape represents one of the most important factors to specifically identify a bioparticle¹. Among others, shape is a marker of cell cycle. For example, eukaryotic cells such as yeast show cell-cycle dependent changes in their shape as a budding daughter cell forms attached to the mother cell². Shape is also an indicator of cell state of use in clinical diagnostics. For example, blood cell shape-changes accompany many diseases, such as modified red blood cell morphology resulting from sickle cell disease, anaemia or malaria^{3,4}. Thus, shape can be a specific marker in bioparticle separation and may serve as a useful new basis for passive particle fractionation. More generally, many particles of interest such as parasites, bacteria, viruses, but also marine organisms^{5,6}, man-made microparticles like barcoded substrates^{7,8} or cement microparticles possess a variety of shapes and the ability to prepare particular shapes at high purities enables subsequent clinical, industrial, and research applications.

Given that traditional pore-based filtration is ineffective with bioparticles that may be

deformable or possess unique shapes, a diverse set of methods have recently emerged to achieve continuous separation of cells/microparticles ⁹. Some approaches combine microfluidic flow with a force field, such as electric, magnetic, optical, acoustic, or with biochemical interactions (selective lysis or antigen/antibody capture) ^{10–13}. Other approaches are based on passive hydrodynamics in microchannels, for example micro filtration ¹⁴, pinched flow fractionation (PFF) and hydrodynamic filtration (HDF) ^{15,16}, hydrophoresis ^{17–22}, deterministic lateral displacement (DLD) around pillars ²³ and inertial separation in curved channels or spirals ^{24–26}.

However, particle shape has not been considered in most of these separation techniques. Only recently, have researchers investigated hydrodynamic filtration (HDF), deterministic lateral displacement (DLD) and dielectrophoresis (DEP) for shape-based separations. Beech et al. first recognized the need to separate shaped parasites from within blood and implemented an approach using the DLD technique ²⁷. DLD devices consist of post networks in which spatial arrangement defines a size cut-off of separation (or critical radius). DLD has been demonstrated to enable a separation based on particle morphology, via control of particle orientation, and particle deformability, via control of shear stress ²⁸. Holm, Beech et al. applied this technique for the separation of trypanosomes from red blood cells ²⁹ and for the classification of morphologically altered red cell ²⁸. More recently, Sugaya et al. applied HDF for shape-based sorting of budding/single cells from a yeast cell mixture ³⁰. HDF is based upon differential particle behavior in a fluid branch point due to steric exclusion, with the separation size cut-off being determined by the channel fluidic resistance ratio. Similarly to DLD, the rotation of non-spherical particles modifies their effective steric dimension. Both HDF and DLD are efficient, passive and continuous techniques but both require (i) highly complex features (130 branch channels for HDF ³⁰, complex and high-resolution arrays of posts with 13 different arrangements

for DLD ²⁸) and (ii) low flow rates (60 nL/min for Holm et al. ²⁹ and 2-3 μ L/min for Sugaya et al. ³⁰), consequently offering a low throughput that may be suitable for research applications but not industrial-scale applications. Similarly, Valero et al. performed shape-based sorting of yeast by balancing opposing dielectrophoretic (DEP) forces at multiple frequencies³¹. DEP requires the integration of active elements and a precise and reproducible control of the buffer conductivity between each experiment, which both complicate potential use beyond research applications.

Recently, Di Carlo and others have shown that inertial focusing, based on inertial migration effects in cylindrical pipes first observed by Segre and Silberberg ³², can be used to separate microparticles and cells in microchannels at high rates ^{26,33–35}. Briefly, two inertial lift forces are involved: (i) a shear gradient lift force and (ii) a wall effect lift force induce particle migration across streamlines when the particle Reynolds number, Rp , is of order 1 or greater. $Rp = Re(a/W)^2$ with a/W being the ratio of particle to channel diameter, and Re indicates the Reynolds number for the channel flow, $Re = \rho UmW/\mu$. Here, ρ , Um , and μ correspond to the density, maximum velocity, and dynamic viscosity of the fluid. In rectangular or square channels, particles generally migrate to two to four distinct dynamic equilibrium positions depending on the fold symmetry of the channel cross-section (Fig. 1). Among other advantages, the possibility of operating over a large range of high flow rates makes inertial focusing a promising technique for low cost cytometry, massively parallel cell separation and washing ^{36,37}. However, previous work has mainly investigated spherical particles and characterized the ability of inertial focusing to separate or focus particles/cells based on the overall particle diameter ²⁶. Recently, deformability-based differences in equilibrium positions for cells and viscous droplets were demonstrated ³⁸. Some of the current authors also showed that inertial effects can be exploited to focus non-spherical particles to uniform locations ³⁹, illustrating that the effect of particle shape

on its focusing position is an important parameter to be further investigated.

Here we evaluate how the shape of a particle, while conserving volume, will modify its motion and its dynamic equilibrium position in a microchannel under inertial conditions, and use these differences to perform shape-based separations. Rod-like particles migrate to a stable position closer to the channel centerline than spherical particles with the same volume, and align such that they periodically “tumble” rotating around a short axis following Jeffery orbits, and are pushed away from the channel wall. Numerical simulations and experimental results both yield focusing positions that are dependent on the particle’s largest cross-sectional dimension and simulations indicate particle rotation is necessary for this behavior. From these shape-based differences in focusing positions, we demonstrate passive and high-throughput separation using a particle’s largest cross-sectional dimension as a distinguishing marker, independent of the smallest dimension of the particle. We applied this separation to the efficient and high-throughput sorting of budding yeast in view of cell-cycle synchronization (at rates of 60 $\mu\text{L}/\text{min}$ or 1500 cells/s compared to 100 cells/s in previous work ³¹). Next, by integrating this design with deformability cytometry we show the feasibility of cell separation by its deformability and size.

Importance and challenges of separating particles by deformability. Biophysical (mechanical) properties of cells are promising biomarkers indicative of changes in cellular phenotype associated with malignancy. These label-free biophysical markers can be used to purify cells of interest at lower cost than currently available techniques. Cell size and stiffness are among the most important label-free markers. It has recently been reported that despite the relative stiffness of tumor masses compared to neighboring healthy tissues, cancer cells are in fact softer than their healthy counterparts. The increased deformability of cells associated with their malignancy is actually suggested to be relevant to their ability to migrate through tissues

and metastasize. Previous studies report up to 3.5 times higher compliance associated with metastatic cancer cells disseminated in pleural fluids compared to benign cells. Malignant cells in body fluids are also shown to be larger than the background of white and red blood cells. Concentrating malignant cells and removing large populations of leukocytes that interfere with the molecular analysis, can improve cytological diagnosis accuracy and can lead to more accurate detection of specific gene mutations for targeted drug therapies. Therefore, the ability to uniquely separate highly deformable large cells can significantly improve the enrichment of malignant cells. However, there are no current methods that specifically sort particles by their deformability. Beyond pleural fluid analysis, rapid, automated processing of large volumes of bodily fluids and purification of malignant cells of interest will impact a variety of clinical and drug discovery areas including urinalysis, analysis of peritoneal fluids, hematopoietic cell purification from bone marrow, and mesenchymal stem cell purification from lipoaspirates.

Traditional cytological examinations are only successful to identify malignant cells in around 60% of cases. Due to the presence of large populations of contaminating cells in body fluids, only a subset of these fluids can be analyzed for clinically-valuable mutations. These background of non-malignant cells, which are often smaller and/or stiffer than cancer cells, contain wild type DNA, and can interfere with the identification of gene mutations. High purity samples of malignant cells are necessary for accurate sequencing that can guide targeted drug treatments. Therefore, extracting and purifying these malignant cells from larger volumes of body fluids with high efficiency and purity could improve cytology-based diagnoses. Examples of this application include isolation of malignant cells (mainly leukemia, lymphoma and disseminated cancer cells from lung and breast) from pleural effusions, isolating circulating

tumor cells in peripheral blood and isolating mesenchymal stem cells (MSCs) from lipoaspirates or bone marrow aspirates.

Current methods of isolating these cells are costly, and require pre-knowledge of the potential cancer origin and therefore are not clinically practical. Laser capture microdissection (LCM) and other manual selection techniques have been successfully applied to enrich cancer cells from body fluids resulting in detection of EGFR and KRAS mutations associated with sensitivity and resistance to EGFR tyrosine kinase inhibitors, respectively ^{40,41}. However, these techniques are laborious, slow and unlikely to be used routinely in the clinic. Therefore robust, low cost and rapid approaches are needed to process large volumes of fluid and sort out malignant cells into a small volume for molecular analysis. Conventional cell sorting strategies, including fluorescence-activated cell sorting (FACS) and magnetic-activated cells sorting (MACS), mainly rely on specific antigens to distinguish between cell types, requiring pre-knowledge of the cancer type and expression levels. Although FACS and MACS allow high-throughput screening and sorting, their complexity and high initial, as well as operating costs limit their use as simple cost-effective approaches. Therefore, there is a clinical need for low cost cell sorting approaches, which can take advantage of physical biomarkers to sort different cell populations without costly external labels.

Laser capture microdissection (LCM) and other manual selection techniques are the main current approaches for enrichment of cancer cells, which are laborious, slow and unable to analyze a large volume of fluids. Conventional cell sorting strategies including FACS and MACS mainly rely on external labels to distinguish between cell types, which requires pre-knowledge of the potential mutations. Fluorescence-activated cell sorting (FACS) is a commonly used active sorting method, offering up to four-way cell sorting based on fluorescent emission.

Magnetic-activated cell sorting (MACS) is a passive separation technique that uses antibody-conjugated magnetic beads to separate out cells of interest. Although FACS and MACS allow high-throughput screening and sorting, their complexity and high initial, as well as operating costs limit their application as cost-effective approaches. Therefore, there is a lot of interest in “label-free” cell sorting approaches, which mainly rely on manipulating physical biomarkers to sort different cell populations. Current methods of isolating malignant cells are costly, and require pre-knowledge of the potential cancer origin and therefore are not clinically practical. Therefore robust and fast approaches are needed to process large volumes of fluid and sort out malignant cells into a small volume.

An emerging trend in anti-cancer therapy is the use of pharmacological agents that target specific molecular pathways that are affected by common genetic lesions. These targeted therapies can be particularly effective without causing many of the significant side-effects that occur with traditional chemotherapy that acts upon actively dividing cells with less specificity. Examples of successful targeted therapies include the tyrosine kinase inhibitors gefitinib and erlotinib which target EGFR-activating mutations in non-small-cell lung cancer (NSCLC) ⁴²; anti-HER2 agents trastuzumab and lapatinib in breast tumors over-expressing HER2/ERBB2 ⁴³; and imatinib, nilotinib and dasatinib which are effective against BCR-ABL fusions in chronic myeloid leukemia ⁴⁴. Importantly, these drugs are not efficacious in patients who do not have a tumor with the specific molecular lesions. In addition, efficacy drops due to emergence of resistance that is associated with another set of possible mutations (for the breast cancer example this includes activating mutations in *PI3K* or loss of function mutations in the phosphatase PTEN) ⁴³.

Therefore, treatments must be individualized following a companion diagnostic - molecular analysis of the tumor to determine the presence of particular target mutations and lack of resistance mutations. In some cases the primary tumor can be biopsied and high purity cancer cells can be analyzed. However, often the primary tumor has been previously resected or is otherwise inaccessible, and biopsy is not a viable option (due to risk to the patient) ⁴⁵. In these cases, disseminated cancer cells can be found at much lower quantities and purity in body fluids: blood (circulating tumor cells – CTCs), peritoneal or pleural fluids, and urine. “Liquid biopsies” of cells from these relatively non-invasive sources are particularly ideal, but the challenge of isolating and enriching pure populations of cancer cells from the large background of contaminating cells remains. High purity aids in various methods of mutational analysis from cytopathology stains and fluorescence *in situ* hybridization (FISH) to gene expression analysis and sequencing. For example, increasing purity reduces the likelihood of false positive detection of a mutation by PCR or gene sequencing ^{46,47}.

Beyond separation of malignant cells from body fluids, being able to sort particles passively by deformability and size has additional applications. Activated leukocytes that are involved in disease processes like sepsis and transplant rejection may be able to be sorted based on their deformability and removed to lower cytokine levels and improve clinical outcomes. Remaining pluripotent stem cells could be sorted from differentiated batches to prevent implantation and subsequent teratoma (tumor) formation. For life science research, pure populations of a variety cell types associated with a deformable phenotype could be analyzed to determine molecular differences leading to this phenotype.

As discussed above, physical properties of cells are attractive biomarkers, due in part to their independence from expensive and overly-specific molecular markers. Increased cellular

deformability (the ability to change shape under a load) and size have repeatedly been shown to be specific biomarkers for malignancy, but sorting cells based on these properties is challenging. The increased deformability of malignant cells is purportedly linked to their ability to migrate through tissues and metastasize. Previous studies using atomic force microscopy (AFM) reported the deformability of metastatic cancer cells disseminated in pleural fluids was up to 3.5 times higher than that of benign cells; however, only tens of cells could be measured in a meaningful time and only after first identifying cells based on specific staining. All in agreement, several methods of assaying cell deformability, including AFM, micropipette aspiration, and optical stretching, have reported increases in deformability of malignant populations of cells compared to benign cells.

Our lab has previously introduced the deformability cytometry technique which can deform thousands of cells per second to aid in pleural fluid diagnostics. This technology applies large strains (greater than 50%) to cells in an extensional (purely stretching) flow. This high-throughput cell deformability measurement technique can measure over 1,000 cells/second without user input or pre-selection. In a study of 119 patients, using the validated deformability cytometry technique⁴⁸, we have also measured substantially increased deformability and size for cells in malignant pleural fluid samples, in agreement with similar measurements of model cell lines. Median cell deformability was around 77%, 67%, 85% higher in patients with mesothelioma, breast, and lung cancer, respectively. Cell diameter was also around 50%, 36%, and 44% higher for patients with mesothelioma, breast and lung cancer (Fig. 12). However, this instrument can only measure these cell properties but there remain challenges to subsequently sort based on these properties. Therefore, the ability to uniquely separate highly deformable large

cells can significantly improve the enrichment of malignant cells. However, there are no commercially available methods that specifically sort particles by their deformability.

Results

Particle motion in microchannels depends on shape. In Stokes flow, the linearity of the equations of motion leads to the absence of lift forces on particles with sufficient rotational symmetry (such as the ellipsoids investigated here) ⁴⁹. Therefore, one must rely on the effects of inertia ²⁶, particle deformability ³⁸, or the non-Newtonian nature of the fluid itself ⁵⁰ to establish shape-dependent lift-induced positions of equilibrium within a microchannel. For common applications that are concerned with rigid particles in a Newtonian fluid such as water, one relies on inertia alone.

With finite inertia, ellipsoid particles migrate to inertial focusing positions within microchannels and undergo different modes of rotational motion. We classified the rotational configurations qualitatively as “*in plane rotation*” when the particle rotates around the y-axis, “*out of plane rotation*” when the rotation contains components around the x-axis and “*no rotation*” when the particle does not rotate while moving downstream (Fig. 2A). At low particle Reynolds numbers (Rp) (calculated for a sphere with the same volume) since the particles are not focused, their rotation is random and rather than a pure “*in plane rotation*”, “*out of plane*” or “*no rotation*” mode, they exhibit a mix of rotational behaviors. If the particle rotates in any manner other than a pure “*in plane*” mode, its rotation is classified to be “*out of plane*”. At Rp of 0.3, 52% of particles exhibit some out of plane rotational behavior which occurs more often compared to 39% that exhibit pure “*in plane*” rotation. As the flow rate and particle Reynolds

number (Rp) increases from 0.3 ($Q=20 \mu\text{L}/\text{min}$) to 0.75 ($Q=50 \mu\text{L}/\text{min}$), the frequency of “*in plane rotation*” increases with a corresponding reduction in the other two modes. These differences can be explained since at higher Rp , more complete migration to the dominant focusing positions on the long edges of a rectangular microchannel are expected. Along these edges, particles rotate around the axis of highest vorticity, perpendicular to this long face, leading to a more uniform “*in plane*” rotational motion. For these well-focused particles the uniform behavior for rotation is a tumbling motion, or periodic flipping around the long axis that is not rotationally symmetric. Rotational motion of ellipsoidal particles in flow has been previously observed by Jeffery and others^{51–53}. Unlike our results, Jeffery did not predict a single axis of rotation but an infinite set of stable orbital motions that depended on initial conditions. However, addition of a little inertia for the fluid or particle has been suggested to lead to the precession of particle orbits to a stable rotational axis in a shear (or parabolic flow)⁵⁴. Our results confirm these predictions through the convergence of rotational modes to a single “*in plane*” mode when increasing Rp from 0.3 to 0.75.

The period of rotational motion, T , is dependent on particle shape. Jeffery (1922) demonstrated that an isolated inertialess ellipsoid in an unbounded linear shear flow field undergoes a periodic closed orbit around the vorticity axis⁵¹. The orbit period of an ellipsoid with aspect ratio R is given by

$$T_{orbit} = \frac{2\pi}{\gamma} \left(R + \frac{1}{R} \right)$$

where γ is the local shear rate. The experimentally observed rotational dynamics of ellipsoidal particles (aspect ratio, $R = 1:3$ and $1:5$) in a channel flow follows a similar dependence of rotational period on ellipsoid aspect ratio,

with an increasing rotational period for longer particles (Fig. 2).

Since the Jeffery orbit is distinctive, the reproduction of similar trends in simulation is a strong indication that the correct dynamics have been captured. From our simulations, the trajectories of particles (center of mass) at different initial positions converge to an equilibrium position. The trajectories oscillate when particles are close to the wall, which is due to the rotation of the ellipsoidal particles (Fig. 3). The period of oscillation predicted by our simulation and the Jeffery formula for particles with aspect ratio 1:3 (Fig. 2C, E) and 1:5 (Fig. 2D, F) in channels with aspect ratios of 0.64 (Fig. 2C, D) and 0.74 (Fig. 2E, F) largely agree with each other and the experimental results, suggesting only small contributions from finite inertia and the curvature of the velocity field. Note that a larger deviation from the Jeffery predictions is observed for particles with a 5:1 aspect ratio. It is likely that for these longer particles, the gradient in the velocity in our channels plays a larger role in rotational dynamics. Unlike for Jeffery orbits, in our system, the shear rate is not identical throughout the flow, but reverses direction at the channel centerline and increases towards the wall. The longer 5:1 particles are exposed to regions of flow reversal (relative to the particle frame of reference) across the channel centerline from where focusing occurs. These particles are observed to rotate slower (longer period of rotation) than Jeffery predictions that rely solely on the local shear rate at the particle center (Fig. 2G).

The dominant tumbling rotational motion suggests a mechanism by which particles of differing aspect ratios focus to unique positions within a channel cross-section. Since the particle shape is not spherical, when the major axis rotates to the orientation perpendicular to the plane of the wall, wall effect lift increases substantially due to the closer distance, acting to push the particle away from the wall. When the major axis aligns to the flow, wall effect lift decreases,

and the particle migrates back towards the wall. Relative dominance in the lift away from the wall vs. towards the wall integrated over time as the particle tumbles would suggest average equilibrium positions closer to the centerline for higher aspect ratio particles. That is, wall effect lift away from the wall is strongly dependent on distance from the wall and becomes much stronger than the balancing shear-gradient lift in the near wall region which rotating ellipsoids can sample.

Particle shape influences the location of the steady-state focusing position. Particles with different shapes have different inertial equilibrium positions. This variation in equilibrium position is seen in histograms of particle lateral position for channels with aspect ratios of 0.53, 0.64 and 0.74 and flow rates from 20 to 110 $\mu\text{L}/\text{min}$ (Fig. 4, Fig. 5). The possibility of particle separation at each condition is better characterized through plotting a parameter related to differences in equilibrium position and the variation in this position for the population of particles, *Separability Factor* ($SF_{\text{Type1-Type2}}$) (Equation 1). Practically, $SF_{\text{Type1-Type2}}$ indicates the expected separation performance and was calculated as the difference in average focusing positions (X_{eq}) between two particle shapes, normalized by the average of their standard deviations (Fig. 6):

$$SF_{a/b} = \frac{|X_a - X_b|}{\text{mean}(SD_a, SD_b)} \quad (1)$$

In 35 μm wide channels (channel aspect ratio closer to 1), at Reynolds numbers higher than 10, inertial effects start to concentrate both spherical and rod-shaped particles (Fig. 4A). Spheres start to accurately focus and occupy four focusing positions, while rods are largely spread along the channel width. As fluid inertia increases ($Re=72$, $Q=110 \mu\text{L}/\text{min}$), spherical particles migrate

to locations closer to the walls when compared to higher particle aspect ratios (Fig. 4B). Additionally, some of the particles are focused to other positions, on the top and bottom faces of the channel. The existence of four equilibrium positions, expected for such aspect ratios (0.74), is problematic for separation applications. Decreasing channel width from 35 to 30 μm changes the aspect ratio of the channel cross-section to 0.64, which leads to migration to only two distinct equilibrium positions. At 30 $\mu\text{L}/\text{min}$ ($Re=21$), 1:5 rods were initially separated from spheres and 1:3 rods (Fig. 3.D); $SF_{Spheres/Rods1:3}=0.24$, $SF_{Rods1:3/Rods1:5}=2.26$. As Q was increased to 40 $\mu\text{L}/\text{min}$ ($Re=28$), both families of rods migrate further away from spheres and from each other (Fig. 3.E), suggesting the possibility of a better shape-based separation; $SF_{Spheres/Rods1:3}=0.85$, $SF_{Rods1:3/Rods1:5}=1.46$. As Re was increased further ($Re=49$, 70 $\mu\text{L}/\text{min}$), rods tended to move closer to the walls where spheres are located, reducing the gap between focusing positions (Fig. 3.F); $SF_{Spheres/Rods1:3}=1.05$, $SF_{Rods1:3/Rods1:5}=0.61$. Decreasing channel width further to 25 μm , aspect ratio 0.53, makes it difficult to uniquely focus all particles. Indeed, even at $Re=37$ (50 $\mu\text{L}/\text{min}$), 1:5 rods are still not focused to a unique streamline (Fig. 4H). This result is also partly due to the fact that, especially with larger rods, this narrow channel is prone to clogging. These results clearly suggest that optimum conditions exist that maximize the distance between particle positions and allow for the most efficient particle separation based on aspect ratio. The experiments also suggest that above a cut-off Re where particles are already focused, increasing Re further will result in the convergence of focusing positions for all three particles to a position closer to the wall. This agrees with previous numerical analysis by Di Carlo et al.⁵⁵ Wall-directed shear-gradient lift force increases faster with increasing Re than the balancing wall-effect lift, leading to a shift in equilibrium position closer to the wall. Convergence of the focusing positions for normally segregated shaped particles is likely due to this effect acting

more strongly on particles with initial focusing positions further from the wall.

Spheres with similar rotational diameter predict focusing positions for rod-shaped particles. Whatever the channel aspect ratio, experimentally determined focusing positions agree best with the hybrid computational method that allows for simulation of *Rotating rods*. Simulations with *Aligned rods* constrained not to rotate and with the major axis pointed in the flow direction exhibit significant differences in comparison with experiments (Fig. 7), with high aspect ratio particles occupying equilibrium positions significantly closer to the wall than is experimentally observed. These results further implicate strong lift during rotation as responsible for shape- dependent differences in focusing. Aligned rods cannot rotate freely following Jeffery orbits, in which the rods are periodically pushed away from the wall. Simulations with *Spheres* $D=b$ (spheres with diameter corresponding to the minor axis of the particle) do not match the experimental results well either. However, simulations with spheres with diameters corresponding to the major axis of the particle (*Spheres* $D=a$) align with the experimental results much more closely (Fig. 7D-F). This indicates that rod-shaped particles with 180° rotational symmetry follow the focusing trend of spheres with similar rotational diameter. These results agree with those obtained recently with other shapes and larger dimensions³⁹, and provide a simple approach to model and predict focusing positions for non-spherical particles. Particles without this rotational symmetry would be subject to additional non-inertial lift forces following the work of Bretherton⁴⁹.

Application to shape-based separation. Using the significant differences in lateral equilibrium position emphasized above, we conducted label-free enrichment and collection of shaped particles. Fig. 8 illustrates the separation results for several configurations of SAPS (shape-activated particle sorting) devices, where the experimental parameters (channel aspect

ratio and flow rate) were chosen based on the separability results previously obtained (Fig. 6). To quantify the efficiency of separation, we report three parameters defined in the methods: Extraction Yield (*EY*), Extraction Purity (*EP*) and Enrichment Ratio (*ER*) (Fig. 8D-F, SI movie). To better achieve specific separations, we have designed devices with three arrangements of outlet resistances, which provide separate relative capture ratios of the fluid at different outlets (Fig. 8A-C).

By tuning device parameters we demonstrate a range of possible separations between spheres, 1:3 rods, and 1:5 rods. The SAPS device A, 25 μm wide ($ARc = 0.53$), with identical fluidic resistance for each outlet is shown in Fig. 5A. For this design most spheres and 1:3 rods exit from outlet 1, while 1:5 rods are predominantly captured from outlet 2 (Fig. 8D). In agreement with *SF* measurements for these flow conditions (Fig. 6), 1:5 rods were found to have a high extraction yield in outlets 2 and 4 (86% of 1:5 rods) with up to 90% purity, compared to 1:3 rods and spheres which were mainly collected together in outlets 1 and 5 (83% of all spheres and 70% of all 1:3 rods injected). To achieve another scenario of separation and with a higher flow rate, we tuned the experimental conditions to a channel aspect ratio of 0.64, and a flow rate of 80 $\mu\text{L}/\text{min}$ (SAPS device B, Fig. 8B) and we modified the ratio of fluidic resistance between the different outlets ($\alpha_{1:2} = 3/4$, $\alpha_{1:3} = 1/2$). Contrary to before, we achieved excellent extraction yield for spherical particles (**85%** of all spheres were found in outlets 1 and 5), while both types of rods were collected together (90% of all rods are extracted in outlets 2 and 4), leading to an extraction purity of **96%** for spheres (Fig. 8H, K). These results are still in agreement with *SF* values. Decreasing the flow rate to 60 $\mu\text{L}/\text{min}$ in a 30 μm ($ARc = 0.64$) channel allows for separating all three types of particles while slightly decreasing the purity of spheres, as predicted by *SF* measurements. The presence of 7 outlets in SAPS device C (Fig. 8C) provides a more

accurate separation between streamlines (SAPS device C, $\alpha_{1:2}=3/4$, $\alpha_{1:3}=1/2$, $\alpha_{1:4}=1/4$). Indeed, we isolated **88%** of spheres in outlets 2 and 6 with 87% purity, **49%** of 1:5 rods in outlet 4 with 78% purity, and more interestingly **77%** of 1:3 rods with 80% purity (Fig. 8I, L).

We have also examined and confirmed the possibility of separation of 3 μm spheres and 3 μm derived-ellipsoids with three different aspect ratios by applying the same concept as was used for separating 6 μm beads with slightly modified parameters. Using SAPS device D (Fig. 9 A), we collected spheres in outlets 1 and 5 with 90% yield (*EY*) and up to 90% purity (*EP*), as well as 81% yield of 1:3 rods in outlets 2,3 and 4, and 97% yield of 1:5 rods in outlets 2,3 and 4 with up to 88% purity (*EP*) of the two types of rods (Fig. 9B-D).

Application to passive and high-throughput yeast sorting. Shape-based separation using inertial effects allows for yeast cell sorting and cell cycle synchronization. Understanding of the cell cycle is the subject of current research, which is often explored using yeast cells (*S. cerevisiae*) because of the well-known genetics and characteristic shape changes; budding yeast cells elongate from a sphere to a bispherical twin or a larger aggregate^{2,56}. To understand gene expression profiles specific to each of these stages, it is necessary to synchronize the yeast cell-cycle. This synchronization at given cycle-stages is generally done (i) by using chemicals (metabolic agents) which disturb the cell physiology or using a temperature increase, or (ii) by size-based elutriation, which isolates the smaller cells⁵⁷. The first methods interfere with the cell metabolism, while elutriation only provides young cells not yet in active division⁵⁸. Thus, there remains a need for a non-invasive and drug-free continuous method for shape-based yeast cell sorting and synchronization³¹.

Using the SAPS device C previously described ($ARc = 0.64$, 7 outlets with $\alpha_{1:2}=3/4$, $\alpha_{1:3}=$

1/2, $\alpha_{1:4} = 1/4$), we conducted yeast sorting at various flow rates. Fig. 10 summarizes the separation results obtained at 60 $\mu\text{L}/\text{min}$, with pictures showing outlet contents. Non-dividing singles were found to have a high extraction yield in outlets 2 and 6 (90% of small singles and 91% of large singles are recovered in these outlets), with up to 94% purity, while budded yeast cells were mainly collected in outlets 3 and 5 (54% of budded yeast, with up to 31% of purity, compared to 6.6% purity at the inlet). The higher throughput of our SAPS device (60 $\mu\text{L}/\text{min}$ i.e. 1500 cells/s compared to 100 cells/s in previous work ³¹) could be further increased an order of magnitude by increasing cell concentration and by parallelization of the focusing channels, as demonstrated previously in our laboratory ³⁶. Purity and enrichment especially needed for this synchronization application could be improved by cascading devices in series.

Application to passive and high-throughput enrichment of malignant cells by size and deformability in pleural fluids. This work is the first of its kind to demonstrate passive, simple, continuous and high-throughput approach for automated processing of large volumes of bodily fluids for rapid label-free fractionation of cells based on deformability and size. The approach integrates several critical advances in microfluidic automation to yield a low-cost instrument that will expand the use of and improve the accuracy of companion diagnostic assays: **(1)** the microfluidic cartridge will accept cells from a pleural fluid sample directly after erythrocyte-specific lysis (Fig. 11, Step 1), without multi-step antibody labeling and washing procedures, and deform them at high speeds in a continuous flow using hydrodynamic stretching technology (Fig. 11, Step 2). The method operates by focusing cells into a continuous stream using passive inertial focusing ^{33,48}, and cells are subsequently hydrodynamically stretched in an extensional flow, achieving large strains (greater than 50%). The magnitude of cell deformation is defined by each cell's intrinsic physical properties (or deformability). **(2)** The stretched cells are then

passively sorted, based on their rotational diameter (deformed diameter), into a number of outlets by exploiting previously demonstrated inertial microfluidic techniques to separate by shape ⁵⁹ (Fig. 11, Step 3). The differences between the deformed diameter of cells are large enough to enable an efficient, continuous, passive separation downstream. These channels will be designed with recent insights into how inertial lift forces act on rotating non-spherical (deformed) cells and particles ⁵⁹. This technique not only enables sorting of malignant cells in pleural effusions but could potentially fractionate different parts of a malignant cell population based on their deformability--potentially separating cells by invasiveness ⁶⁰.

The existing systems are not capable of sorting stiff and deformable cells with the same size, while changes of stiffness of single cells is shown to indicate malignancy. However, our system applies large strains on cells, magnifying the effect of cell deformability on its final effective diameter, based on which passive sorting can be more easily achieved. Our system can be fabricated with the simplest standard 2D microfluidic fabrication techniques, which decreases the time and cost of fabrication drastically. The final product will be a separation cartridge that is easy to use. The cartridge is compatible with standard 24-well plates and the sorted fractions of the sample can be easily captured for further analysis. There is no need for any external set-up (including electrodes, optical systems, or cameras) to induce cell separation, as opposed to "active" methods. Our final system will be as simple as possible, merely relying on geometric design and presence of a fluid driving force. This is particularly important in practice since it enhances the reliability of the system, and makes it easy-to-use. As the system is extremely simple (2D design structure, no external forces) and relies solely on geometry of the device and the flow rate, with no extra components involved, it is also very robust. As this system relies on inertial effects in the system, it usually works at relatively high flow rates, which makes it quite

high-throughput, especially compared to DLD and HDF techniques which require particularly low flow rates.

Our approach enables automated processing of large volumes of bodily fluids for rapid label-free isolation of larger deformable cells into a small end volume. The proposed approach uses several recent discoveries in microfluidic automation to yield a low-cost instrument that can improve cytopathology diagnostics and advance targeted drug therapies by providing purified cell populations of interest. The cells are first deformed using deformability cytometry (DC), although other methods of deforming cells may be used in this first step. Single cells in the fluid are aligned into a continuous stream and are consequently stretched by applying large strains (greater than 50%) and strain rates (in kHz range). The ratio of cell deformation under similar force is defined by cell stiffness. The stretched cells are then separated based on their effective diameter (deformed diameter) into a number of outlets. The differences between the deformed diameter of cells are large enough to enable an efficient, continuous passive separation downstream. We believe that this technique not only enables sorting out of malignant cells in pleural effusions, but could potentially fractionate different parts of malignant cell populations based on their deformability. Beyond pleural effusions, stem cells, leukocyte sub-populations, and other cells or particles can be sorted based on mechanical properties for uses in improved diagnostics or research.

Our technique takes both cell size and stiffness into account and enables rapid and selective sorting of cells of interest with high sensitivity and specificity. We achieve this, using inertial focusing of shaped particles and introducing adjustable fluidic resistances which are adjusted to extract the desired cell population fractionation. We first optimize the hydrodynamic forces that result in maximum differences in the deformed cell diameter (equivalent to the rotational

diameter) of malignant cells compared to the background leukocytes. Second, we use inertial focusing to sort cells of different deformed diameter with high purity. Inertial focusing in a straight channel has been previously established for separation of cells and particles based on their size and shape. These studies show that the lateral position of cells in the channel is directly related to its rotational diameter. By tuning channel geometry and flow conditions different fractions segregate within the channel and can be isolated downstream in different outlets.

High-throughput uniform single cell stretching. Inertial focusing is used to focus cells to a 3D position as an alternative to hydrodynamic focusing. Operating in inertial regime (channel Reynolds number $Re \sim 100$) ensures positioning cells to the same streamlines prior to stretching. This ensures that each cell, traveling at the same downstream velocity, experiences equivalent three-dimensional force field at the extensional flow region. Cells are delivered at high rates to an extensional flow, which is used to stretch the cells in suspension to high strains and strain rates that create significant deformations. Cell viscoelastic properties determine to what extent a cell deforms. These large strains (greater than 50%) on the cells, allow for significant differences in cell deformation across cell types. As a first step we use inertial focusing, a sheathless alternative to hydrodynamic focusing, to focus cells to a position in the cross-section of the flow. Inertial focusing ensures positioning of cells to the same streamlines prior to stretching, resulting in uniform velocity, and delivers them to a three-dimensional fluid force field (Fig. 11, Step 2). This extensional, stretching flow exerts large strains on deformable cells. Cell viscoelastic properties determine to what extent a cell deforms. The ability to exert strains as large as 50% of the cell diameter provides a large dynamic range to distinguish between cells by deformability. For example, in preliminary studies, we found that Jurkat cells (a leukemia cell line) possessed a

~2-fold larger deformed diameter than WBCs, while only a 40% increase in resting diameter (before hydrodynamic stretching) was observed. In general, deformed diameter was a better metric than resting diameter for discriminating WBCs from a host of cancer cell types that can be present in pleural fluids (Fig. 13). Importantly, we make use of these larger differences in deformed diameter in our passive separation approach.

Automated easy-to-use processing of samples. The chip can be integrated with a custom-made pressure system that continuously delivers samples from large volume containers in a high-throughput and programmable manner. The instrument will be ‘plug-and-play’, with a few simple steps: (i) obtain the sample from the patient and place it in a pressurized glass bottle, (ii) plug in the chip and (iii) press play on the custom software.

Passive cell sorting based on deformed diameter. Differences in inertial focusing equilibrium positions (position in a channel’s cross-section) based on size have been used extensively to separate cells and particles. Strategic design of the channel geometry including the placement of outlets allows size-based fractionation. Recently the Di Carlo laboratory has shown that for non-spherical particles, separation based on shape is also feasible. These previous studies showed that the equilibrium position of cells in a channel is directly related to its rotational (or longest) diameter. For ellipsoidal deformed cells, the rotational diameter corresponds to the deformed diameter. We have previously reported 90% purification of particles with a two fold difference in their mean rotational diameter (Fig. 15C) suggesting the ability to obtain high purity malignant cells from pleural fluids based on the even larger differences in deformed diameter. The feasibility of this approach is further supported by the observation that deformed cells retain their deformed shape 3-5 mm downstream following initial deformation (Fig. 14).

Alternative sorting method (Dean flow-based sorting). Instead of a 5 mm long straight channel for focusing deformed cells, Dean flow, a secondary flow perpendicular to the primary flow direction induced by channel curvature in inertial flows, can be used to sort cells of different effective diameters within a shorter distance (<1 mm) (Fig. 15B). This secondary flow was previously found to apply a drag force to flowing particles, and alter their position in the presence of other forces (eg. inertial forces) in the channel. The Dean drag scales as $F_D \sim \rho U_m^2 a D_h^2 r^{-1}$ (ρ : fluid density, U_m : maximum channel velocity, a : particle diameter, D_h : hydraulic diameter and r : radius of curvature of channel), where $D_h = 2wh/(w + h)$ (w : channel width, h : channel height). The balance between inertial lift and Dean drag forces determines the equilibrium position of the particles in channels²⁶.

We have successfully shown separation of softer Jurkat cells (median deformed diameter ~27 μm) from stiffer 4% paraformaldehyde fixed Jurkats (median deformed diameter ~17 μm) into two individual streams using Dean flow (Fig. 15D); however, initial purity is not as high as a level as in straight inertial separators.

Depending on the cell size and fractionation of interest, channel geometries and flow rates and configuration of outlet resistances can be optimized. Histograms of particle lateral position in the channel at different conditions (channel size and flow rate) could serve as experimental methods to optimize separation while numerical simulations could provide useful approximations to predict a particle's lateral position.

For the Dean flow implementation, in our experiments we found the device with channel width, $W = 60\mu\text{m}$ and channel height, $H = 30\mu\text{m}$ at $Q = 900\mu\text{L}/\text{min}$ with curved channel of 900 μm inner diameter and 1200 μm outer diameter that has 4 outlets with equal resistances is the best

device to separate softer Jurkat cells (median deformed diameter $\sim 27\ \mu\text{m}$) from stiffer 4% paraformaldehyde fixed Jurkats (median deformed diameter $\sim 17\ \mu\text{m}$) (Fig. 15D).

Discussion

We have demonstrated that the inertial separation of particles with different shapes is possible and tunable with channel geometry and flow conditions. This work is the first of its kind to demonstrate a practical solution to continuously filter particles that have similar dimensions along one axis, but vary along another axis – which cannot be effectively accomplished with traditional filtration. The approach is passive, simple and continuous, using only inertial effects present in simple straight channels. Other advantages are the absence of any external set-up to induce particle separation, as opposed to active methods such as DEP, and increased processing rates compared to DLD and HDF techniques which require particularly low flow rates ($60\ \text{nL/min}$ ²⁹ and $2\text{--}3\ \mu\text{L/min}$ ³⁰ versus our $40\text{--}80\ \mu\text{L/min}$), since the underlying separation force does not increase with flow rate in previous techniques as is the case with inertial separation.

The predictability of inertial focusing of non-spherical particles is of interest to various research areas. There are many arbitrarily shaped particles in biology and industrial processing that are counted and analyzed. As an example, the deviation from spherical symmetry has been recently demonstrated to result in a considerable increase in cytometry uncertainty. The precise alignment of shaped particles by inertial focusing, and especially the predictability of this alignment, would help to address this kind of uncertainty and to produce more reliable measurements⁶¹. One potential application is the fluidic alignment of bar-coded particles. Bar-coded particles are fabricated using approaches like stop-flow lithography and used for

multiplexed and high-throughput biochemical assays. These particles are usually aligned by sheath flow⁷ which can lead to unstable focusing, or active guiding rails which complicate their integration in microsystems. Inertial effects may enable precise control of the alignment and focusing of bar-coded particles for the optical reading of their patterns. Similarly, our results suggest design criteria, since although particles rotate in our channels, maintenance in a relatively fixed orientation for a longer period needed for reading can be achieved by increasing the particle aspect ratio. Another application is the sorting of microalgae prior to cytometry, as phytoplankton possesses a large variety of shapes and sizes^{5,6}. Non-spherical objects rotate and translate vertically in an oscillatory pattern in the channel and depending on their initial angle, these organisms with the same length may pass through the interrogation region at different angles, causing different scatter signals. Shape-based separation prior to interrogation would allow a more effective identification of marine microorganisms in water.

More interestingly, inertial shape-based separation is possible for a large range of particle sizes. The differential focusing of larger non-spherical particles (up to 100 μm) was shown previously³⁹. Focusing of particles as small as 2 μm was also demonstrated in our lab²⁵, while particles smaller than 2 μm require higher flow rates and pressures, necessitating materials with higher bond strengths, such as Thermoset Polyester (TPE)⁶². The possibility of separating 2-3 μm spheres and rods as demonstrated here opens a new range of applications in separation of bacteria to synchronize populations at different stages of cell growth. Depending on the stage of the cell cycle, rod-like bacteria (e.g. bacilli) can up to double their length while maintaining the same short dimension. Enrichment of these bacteria by life-cycle stage can avoid cell-cycle dependent noise, and aid microbiologists in synchronizing a population to better understand population dynamics, environmental effects leading to desynchronization, and stochasticity in

single-cell behavior⁶³. New applications may also be targeted outside of biotechnology in separation of cement microparticles into pure fractions. Cement strength and stability are critically linked to particle shape and size. An approach for filtration of highly defined particles without clog-prone filters would aid in the development of optimized cement formulations - saving material costs for various construction applications.

We have performed numerous experiments with live and fixed cell with a variety of flow conditions and channel geometries in the sorting region. We have assessed the feasibility of deformability-based separation for fixed and live cells. We have previously tested a variety of outlet configurations and identified the critical parameters that can be adjusted for optimal separation.

Our next steps are to further demonstrate this sorting approach with other cells and manufacture the final cartridge for clinical studies.

Gathering data on deformed diameter for model cell lines vs. WBCs over a range of hydrodynamic stresses to identify maximum differences in rotational diameter achievable. With our analytical instrument, the deformability cytometer, we obtained the deformed diameter of many types of cells (including leukocytes, leukemic cell lines, and carcinoma cell lines) using a single operating condition (Fig. 13). In our initial results we were able to obtain up to a 2-fold increase in deformed diameter. Here, we propose to expand the range of hydrodynamic stresses applied to identify conditions leading to maximum differences in deformed diameter between leukocytes, model mesothelial cells, and a panel of cell lines representative of the cancer types that disseminate into pleural effusions. Our goal is to achieve a greater than 3-fold increase in deformed diameter which, based on our initial separation data (Fig. 15C), is expected to bring us above a 40% of malignant cell purity threshold for the majority of pleural effusions which have

initial malignant cell purities that are $>5\%$ ⁶⁴. We expect that additional increases in deformed diameter are achievable with increasing fluid stresses and shear rates, as others have shown shear rate-dependent differences in deformability for malignant cells and healthy cells ⁶⁵.

The hydrodynamic stress applied to single cells at the extensional flow junction relates to the initial fluid velocity prior to reaching the junction. This velocity is a function of channel dimensions as well as the driving volumetric flow rate. We will systematically vary (i) channel width, (ii) channel height and (iii) flow rate to identify conditions that result in maximum differences in the deformed diameter of cell populations of interest. It is possible that higher flow rates will result in larger deformed diameters for both cell populations; however, deformation may also diverge between cell types as larger strains could depend on different cellular properties such as nuclear viscoelasticity vs. cytoplasmic cytoskeletal properties for smaller strains. Measurements of deformed diameter will be taken both at the stretching junction and 5 mm downstream of the junction using our high-speed microscopic setup. We plan to place sorting structures (i.e., outlets) at approximately this distance to account for the potential for cell relaxation as well as provide an adequate length for inertial focusing to occur. The base chip design is 60 μm wide and 30 μm tall at the extensional flow junction with an operating flow rate of 900 $\mu\text{L}/\text{min}$. Channel height will be set to maintain inertial focusing and allow for cells within pleural fluids to pass easily; however, we will evaluate channel widths between 50 and 100 μm , and flow rates from 600-3,000 $\mu\text{L}/\text{min}$. The flow rate should be high enough to operate in the inertial regime, ($10 < Re < 200$). For these studies we will use the panel of cell lines shown in Fig. 12, including lung and breast adenocarcinoma lines along with leukocytes. The mean deformed diameter ratio between the cell lines and leukocytes will be our metric which will be evaluated with a goal of a 3-fold difference to enable pure separations.

Optimizing the design of sorters to maximize separation based on combination of cell size and deformability. The main platform of the resistance-based sorting section is composed of: (i) a simple straight focusing channel, 3-5 mm in length (enough for lateral focusing of cells). We have confirmed that cells retained their deformation 5mm downstream of the deforming region of the device (Fig. 14). (ii) a gradually expanding region, which maintains focused particles in the focusing streamline while enhancing the differences in their equilibrium lateral positions compared to the straight portion. (iii) Several branched outlets with fluidic resistors. Each outlet has a serpentine channel as a fluidic resistor to precisely configure the fraction of the cells that will be collected from each outlet (by tuning the ratio of outlets fluidic resistances, we can collect more or less of a given stream). The serpentine channels also minimize the flow ratio distortion due to small variations in the outlet fluidic resistance caused by possible variation in tubing length or small debris. In order to achieve a specific mode of separation, a) channel width and height, b) the number and c) relative resistance of outlets can be systematically adjusted, providing a variety of relative capture ratios of the fluid at different outlets.

We recently demonstrated our ability to sort particles of different aspect ratios, due to their inertial migration to different lateral positions (equilibrium positions), X_{eq} , in a straight channel. This sorting system (Fig. 15A) is composed of: (i) a straight inertial focusing channel, 3-5 mm in length (enough for inertial lift to lead to focusing of cells)); (ii) a gradually expanding outlet region (2° expansion every 100 μm downstream distance), which maintains focused particles in focusing streamlines while enhancing the differences in their lateral positions compared to a straight expansion³⁷; and (iii) several outlet branches with fluidic resistors. Each outlet has a serpentine channel as a fluidic resistor to precisely configure the fraction of the flow volume (and cells) that will be collected. By tuning the ratio of outlets fluidic resistances, the sorting

fractions can be adjusted. The serpentine channels also minimize the flow ratio distortion due to small variations in the outlet fluidic resistance caused by possible fabrication defects or small debris.

Depending on the final deformed shapes of the cells we will adjust our separation cut-offs with a goal of collecting at least one fraction with greater than 40% purity of malignant cells for pleural effusions with down to 5% initial malignant cell populations. These cut-offs can be adjusted by modifying, a) channel width and height (Fig. 15A, *i*), b) the number and c) the relative resistance of outlets, providing a variety of relative capture ratios of the fluid at different outlets to achieve final chip designs. The cut-off positions will be informed by high-speed imaging of the equilibrium positions of the deformed cells. As shown in Figure 15, we will incorporate 7 outlets at each of the two exit channels downstream of the stretching region in the device. The outlets are symmetric in their resistances, meaning that the sample will be fractionated into 4 distinct populations. The resistances and channel width will be designed such that the middle channel will contain few cells, acting as the waste outlet for the largest fluid volume and leading to concentrated cell populations in the other outlets. In order to increase the flexibility of the separation and achieve additional fractions that may depend on the degree of malignancy, we also plan to arrange the resistances of the two opposite 7-outlet branches differently, keeping the total resistance the same, but leading to different cut-off points for each fraction (Fig. 16B). Importantly, this will result in two different sets of three (or 6 distinct fractions) sample fractions, which can provide flexibility in achieving high purity even when processing unknown pleural fluid samples in future clinical studies.

We will design cartridges for sample loading and cell release in consultation with our clinical collaborators and their staff to obtain user feedback at an early stage and minimize

design iterations and costs. Initial interactions have motivated interfacing with a well-plate format to ultimately improve integration with downstream molecular assays and companion diagnostics (Fig. 16).

Materials and Methods

Microfluidic device fabrication and geometry. Microfluidic devices were fabricated using common polydimethylsiloxane (PDMS) replica molding processes. Briefly, standard lithographic techniques were used to produce a mold from a silicon master spin-coated with SU-8 photoresist. PDMS chips were produced from this mold using Sylgard 184 Elastomer Kit (Dow Corning Corporation) and a cross-linker to polymer ratio of 1:10. To enclose the channels, PDMS and glass were both activated by air plasma (Plasma Cleaner, Harrick Plasma, 500 mTorr, 30 sec) before being bonded together. Our primary device was a straight rectangular channel, 4 cm in length (a distance expected to be long enough for particles to be laterally focused in their dynamic equilibrium positions (X_{eq})⁶⁶), and with a cross-section of 47 μm in depth by 25, 30 or 35 μm width (channel aspect ratios, AR_c , are therefore 0.53, 0.64 and 0.74 respectively).

For particle separation, our SAPS device is composed of (i) the previously described straight focusing channel, (ii) a gradually expanding region downstream of the focusing channel, and (iii) 5 or 7 branched outlets with tuned fluidic resistors (Fig. 10, A-C). Indeed, as previously reported a gradually expanding region maintains focused particles in the focusing streamline while enhancing their X_{eq} differences when compared to straight-angled expansions³⁸. The tuned fluid resistors in the form of serpentine channels minimize the flow ratio distortion due to any small variation in the outlet fluidic resistance (due to small variation in tubing length or small

debris). These serpentine also offer the ability to precisely configure each outlet, by tuning the ratio of outlet fluidic resistances to collect more or less of a given stream. α represents this ratio of outlet flow rates ($\alpha = Q_{O1}/Q_{O2}$), which also represents the ratio of outlet fluidic resistances. For both geometries, filters located at the inlet prevent channel clogging by aggregates.

Bead fabrication and injection. 3 and 6 μm spherical beads (Polyscience) were stretched to rods with different aspect ratios ($R=1:3$ and $1:5$) (Fig. 1), following the protocol published previously by Champion et al.⁶⁷. Beads were suspended in 75°C water - hot-water soluble poly(vinyl alcohol) (PVA) - to a final concentration of 10% wt/vol, 5% wt/vol glycerol, and 0.08% wt/vol spherical polystyrene particles). This solution was spread and dried overnight on a 19 x 27 cm flat surface. The films were then stretched in mineral oil at 120°C on a custom-made apparatus, and dried at room temperature for 20 minutes. To recover the rod-shaped particles, the films were washed with isopropanol and dissolved in 30% isopropanol/water at 75°C. The particles were finally washed 8 times, each time with decreasing amounts of isopropanol, in order to remove all PVA from the particle surface. Particle suspensions were injected into tested devices, at a maximum concentration of 1×10^6 beads/mL, using a syringe pump (Harvard Apparatus PHD 2000) and a glass syringe (Hamilton), at flow rates Q ranging from 20 to 110 $\mu\text{L}/\text{min}$.

High-speed imaging for study of inertial focusing and particle motion. Image sequences were recorded 4 cm away from the inlet using a Phantom v7.3 high-speed camera and the Phantom Camera Control Software (Vision Research Inc.). Based on these images and using a MATLAB custom-built code, the size and center of individual particles were determined in each image frame to estimate the average particle equilibrium position (X_{eq}). Particle motion in

channels with 0.64 and 0.74 aspect ratios was also studied through high-speed images, to determine and characterize the modes of particle rotation.

The particle average equilibrium position (X_{eq}) was calculated by measuring the distance between the particle center and the channel wall. X_{eq} equal to 0% or 50% indicates that the particle center is located at the channel wall or the channel center respectively. To obtain statistical significance, more than 100 data points were measured for each particle type and flow conditions, with less than 1% error for each point due to the resolution of the camera. A *Separability Factor* ($SF_{Type1-Type2}$) was calculated as the difference in average focusing positions (X_{eq}) between two particle shapes, normalized by the average of their standard deviations (Fig. 6, Equation 1), and indicated the expected separation performance

By analyzing high-speed images, the dominant modes of rotation were also determined at the end of the channel (Fig. 2A). The observation frequency of each of these modes for $AR_c = 0.74$ channel is reported at different flow rates (Fig. 2B). The period of the rotation, $T(\mu s)$, was calculated by counting the number of frames required for a particle to make a half rotation. The number of frames for a half period was converted to microseconds simply using the frame rate of the image sequence and then multiplied by 2 to give the period of a full rotation.

Simulations. Two methods of simulation were used to calculate equilibrium positions for shaped particles. **(1)** To simulate steady-state focusing positions, we used a numerical model that solves the 3D incompressible Navier-Stokes equations in the reference frame of a spinning particle^{55,68}. For these simulations, while the position of the particle is fixed, the dynamics of the system are updated to achieve force- and torque-free conditions for the particle (i.e. the steady-state behavior). Using this method, we conducted a series of simulations for various particle

positions along the short axis of the channel (at $z=0$) which yielded the steady state lateral force for a particle held to each particular position. Because the rotation rate of the particle is updated as a slip condition on the particle surface, only particles rotationally symmetric about the vorticity axis of the flow (e.g. spherical particles, and ellipsoids rotating around their rotationally symmetric axis) can be accurately simulated. Therefore, for ellipsoid particles with 1:3 and 1:5 dimension ratios that are experimentally observed to prefer a “tumbling” motion, we could only simulate horizontally-aligned positions with no rotation. For both spherical and ellipsoid particles the position where the lateral force curve crossed zero was interpolated to find the dynamic equilibrium position. Simulations for non-spherical particles (aspect ratios 1:3 and 1:5) were conducted (i) assuming that particles are rods but do not rotate in the channel (*Aligned rods*), (ii) assuming that particles are spheres with their small dimension (b) as the diameter of the sphere (*Spheres $D=b$*) or (iii) assuming that particles are spheres with their large dimension (a) as the diameter of sphere (*Spheres $D=a$*). **(2)** To predict the particle focusing position of non-spherical particles for the more accurate case of (iv) taking their rotation into account (*Rotating rods*) and to simulate the dynamics and direction of particle rotation, we used a fully-coupled hybrid computational approach that integrates the lattice Boltzmann model (LBM) for the dynamics of the fluid and the lattice spring model for the motion of rigid ellipsoidal particles²⁰. The LBM is a lattice-based numerical method for simulating hydrodynamic flows governed by the incompressible Navier- Stokes equations^{69,70}. The flow is modeled by simulating the time evolution of a density distribution function, $f_i(\mathbf{r}, t)$, that describes the mass density of “fluid particles” with velocity \mathbf{c}_i at a lattice node \mathbf{r} at time t . We use a three-dimensional D3Q19 model with 19 velocities⁶⁹. The time evolution of the distribution function is governed by the discretized Boltzmann equation, $f_i(\mathbf{r} + \mathbf{c}_i \Delta t, t + \Delta t) = f_i(\mathbf{r}, t) + \Omega[f(\mathbf{r}, t)]$. The collision operator

$\Omega[f(\mathbf{r},t)]$ accounts for the change in f_i due to instantaneous collisions at the lattice nodes. The flow parameters are calculated as follows: the fluid density $\rho = \sum_i f_i$, the momentum $\mathbf{j} = \rho \mathbf{u} = \sum_i f_i \mathbf{c}_i$, where \mathbf{u} is the macroscopic fluid velocity, and the stresses $\Pi = \sum_i f_i \mathbf{c}_i \mathbf{c}_i$. The solid particles are modeled by a set of lattice nodes located on the outer particle surface and connected by rigid bonds¹⁸. In this representation, we simulate particles as thin solid shells filled with a viscous fluid. We verified that for a low frequency particle rotation observed in our simulations, the viscous fluid inside particles behaves as a solid and the particles follow the rigid body dynamics. Thus, the total particle mass combines the contributions due to the shell and the internal fluid⁷⁰. To capture the dynamics of the particle motion, we calculate the total force and torque on the solid particles due to the fluid and find the translational and rotational displacement of the particle by integrating Newton's equation of motions. We, then, update the positions of lattice nodes on the particle surface.

The lattice models for fluid and solid are coupled through appropriate boundary conditions. Specifically, we use an interpolated bounce-back scheme at the moving solid-fluid interface that provides second-order accuracy^{71,72}. We have previously validated our hybrid model in the limit of low Reynolds numbers and used it to examine microchannel flows with rigid and compliant particles^{18–22,73,74}. In order to compare the simulations with experimental results, we set the dimensions of channel, particle size and Reynolds number equal to the corresponding experimental parameters. At the beginning of the simulations, the particles are released at different positions and their trajectories are monitored. For a given set of flow parameters, particles released at different initial positions migrate to a common equilibrium trajectory. The equilibrium trajectory exhibits oscillations due to the periodic rotation of particles. By averaging

the trajectories over one oscillation period, we find the mean equilibrium positions of particles. The equilibrium orientations of the particles were also predicted through the experiments (Supplementary info).

Experiments and analysis for shape-based separation of beads. For separation experiments, a mixture of spheres, rods of 1:3 and 1:5 aspect ratios was prepared and injected into a SAPS device to evaluate the separation of different particles from each other. Several flow rates and fluidic resistances were tested to maximize the separation, and the fractions of different particles collected from each outlet for each of these tested conditions were measured. Separation can be characterized using 3 parameters, defined below for a particle type a and an outlet i (Equation 2). The *Extraction Yield* (EY) is determined as the number of particle a extracted in the outlet i , over the total number of this particle type injected; EY reports the outlet collection efficiency of a given particle type. The *Extraction Purity* (EP) considers the proportion of particle type a in outlet i , relative to the total number of beads extracted in this outlet; EP reports the particle composition of a given outlet. The *Enrichment Ratio* (ER) is defined as the proportion of particle a in outlet i to its proportion at the inlet.

$$EY = \frac{N_a(\text{outlet}_i)}{N_a(\text{inlet})} \quad EP = \frac{N_a(\text{outlet}_i)}{N_{\text{tot}}(\text{outlet}_i)} \quad ER = \frac{N_a(\text{outlet}_i) / N_{\text{tot}}(\text{outlet}_i)}{N_a(\text{inlet}) / N_{\text{tot}}(\text{inlet})} \quad (2)$$

Application to shape-based separation of yeast. Yeast was cultured in Tryptic Soy Broth (TSB) in an incubated shaker (37°C) for one day prior to the separation experiment. The cultured suspension was diluted in PBS at a non-limiting concentration of 1.5×10^6 cells/mL and then, similarly to beads, was injected at various flow rates using a Harvard Apparatus syringe pump and Hamilton glass syringe. The separation behavior was captured through high-speed imaging,

with the content of each outlet being analyzed by immediate counting with a hemocytometer (Quick-Read). The morphologies of yeast cells were observed and categorized, depending on their cycle state, into (i) small non-dividing singles, (ii) large singles, (iii) budded yeast, (iv) doublets, and (v) aggregates which are composed of three cells or more.

Particle orientation. Our simulation shows two possible equilibrium orientations for the particles in channels. One is in the x - y plane (tumbling mode), the other is perpendicular to the x - y plane (rolling mode). In the tumbling mode the equilibrium position is closer to the channel center compared to rolling mode where the equilibrium position is close to the channel wall. Based on more simulations, we find that initial orientation, channel width and aspect ratio of particle would all affect the final orientation. For instance we have chosen random initial orientations for particles with two different aspect ratios in channels with $ARc=0.35$, 0.64 and 0.74 (Fig.3). In A and B, $W = 25$ ($ARc=0.35$), $Re = 37$, two particles have the same initial orientation $(0.866, 0, -0.5)$, as shown in the figures. Red line denotes trajectory of tip of particle $(X_{tip}, Y_{tip}, Z_{tip})$ with aspect ratio 1:5, and blue line denotes aspect ratio 1:3. The trajectory shows the motion of ellipsoidal tip with respect to the center of mass (X_{CG}, Y_{CG}, Z_{CG}) . The blue line will equilibrate into a repeating circle at $z = 0$, so final orientation of particle of aspect ratio 1:3 is in the x - y plane without z component (tumbling mode), while final orientation of particle of aspect ratio 1:5 is $(0, 0, 1)$, which is perpendicular to the x - y . In C and D, $W = 30$ ($ARc=0.64$), $Re = 27$, initial orientation is $(0.866, 0, -0.5)$. Both particles have the same final orientation in the x - y plane. In Fig. 3E and F, $W = 35$ ($ARc=0.74$), $Re = 71$, initial orientation is $(0.866, 0.433, 0.25)$ and the final orientation of particles is in x - y plane ($z = 0$). We also noticed that if z component of initial orientation (P_z) is not very close to the 1, particle has large chance to set itself in the x - y plane. However, if channel is narrow or aspect ratio of particle is large,

particles have a large chance to set themselves perpendicular to the x-y plane. Although these simulations give more insight about the behavior of a particle in inertial flow, more independent simulations are needed to do a proper statistical analysis and draw clear conclusions on the most probable final orientation of a particle.

Bibliography

1. Mitragotri, S. & Lahann, J. Physical approaches to biomaterial design. *Nat. Mater.* **8**, 15–23 (2009).
2. Martin, S. G. Geometric control of the cell cycle. *Cell Cycle* **8**, 3643–3647 (2009).
3. Wongsrichanalai, C., Barcus, M. J., Muth, S., Sutamihardja, A. & Wernsdorfer, W. H. A review of malaria diagnostic tools: microscopy and rapid diagnostic test (RDT). *Am. J. Trop. Med. Hyg.* **77**, 119–127 (2007).
4. Piagnerelli, M. *et al.* Assessment of erythrocyte shape by flow cytometry techniques. *J. Clin. Pathol.* **60**, 549–554 (2007).
5. Hashemi, N., Erickson, J. S., Golden, J. P. & Ligler, F. S. Optofluidic characterization of marine algae using a microflow cytometer. *Biomicrofluidics* **5**, 32009 (2011).
6. Hashemi, N., Erickson, J. S., Golden, J. P., Jackson, K. M. & Ligler, F. S. Microflow Cytometer for optical analysis of phytoplankton. *Biosens. Bioelectron.* **26**, 4263–4269 (2011).
7. Pregibon, D. C., Toner, M. & Doyle, P. S. Multifunctional encoded particles for high-throughput biomolecule analysis. *Science (80-.)*. **315**, 1393–1396 (2007).
8. Chung, S. E., Park, W., Shin, S., Lee, S. A. & Kwon, S. Guided and fluidic self-assembly of microstructures using railed microfluidic channels. *Nat. Mater.* **7**, 581–587 (2008).
9. Kersaudy-Kerhoas, M., Dhariwal, R. & Desmulliez, M. P. Y. Recent advances in microparticle continuous separation. *IET Nanobiotechnology* **2**, 1–13 (2008).
10. Inglis, D. W., Riehn, R., Austin, R. H. & Sturm, J. C. Continuous microfluidic immunomagnetic cell separation. *Appl. Phys. Lett.* **85**, 5093–5095 (2004).
11. Pamme, N. Magnetism and microfluidics. *Lab Chip* **6**, 24–38 (2006).
12. MacDonald, M. P., Spalding, G. C. & Dholakia, K. Microfluidic sorting in an optical lattice. *Nature* **426**, 421–424 (2003).
13. Laurell, T., Petersson, F. & Nilsson, A. Chip integrated strategies for acoustic separation and manipulation of cells and particles. *Chem. Soc. Rev.* **36**, 492–506 (2007).
14. Ji, H. M. *et al.* Silicon-based microfilters for whole blood cell separation. *Biomed. Microdevices* **10**, 251–257 (2008).

15. Takagi, J., Yamada, M., Yasuda, M. & Seki, M. Continuous particle separation in a microchannel having asymmetrically arranged multiple branches. *Lab Chip* **5**, 778–784 (2005).
16. Yamada, M. & Seki, M. Hydrodynamic filtration for on-chip particle concentration and classification utilizing microfluidics. *Lab Chip* **5**, 1233–1239 (2005).
17. Choi, S. & Park, J.-K. Continuous hydrophoretic separation and sizing of microparticles using slanted obstacles in a microchannel. *Lab Chip* **7**, 890–7 (2007).
18. Alexeev, A., Verberg, R. & Balazs, A. C. Patterned surfaces segregate compliant microcapsules. *Langmuir* **23**, 983–987 (2007).
19. Smith, K. A., Alexeev, A., Verberg, R. & Balazs, A. C. Designing a simple ratcheting system to sort microcapsules by mechanical properties. *Langmuir* **22**, 6739–6742 (2006).
20. Alexeev, A., Verberg, R. & Balazs, A. C. Motion of compliant capsules on corrugated surfaces: A means of sorting by mechanical properties. *J. Polym. Sci. Part B Polym. Phys.* **44**, 2667–2678 (2006).
21. Arata, J. P. & Alexeev, A. Designing microfluidic channel that separates elastic particles upon stiffness. *Soft Matter* **5**, 2721–2724 (2009).
22. Mao, W. & Alexeev, A. Hydrodynamic sorting of microparticles by size in ridged microchannels. *Phys. Fluids* **23**, 51704 (2011).
23. Huang, L. R., Cox, E. C., Austin, R. H. & Sturm, J. C. Continuous particle separation through deterministic lateral displacement. *Science (80-.)*. **304**, 987–990 (2004).
24. Ookawara, S., Higashi, R., Street, D. & Ogawa, K. Feasibility study on concentration of slurry and classification of contained particles by microchannel. *Chem. Eng. J.* **101**, 171–178 (2004).
25. Gossett, D. R. & Carlo, D. Di. Particle focusing mechanisms in curving confined flows. *Anal. Chem.* **81**, 8459–8465 (2009).
26. Di Carlo, D., Irimia, D., Tompkins, R. G. & Toner, M. Continuous inertial focusing, ordering, and separation of particles in microchannels. *Proc. Natl. Acad. Sci. U. S. A.* **104**, 18892–7 (2007).
27. Beech, J. P., Holm, S. H., Adolfsson, K. & Tegenfeldt, J. O. Sorting cells by size, shape and deformability. *Lab Chip* **12**, 1048–1051 (2012).
28. Holm, S. H., Beech, J. P., Barrett, M. P. & Tegenfeldt, J. O. Separation of parasites from human blood using deterministic lateral displacement. *Lab Chip* **11**, 1326–1332 (2011).

29. Sugaya, S., Yamada, M. & Seki, M. Observation of nonspherical particle behaviors for continuous shape-based separation using hydrodynamic filtration. *Biomicrofluidics* **5**, 24103 (2011).
30. Valero, A. *et al.* Tracking and synchronization of the yeast cell cycle using dielectrophoretic opacity. *Lab Chip* **11**, 1754–1760 (2011).
31. Segre, G. Radial particle displacements in Poiseuille flow of suspensions. *Nature* **189**, 209–210 (1961).
32. Di Carlo, D., Edd, J. F., Irimia, D., Tompkins, R. G. & Toner, M. Equilibrium separation and filtration of particles using differential inertial focusing. *Anal. Chem.* **80**, 2204–2211 (2008).
33. Di Carlo, D. Inertial microfluidics. *Lab Chip* **9**, 3038–3046 (2009).
34. Bhagat, A. A. S., Kuntaegowdanahalli, S. S. & Papautsky, I. Continuous particle separation in spiral microchannels using Dean flows and differential migration. *Lab Chip* **8**, 1906–14 (2008).
35. Hur, S. C., Tse, H. T. K. & Di Carlo, D. Sheathless inertial cell ordering for extreme throughput flow cytometry. *Lab Chip* **10**, 274–280 (2010).
36. Mach, A. J., Kim, J. H., Arshi, A., Hur, S. C. & Di Carlo, D. Automated cellular sample preparation using a Centrifuge-on-a-Chip. *Lab Chip* **11**, 2827–2834 (2011).
37. Hur, S. C., Henderson-MacLennan, N. K., McCabe, E. R. B. & Di Carlo, D. Deformability-based cell classification and enrichment using inertial microfluidics. *Lab Chip* **11**, 912–920 (2011).
38. Hur, S. C., Choi, S.-E., Kwon, S. & Carlo, D. Di. Inertial focusing of non-spherical microparticles. *Appl. Phys. Lett.* **99**, 44101 (2011).
39. Bretherton, F. P., Carrier, G. F. & Longuet-Higgins, M. S. Report on the IUTAM symposium on rotating fluid systems. *J. Fluid Mech.* **26**, 393–410 (1966).
40. Boldrini, L. *et al.* Mutational analysis in cytological specimens of advanced lung adenocarcinoma: a sensitive method for molecular diagnosis. *J. Thorac. Oncol. Off. Publ. Int. Assoc. Study Lung Cancer* **2**, 1086–1090 (2007).
41. Malapelle, U. *et al.* EGFR and KRAS mutations detection on lung cancer liquid-based cytology: a pilot study. *J. Clin. Pathol.* **65**, 87–91 (2012).
42. Lynch, T. J. *et al.* Activating mutations in the epidermal growth factor receptor underlying responsiveness of non-small-cell lung cancer to gefitinib. *N. Engl. J. Med.* **350**, 2129–2139 (2004).

43. Higgins, M. J. & Baselga, J. Targeted therapies for breast cancer. *J. Clin. Invest.* **121**, 3797–3803 (2011).
44. Cervantes, F. & Mauro, M. Practical management of patients with chronic myeloid leukemia. *Cancer* **117**, 4343–4354 (2011).
45. Jian, G. *et al.* Prediction of epidermal growth factor receptor mutations in the plasma/pleural effusion to efficacy of gefitinib treatment in advanced non-small cell lung cancer. *J. Cancer Res. Clin. Oncol.* **136**, 1341–1347 (2010).
46. Smouse, J. H. *et al.* EGFR mutations are detected comparably in cytologic and surgical pathology specimens of nonsmall cell lung cancer. *Cancer* **117**, 67–72 (2009).
47. Billah, S. *et al.* EGFR and KRAS mutations in lung carcinoma: molecular testing by using cytology specimens. *Cancer Cytopathol.* **119**, 111–117 (2011).
48. Gossett, D. R. *et al.* Hydrodynamic stretching of single cells for large population mechanical phenotyping. *Proc. Natl. Acad. Sci.* **109**, 7630–5 (2012).
49. Yang, S., Kim, J. Y., Lee, S. J., Lee, S. S. & Kim, J. M. Sheathless elasto-inertial particle focusing and continuous separation in a straight rectangular microchannel. *Lab Chip* **11**, 266–273 (2011).
50. Jeffery, G. B. The motion of ellipsoidal particles immersed in a viscous fluid. *Proc. R. Soc. London. Ser. A, Contain. Pap. a Math. Phys. Character* **102**, 161–179 (1922).
51. Pozrikidis, C. Orbiting motion of a freely suspended spheroid near a plane wall. *J. Fluid Mech.* **541**, 105–114 (2005).
52. Keller, S. R. & Skalak, R. Motion of a tank-treading ellipsoidal particle in a shear flow. *J. Fluid Mech.* **120**, 27–47 (1982).
53. Koch, D. L. & Hill, R. J. Inertial effects in suspension and porous-media flows. *Annu. Rev. Fluid Mech.* **33**, 619–647 (2001).
54. Subramanian, G. & Koch, D. L. Centrifugal forces alter streamline topology and greatly enhance the rate of heat and mass transfer from neutrally buoyant particles to a shear flow. *Phys. Rev. Lett.* **96**, 134503 (2006).
55. Di Carlo, D., Edd, J. F., Humphry, K. J., Stone, H. A. & Toner, M. Particle segregation and dynamics in confined flows. *Phys. Rev. Lett.* **102**, 94503 (2009).
56. Petranovic, D. & Vemuri, G. N. Impact of yeast systems biology on industrial biotechnology. *J. Biotechnol.* **144**, 204–211 (2009).

57. Walker, G. M. Synchronization of yeast cell populations. *Methods Cell Sci.* **21**, 87–93 (1999).
58. Shedden, K. & Cooper, S. Analysis of cell-cycle gene expression in *Saccharomyces cerevisiae* using microarrays and multiple synchronization methods. *Nucleic Acids Res.* **30**, 2920–2929 (2002).
59. Masaeli, M. *et al.* Continuous Inertial Focusing and Separation of Particles by Shape. *Phys. Rev. X* **2**, 31017 (2012).
60. Suresh, S. Biomechanics and biophysics of cancer cells. *Acta Biomater.* **3**, 413–438 (2007).
61. Spencer, D. & Morgan, H. Positional dependence of particles in microfluidic impedance cytometry. *Lab Chip* **11**, 1234–1239 (2011).
62. Sollier, E., Murray, C., Maoddi, P. & Di Carlo, D. Rapid prototyping polymers for microfluidic devices and high pressure injections. *Lab Chip* **11**, 3752–3765 (2011).
63. Elowitz, M. B., Levine, A. J., Siggia, E. D. & Swain, P. S. Stochastic gene expression in a single cell. *Science (80-.).* **297**, 1183–1186 (2002).
64. Ozkumur, E. *et al.* Inertial focusing for tumor antigen-dependent and -independent sorting of rare circulating tumor cells. *Sci. Transl. Med.* **5**, 179ra47 (2013).
65. Hoffman, B. D. & Crocker, J. C. Cell mechanics: dissecting the physical responses of cells to force. *Annu. Rev. Biomed. Eng.* **11**, 259–288 (2009).
66. Bhagat, A. A. S., Kuntaegowdanahalli, S. S. & Papautsky, I. Inertial microfluidics for continuous particle filtration and extraction. *Microfluid. Nanofluidics* **7**, 217–226 (2009).
67. Champion, J. A. & Mitragotri, S. Role of target geometry in phagocytosis. *Proc. Natl. Acad. Sci. U. S. A.* **103**, 4930–4934 (2006).
68. Lee, W., Amini, H., Stone, H. A. & Di Carlo, D. Dynamic self-assembly and control of microfluidic particle crystals. *Proc. Natl. Acad. Sci.* **107**, 22413–22418 (2010).
69. Succi, S. *The lattice Boltzmann equation: for fluid dynamics and beyond.* (Oxford university press, 2001).
70. Ladd, A. J. C. & Verberg, R. Lattice-Boltzmann simulations of particle-fluid suspensions. *J. Stat. Phys.* **104**, 1191–1251 (2001).
71. Alexeev, A., Verberg, R. & Balazs, A. C. Modeling the motion of microcapsules on compliant polymeric surfaces. *Macromolecules* **38**, 10244–10260 (2005).

- 72. Bouzidi, M., Firdaouss, M. & Lallemand, P. Momentum transfer of a Boltzmann-lattice fluid with boundaries. *Phys. Fluids* **13**, 3452 (2001).
- 73. Masoud, H. & Alexeev, A. Modeling magnetic microcapsules that crawl in microchannels. *Soft Matter* **6**, 794–799 (2010).
- 74. Kilimnik, A., Mao, W. & Alexeev, A. Inertial migration of deformable capsules in channel flow. *Phys. Fluids* **23**, 123302 (2011).

Figures

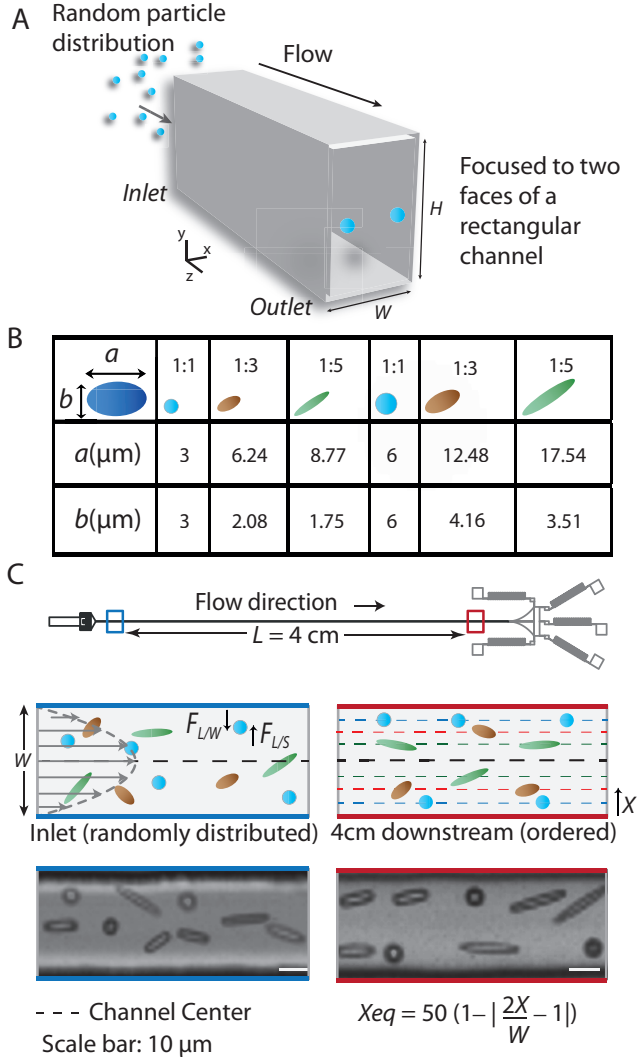


Figure 1. Focusing of ellipsoids of different aspect ratios to two sets of dynamic equilibrium positions. (A) In rectangular channels with a high-aspect ratio, at moderate Re , randomly distributed particles are known to focus to two equilibrium regions centered at the long faces of the channels. (B) The particle shapes, stretching ratios, and ellipsoid dimensions evaluated in the current work. (C) The microfluidic device used for shape-based separation consists of a simple straight 4 cm long channel, with $W=25, 30$ or $35 \mu\text{m}$, and $H=47 \mu\text{m}$. At the inlet (left), particles

are initially randomly distributed within the fluid. Equilibrium positions (X_{eq}) are measured at the channel outlet (right), 4 cm downstream of the inlet, where particles are assumed to be inertially focused due to the combined effect of FL/W (wall effect lift) and FL/S (shear gradient lift). Overlaid pictures (scale bar = 10 μm) illustrate particle distribution, respectively at the inlet (right) and outlet (left). The images are multiple overlays of frames captured at the channel inlet and outlet.

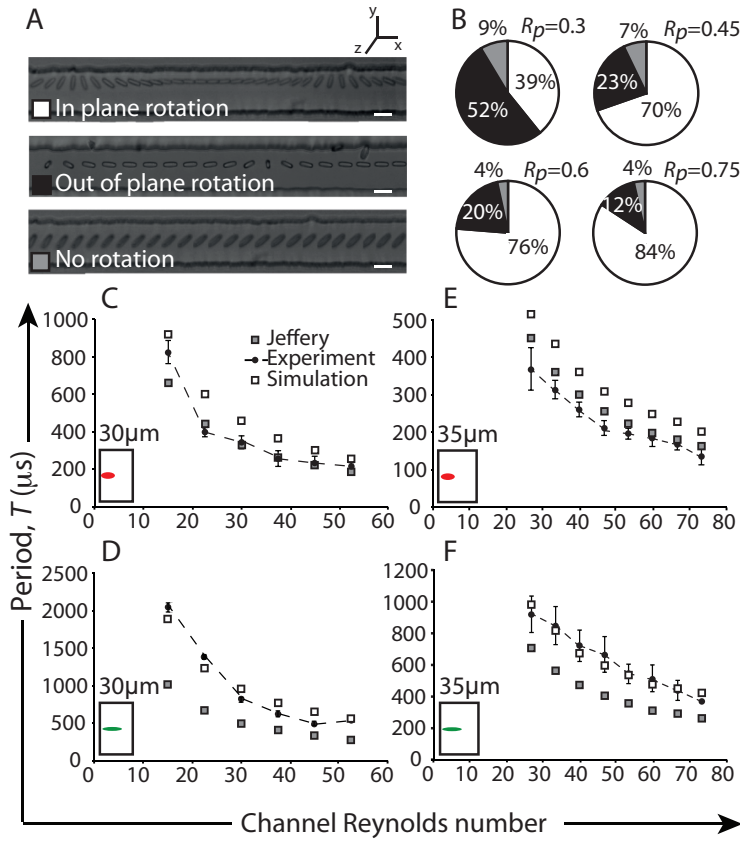


Figure 2. Rotational motion of ellipsoid particles in a microchannel. (A) Three modes of motion of 1:5 rods were observed in a channel with aspect ratio (ARc) of 0.74: “in plane rotation”, “out of plane rotation” and “no rotation”. (B) As R_p (calculated for a sphere of the same volume) was increased from 0.3 to 0.75, the frequency of “out of plane rotation” and “no rotation” modes

decreased and most of the particles rotated in plane around the vorticity axis (color legend shown in A). The period of rotation from our simulation and the Jeffery formula are plotted along with the experimental results for 1:3 (C, E) and 1:5 (D, F) rods in $ARc=0.64$ (C, D) and 0.74 (E, F). Scale bars: $20\text{ }\mu\text{m}$. (G) Period of rotation (T) normalized by average shear rate, increases as the particles get closer to the channel centerline either due to an increase in particle length or decrease in channel width. The normalized value of period is calculated by $T*U_{avg}/(W/2)$ where T is the period of rotation, U_{avg} is the average fluid velocity and W is channel width.

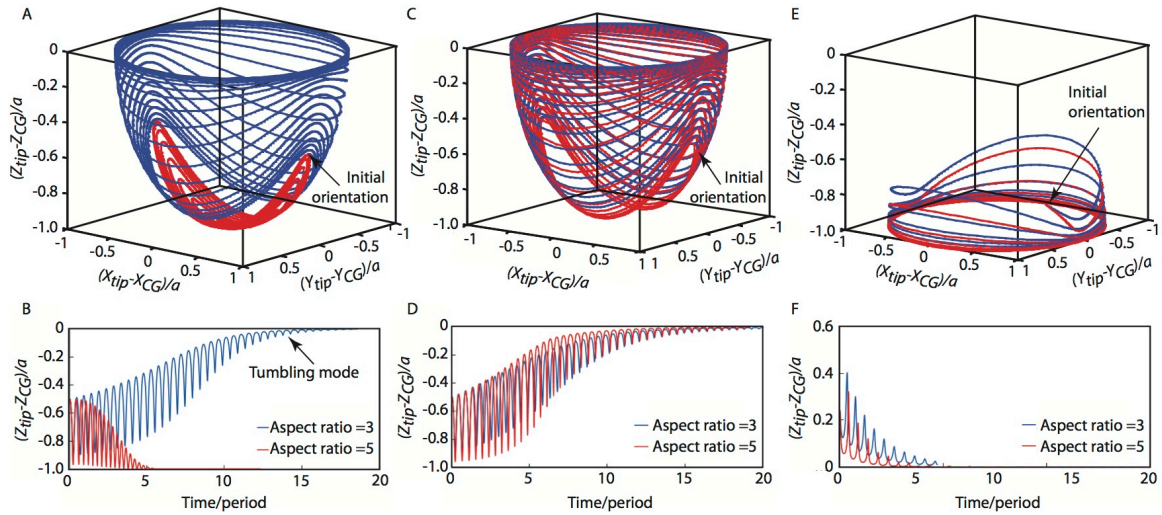


Figure 3. The trajectory of the ellipsoidal tip (X_{tip} , Y_{tip} , Z_{tip}) for particles with aspect ratio 1:3 (blue) and 1:5 (red) with respect to the center of mass (X_{CG} , Y_{CG} , Z_{CG}). Random initial orientations were chosen to predict the final orientation in $ARc=0.35$ (A, B), $ARc=0.64$ (C, D) and $ARc=0.74$ (E, F).

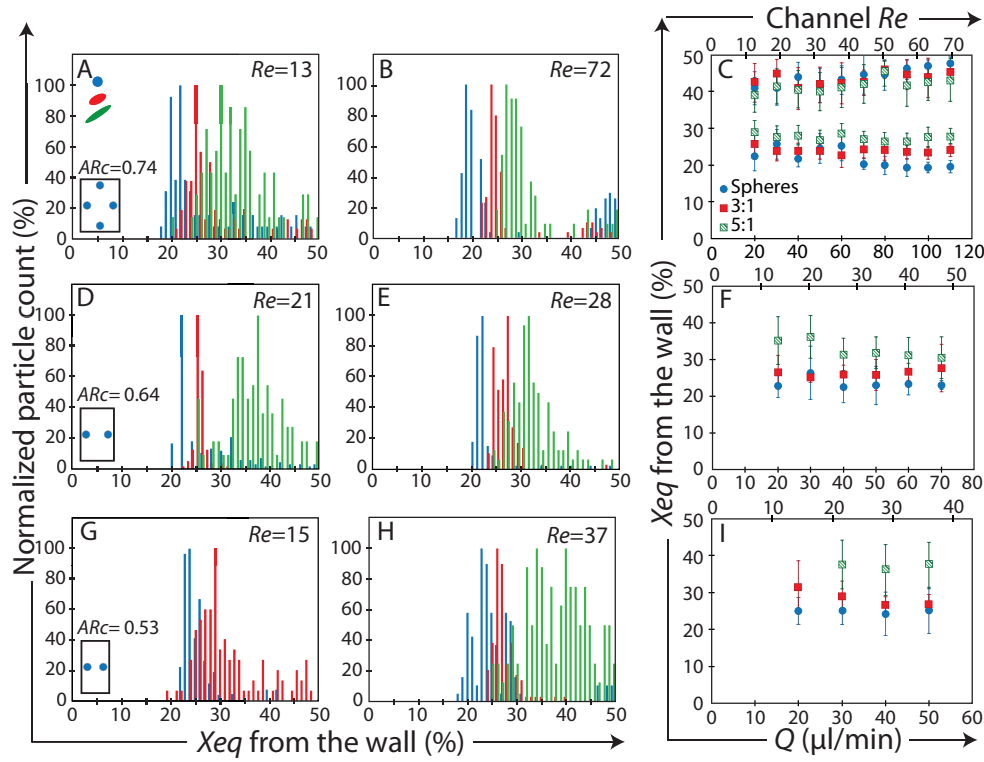


Figure 4. Focusing distributions depend on particle shape, channel aspect ratio, and the Reynolds number of the flow. (A, B, D, E, G, H) Histograms of Xeq for spheres, 1:3 rods and 1:5 rods, in different channel cross-sections and at different flow rates, indicate that equilibrium positions vary for different shapes: (A, B) ARc = 0.74, Q = 20 and 110 μL/min, (D, E) ARc = 0.64, Q = 30 and 40 μL/min, (G, H) ARc = 0.53, Q = 20 and 50 μL/min. (C, F, I) Averaged Xeq is plotted for all channel geometries and flow conditions tested, with error bars indicating the standard deviation obtained from at least 100 measurements.

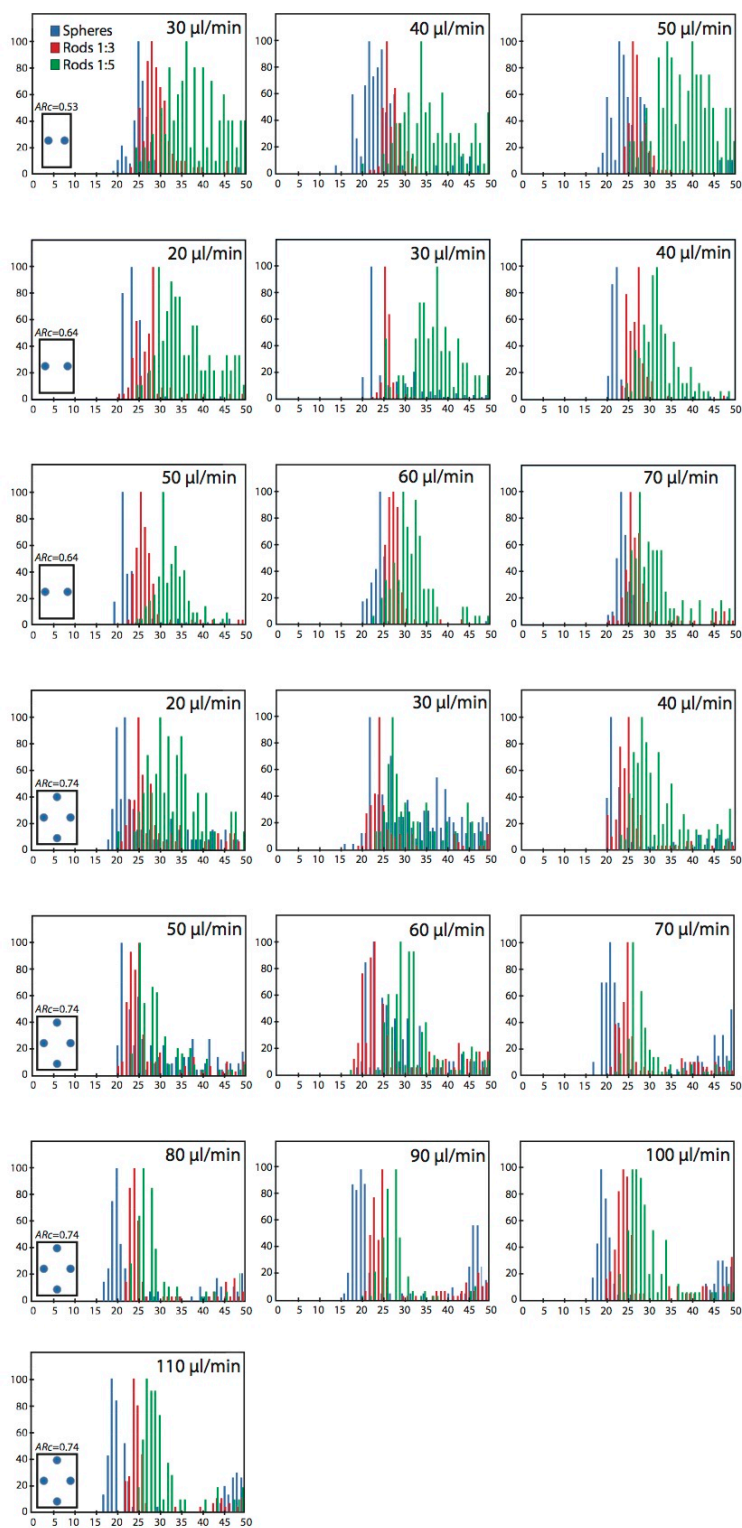


Figure 5. Detailed survey of X_{eq} for spheres, 1:3 rods and 1:5 rods, in channel cross-sections ($W=25, 30$ and $35 \mu\text{m}$) and at flow rates, ranging from 20 to 110 $\mu\text{L}/\text{min}$. Flow rate and channel cross-section greatly influence the average equilibrium position of shaped particles

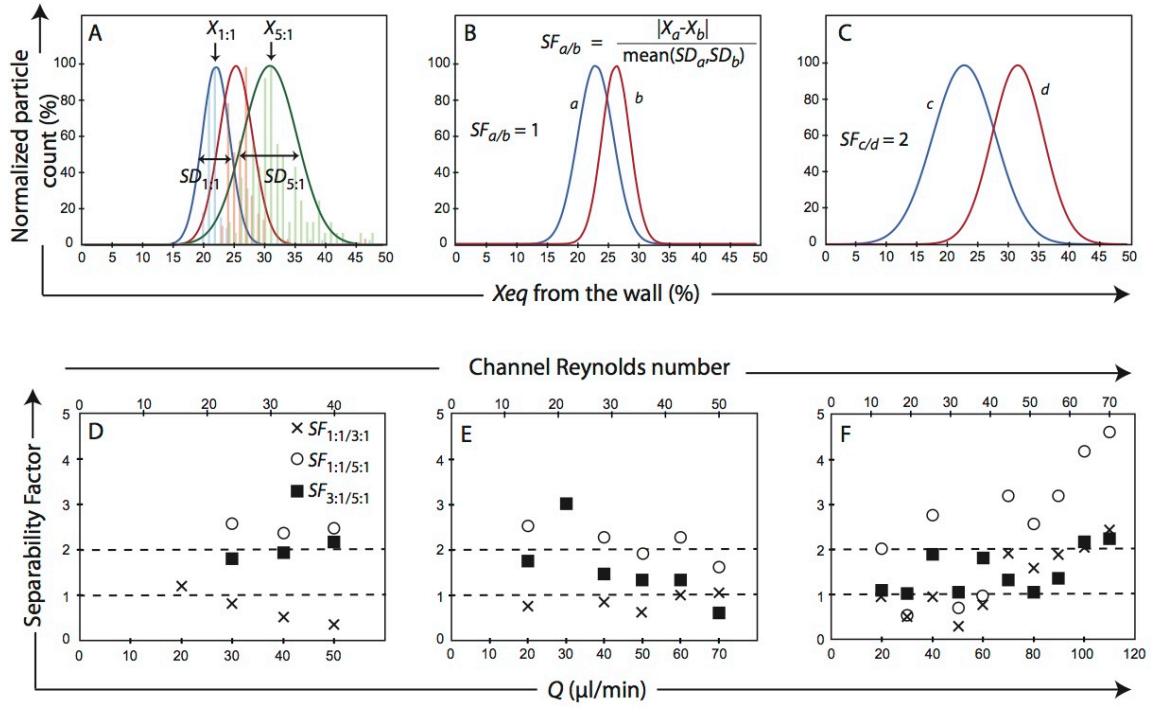


Figure 6. Demonstration of shape-based separability by inertial focusing. (A, B, C) To better interpret the results in view of separation applications, we defined a *Separability Factor* for every two particle types as the difference between their average focusing position divided by the pooled standard deviation of each type. We represented how a Gaussian fit to two frequency plots would look like when the *Separability Factor* is 1 (B) and 2 (C) respectively. (D, E, F) *Separability Factor* obtained for 25 (D), 30 (E) and 35 μm (F) wide channels, at various flow rates.

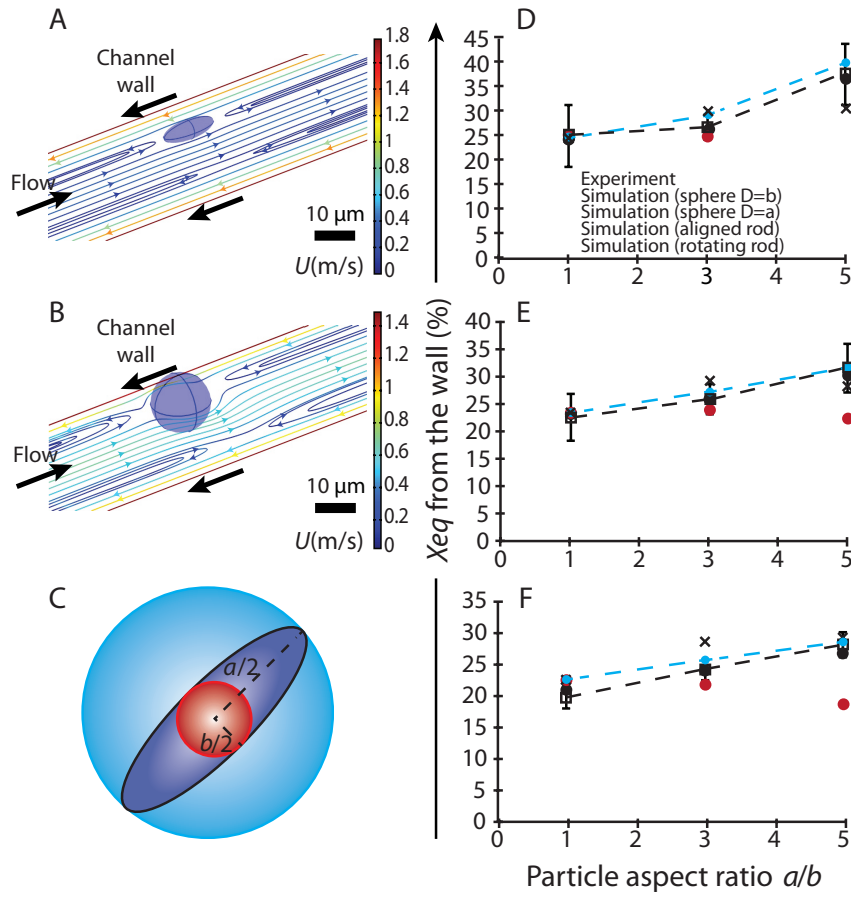


Figure 7. Simulations allow accurate prediction of focusing positions for shaped particles. (A, B) Simulation result and streamlines for flow in the reference frame of a focused rod (A) and spherical (B) particle in a straight channel. (C) Simulations are performed considering particle shape and aspect ratio with (i) the particle rotating (rotating rods), (ii) constraining the rod from rotation (aligned rods), and also considering spheres with diameters corresponding to the rods' (iii) longest (Spheres $D=b$) and (iv) smallest (Spheres $D=a$) dimension. (D, E, F) Comparison of equilibrium positions away from the wall, obtained by experiments and numerical simulations, for (D) $ARc = 0.53$, $Q = 50 \mu\text{L/min}$, (E) $ARc = 0.64$, $Q = 40 \mu\text{L/min}$ and (F) $ARc = 0.74$, $Q = 110 \mu\text{L/min}$.

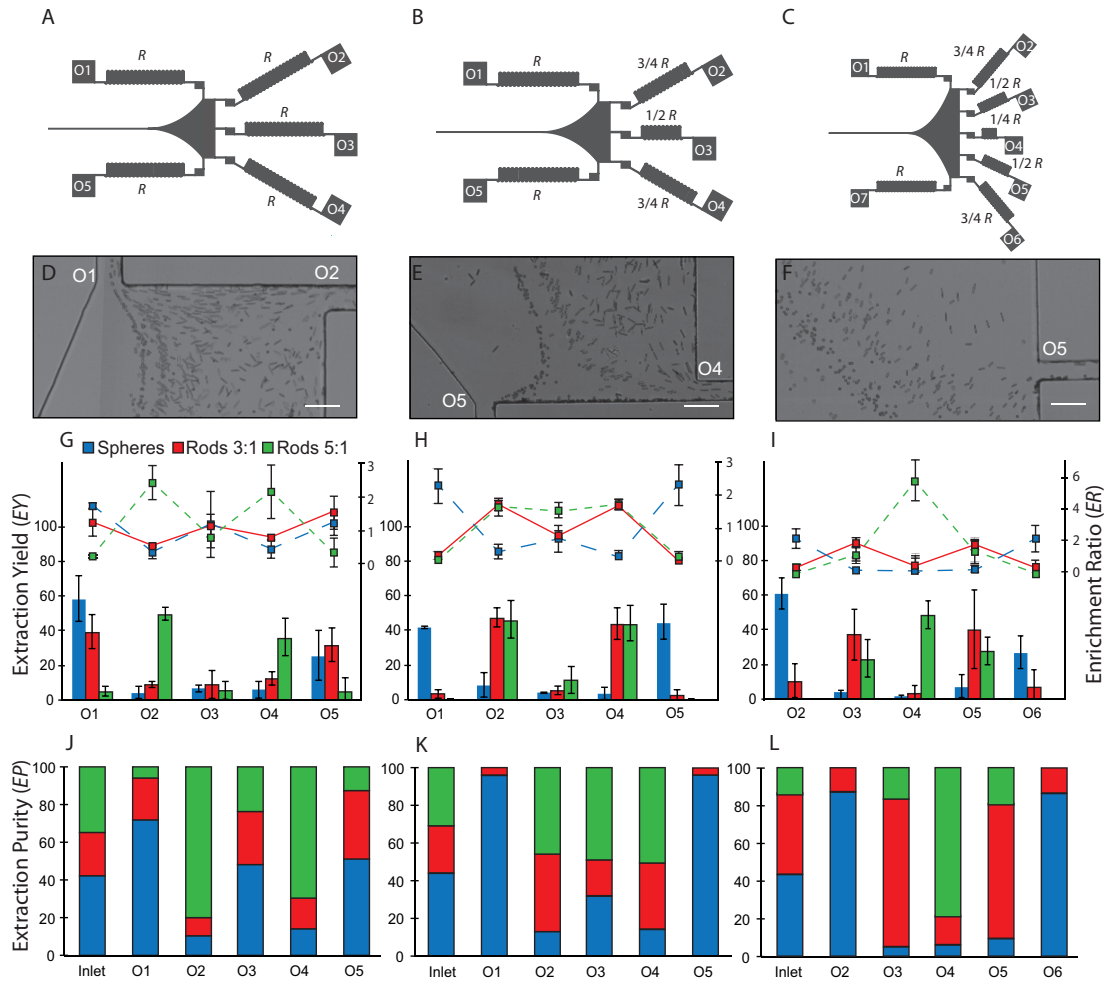


Figure 8. Separation results for 6 μm spherical and ellipsoid particles. The collected ratio of particles is shown at each outlet, considering the Extraction Yield EY, the Enrichment Ratio ER (G, H, I), and the Extraction Purity EP (J, K, L). Each value shows the mean \pm SD from three independent experiments. Three configurations of the SAPS device are considered (A, B, C) and stacked pictures of the separation are shown for each configuration (D, E, F) (Scale bar: 50 μm): (A) $\text{ARc} = 0.53$, $Q = 40 \mu\text{L}/\text{min}$, 5 outlets with equal resistances, (B) $\text{ARc} = 0.64$, $Q = 80 \mu\text{L}/\text{min}$, 5 outlets (O1 to O5) with $\alpha_{1:2} = 3/4$ and $\alpha_{1:3} = 1/2$. (C) $\text{ARc} = 0.64$, $Q = 70 \mu\text{L}/\text{min}$, 7 outlets (O1 to O7) with $\alpha_{1:2} = 3/4$, $\alpha_{1:3} = 1/2$, $\alpha_{1:4} = 1/4$.

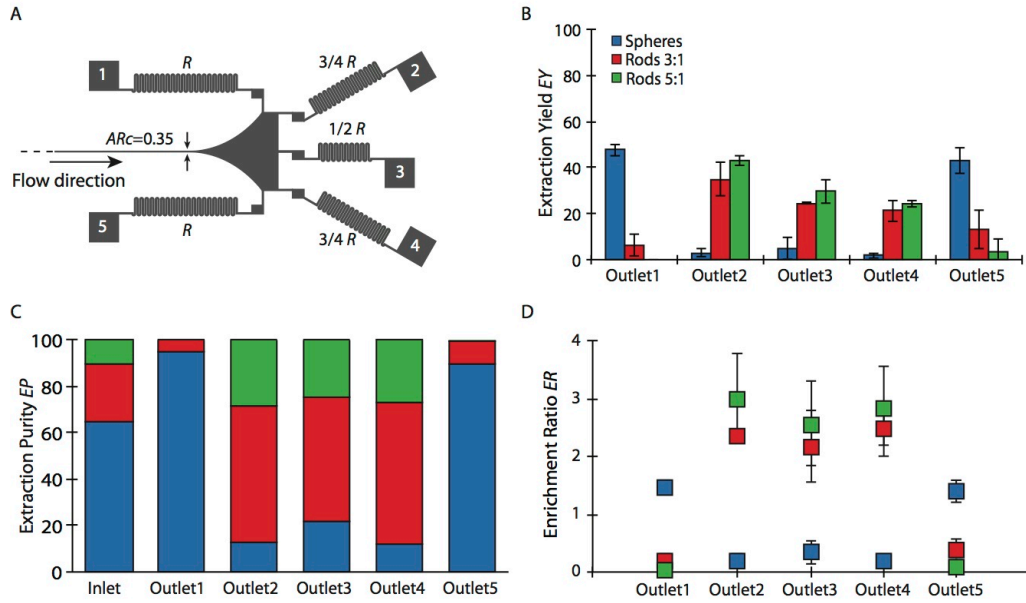


Figure 9. Separation results for 3 μm spherical and rod-shaped particles. (A) Schematic of SAPS device D with $W=25\ \mu\text{m}$, $Q=80\ \mu\text{L}/\text{min}$, 5 outlets with $\alpha_{1:2}=3/4$ and $\alpha_{1:3}=1/2$. The distribution ratio of particles is represented at each outlet, considering the Extraction Yield EY (B), the Extraction Purity EP (C) and the Enrichment Ratio ER (D). Each value shows the mean \pm SD from three independent experiments.

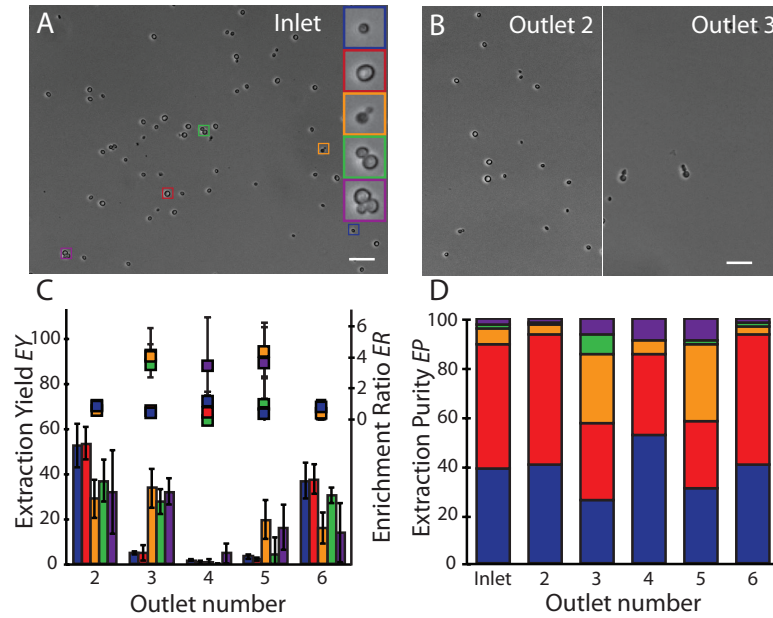


Figure 10. Yeast cell sorting in SAPS device C ($ARc = 0.64$, 7 outlets with $\alpha_{1:2} = 3/4$, $\alpha_{1:3} = 1/2$, $\alpha_{1:4} = 1/4$) at $60 \mu\text{L}/\text{min}$. (A) A picture of the cells in the inlet. Cells are categorized into five groups: small single (blue), large single (red), budded (orange), doublet (green) and aggregate (purple). (B) Singles had a high extraction yield in outlet 2, while (C) in outlet 3 purity of budded cells increased. (C) The collected ratio of particles is shown at each outlet, considering the Extraction Yield EY and Enrichment Ratio ER and (D) Extraction Purity EP. Each value shows the mean \pm SD from three independent experiments.

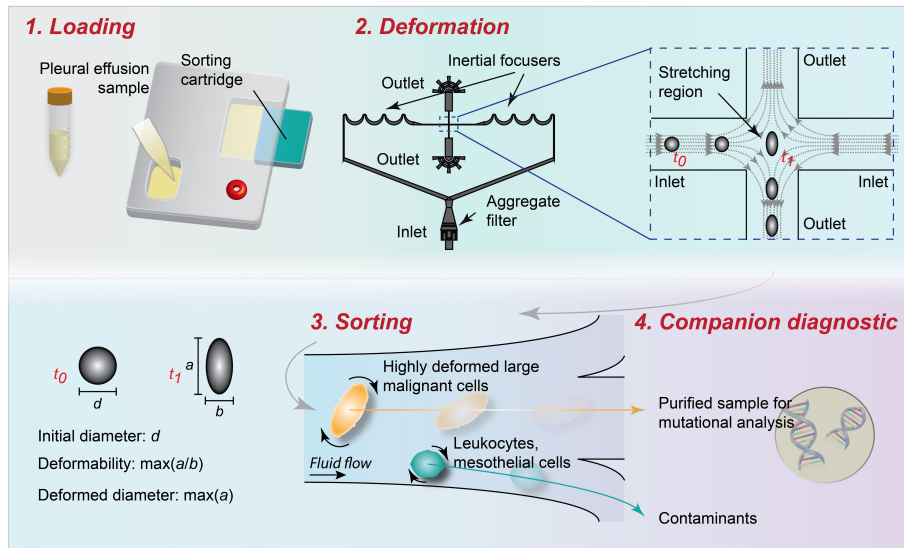


Figure 11. Enriching malignant cells from pleural effusions for companion diagnostics. Step 1 Loading: Sample and cartridge are simply loaded into the instrument. **Step 2 Deformation:** Deformability cytometry (DC) device applies large uniform strains on single cells. **Step 3 Sorting:** Inertial forces focus cells at different equilibrium positions depending on their deformed diameter. **Step 4 Companion diagnostic:** Large, highly deformed malignant cells are enriched into a small volume for analysis.

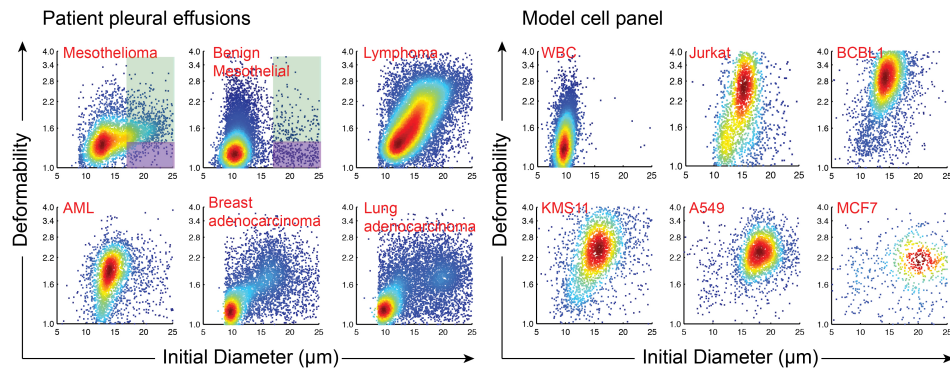


Figure 12. Cell deformability and size are biomarkers for malignant cell populations in pleural fluids. Deformability and size density scatter plots of patient pleural effusion samples (left) and cell line models of cancers that disseminate into the pleural space (right): Jurkat (leukemia), BCBL1 (primary effusion B cell lymphoma), KMS11 (multiple myeloma), A549 (lung adenocarcinoma epithelial cells), MCF7 (breast cancer) and healthy white blood cells. Data collected using deformability cytometry technique. `

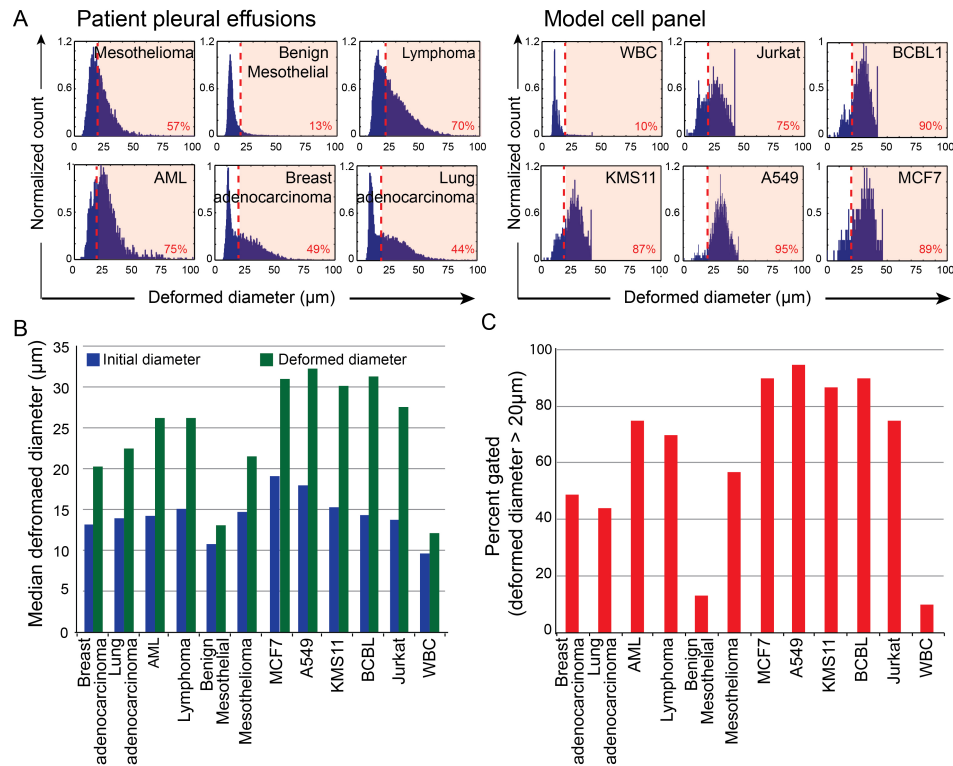


Figure 13. Deformed diameter of stretched cells can be used as a biomarker for enriching malignant cells with high purity. Deformed diameter and size of several model cell lines and patient samples are plotted (A). The histograms of cell deformed diameters show a significant change in malignant cells compared to healthy white blood cells. Red dashed line is gate used in part C, such that less than 10% of WBCs fall within the gate. (B,C) Median values of deformed diameter differ to a larger extent between healthy and malignant cells than initial diameter.

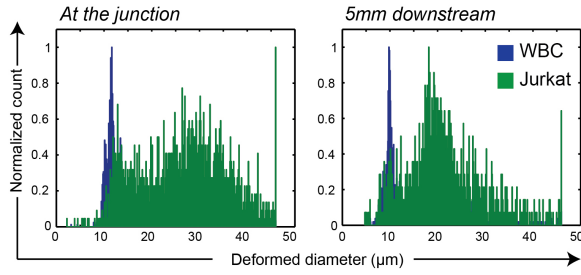


Figure 14. Cells retain their deformation to a large degree while being focused after stretching. Deformed diameter of healthy leukocytes and Jurkats at the stretching region (left) and 5 mm downstream (right).

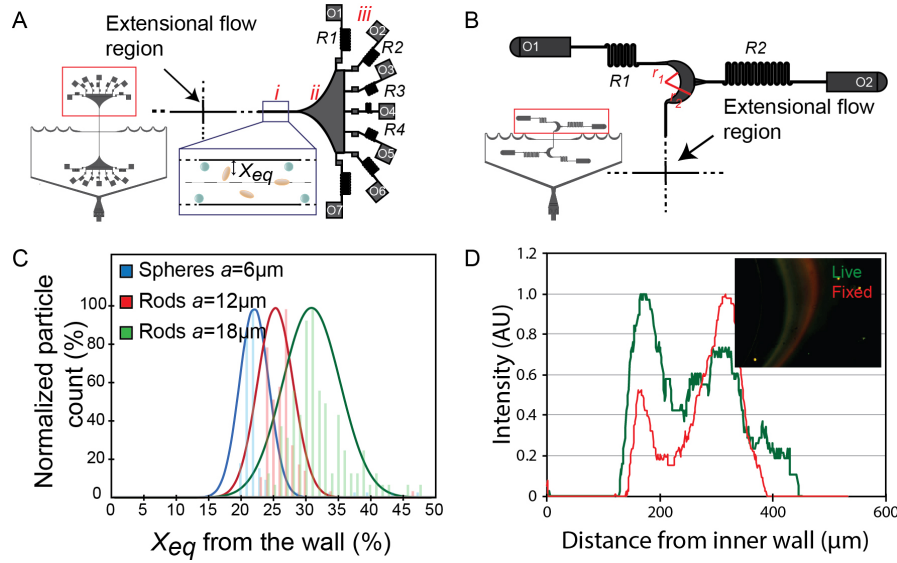


Figure 15. A,B) Fluidic resistance-based microfluidic sorters with 7 outlets on each side of the extensional flow region. The number and resistances of the outlets can be changed to enable the desired sample fractionation. A) Cells can be focused either in a long straight channel or B) in a shorter curved channel after deformation. C) We have previously shown the focusing of 6 μm particles with different aspect ratios at different lateral positions and their successful isolation

with high purity ¹⁸. D) Softer live Jurkat cells were successfully separated from stiffer fixed cells using secondary Dean flow induced in a curved channel.

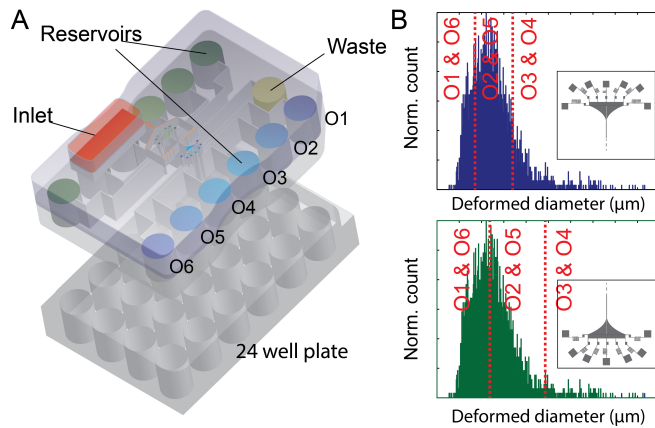


Figure 16. One possible design for the separation cartridge. A) Schematic, the cartridge is compatible with standard 24 well plates. B) Different arrangement of resistances at the two downstream channels enables different sample fractionations) resulting in 6 different sample fractions and 2 waste fractions.